University of Stavanger

FACULTY OF SCIENCE AND TECHNOLOGY

MASTER'S THESIS

Study programme/specialisation: Petroleum Geosciences Engineering	Spring 2021 Open
Author: Orlando Butar Butar	
Faculty supervisor: Nestor Cardozo, University of Stavanger External supervisor: Lothar Schulte, Schlumberger SIS	
Title of master's thesis: Low- versus high-resolution assessment of reservoir compartmentalization in the Wisting field, Norwegian Barents Sea.	
Credits (ECTS): 30	
Keywords: High-resolution seismic Low-resolution seismic Horizon's uncertainties Stø Fm Allan diagram Shale smear Wisting Field	Number of pages: 96 Stavanger, June 15, 2021

Low- versus high-resolution assessment of reservoir compartmentalization in the Wisting field, Norwegian Barents Sea.

by

Orlando Butar Butar

MSc Thesis

Presented to the Faculty of Science and Technology

The University of Stavanger

The University of Stavanger

June 2021

Acknowledgements

First and foremost, I would like to thank my supervisors Nestor Cardozo and Lothar Schulte for their best guidance and support. Their encouragement and commitment have been instrumental to the success of this thesis.

I would like to thank fellow students and friends for valuable discussion and laughs. I wish you all the best!

Finally, I would like to thank my family for their support and motivation during this Master program.

Low- versus high-resolution assessment of reservoir compartmentalization in the Wisting field, Norwegian Barents Sea.

Orlando Butar Butar

The University of Stavanger, 2021

Supervisors: Nestor Cardozo, Lothar Schulte

Abstract

Wisting is Norway's northernmost oil field under development. With ~500 mmboe in shallow marine to fluvial Upper Triassic to Middle Jurassic reservoirs, which are highly faulted and just 250-300 m below sea bottom, this field is quite unique. Wisting sits between the Maud Basin and the Hoop fault complex and is characterized by an orthorhombic fault system consisting of WNW-ESE, NNE-SSW, NE-SW and N-S trending faults. Polygonal faults affect the Cretaceous shales above the reservoir interval. Since the reservoir units are very shallow and the lithology heavily faulted, evaluating fault sealing and the impact of fluid injection on fault reactivation are crucial for the safe, future development of the field. In this study, the seismic survey covers an area of 16km^2 encompassing the Wisting field. Within this area, we use publicly available (via DISKOS) low- (10 to 70 Hz) and high- (7 to 185 Hz) resolution seismic data, to better understand the impact of seismic resolution on the interpretation, fault juxtaposition relationship, reservoir compartmentalization, and gross reservoir volume. The focus of this study is the Stø Fm which provides the main reservoir.

We integrate the information from one exploration well with gamma-ray, resistivity, sonic, density and neutron logs, as well as formation tops. Well interpretation and seismic-well tie are the two initial steps to identify the reservoir zone and link the well log signature to the seismic. The variance and RMS amplitude attributes are used to guide the fault interpretation and to identify hydrocarbon accumulation. Depth structure maps from the low- and high-resolution datasets are constructed, and their differences evaluated. Low- and high-resolution fault throw maps and juxtaposition (Allan) diagrams are also constructed, compared and analysed.

The high-resolution data image the fault zones with impressive detail (although there are fault shadow issues in the footwalls). The study clearly demonstrates that the high-resolution seismic provides essential information such as flat-spot, reservoir heterogeneity and shale smear that cannot be derived from the low resolution seismic. Moreover, the high-resolution model provides more details in the fault throw distribution and in the juxtaposition relationships of the Stø Fm. The top and bottom of this reservoir zone from the high-resolution seismic honours the well-tops and seismic reflectors, whereas this is not the case in the low-resolution seismic. As a result, the reservoir thickness map and the gross reservoir volume from the low-resolution model are more susceptible to uncertainty. The result of this study shows the critical gain in information of high resolution seismic and its impact on the accuracy of the reservoir determination.

Table of Contents

1. INTRODUCTION 1

1.1. STUDY OBJECTIVES 1

1.2. STUDY AREA 2

2. GEOLOGICAL FRAMEWORK 4

2.1. REGIONAL SETTING 4

2.2. HOOP FAULT COMPLEX 9

2.3. LOCAL STRATIGRAPHY 11

3. THEORY 14

3.1. SEISMIC DATA 14

3.1.1. SEISMIC RESOLUTION 15

3.1.2. SEISMIC POLARITY 16

3.2. SEISMIC WELL-TIE 17

3.3. VELOCITY MODELLING 18

3.4. SEISMIC ATTRIBUTES 19

3.4.1. VARIANCE 19

3.4.2. RMS AMPLITUDE 19

3.5. VOLUME OF SHALE 19

3.6. VARIOGRAM 20

3.7. KRIGING 22

3.8. INDICATOR KRIGING 23

3.9. FAULT SEAL MECHANISM 23

3.9.1. ALLAN DIAGRAM 24

3.9.2. SHALE SMEAR 25

3.9.3. SHALE GOUGE RATIO (SGR) 26

4. DATA 27

5. METHODOLOGY 29

5.1. WELL-LOG INTERPRETATION 29

5.2. SEISMIC-WELL TIE 31

5.3. SEISMIC INTERPRETATION 34

5.4. HORIZONS UNCERTAINTIES 36

5.5. DEPTH CONVERSION 36

5.5.1. VELOCITY MODELLING 36

5.6. GEOMODEL BUILDING 37

5.6.1. STRUCTURAL MODELLING 37

5.6.2. FACIES MODELLING 39

5.6.3.PROPERTY MODELLING 39

5.7. FAULT SEAL ANALYSIS 40

5.7.1. ALLAN DIAGRAM 40

5.7.2. SHALE SMEAR 40

5.7.3. SHALE GOUGE RATIO 40

5.8. GROSS ROCK VOLUME ESTIMATION 40

6. RESULTS 41

6.1. DATA CHARACTERIZATION 41

6.1.1. WELL INTERPRETATION 41

6.1.2. SEISMIC-WELL TIE 43

6.1.3. VARIANCE ATTRIBUTE 44

6.1.4. RMS AMPLITUDE ATTRIBUTE 46

6.1.5. FLAT SPOT 48

6.2. HORIZONS' UNCERTAINTIES AND ISOCHORE MAPS 50

6.2.1. HORIZONS' UNCERTAINTIES 50

6.2.2. ISOCHORE MAP 53
6.3. GEOMODEL BUILDING 54
6.3.1. FAULT NETWORK 54
6.3.2. FAULT CUTOFFS 54
6.3.3. FAULT THROW 56
6.4. FAULT SEAL ANALYSIS 58
6.4.1. ALLAN DIAGRAM (ZONES) 58
6.4.2. ALLAN DIAGRAM (FACIES) 61
6.4.3. SHALE SMEAR 62
6.4.4. SHALE GOUGE RATIO AND THE FLUID CONTACT 65
6.5. GROSS VOLUME 68
7. DISCUSSION 71
8. CONCLUSION 74
9. RECOMMENDATION FOR FUTURE WORK 75
10. REFERENCES 76

List of tables

TABLE 4.1: OVERVIEW OF THE AVAILABLE WELL WITH WELL-LOGS 28
TABLE 5.1: NUMBER OF LAYERS IN THE LOW-RESOLUTION MODEL.....39
TABLE 5.2: NUMBER OF LAYERS IN THE HIGH-RESOLUTION MODEL 39
TABLE 6.1: OVERVIEW OF THE TOTAL BULK VOLUMES IN BOTH RESOLUTION MODELS. 69
TABLE 6.2: OVERVIEW OF THE TOTAL GROSS OIL VOLUMES IN BOTH RESOLUTION MODELS. 69
TABLE 6.3: OVERVIEW OF THE TOTAL GROSS GAS VOLUMES IN BOTH RESOLUTION MODELS. ...69

List of figures

FIGURE 1.1: (A) LOCATION OF THE SOUTHWESTERN BARENTS SEA. (B) LOCATION OF THE STUDY AREA. THE WISTING FIELD IS LOCATED BETWEEN THE HOOP FAULT COMPLEX AND THE MAUD BASIN. (C) ZOOM UP OF THE WISTING FIELD. BLACK RECTANGLE SHOWS THE EXTENSION OF THE 3D SEISMIC, AND THE BLUE SQUARE ILLUSTRATES THE MAIN STUDY AREA. BLACK DOT SHOWS THE WELL 7324/8-3 AND THE RED LINE SHOWS THE LOCATION OF THE SECTION IN FIGURES 2.3 AND 2.4B. OILFIELDS ARE SHOWN IN GREEN AND A GAS FIELD IN RED. 3

FIGURE 2.1: (A) TECTONOSTRATIGRAPHIC CHART OF THE BARENTS SEA. RED DASHED RECTANGLE SHOWS THE MAIN RESERVOIRS IN THE STUDY AREA. THEY CONSIST OF THE STØ AND FRUHOLMEN FMS (B) RIFTING PHASES IN THE BARENTS SEA. COLOURS REFER TO THE RIFTING PHASES. MODIFIED AFTER MEUNIER, (2019), GLØRSTAD-CLARK ET AL. (2010), FALEIDE ET AL. (2008) AND GABRIELSEN ET AL. (1990) 8

FIGURE 2.2: (A) VARIANCE ATTRIBUTE FROM THE HIGH-RESOLUTION DATA. THE VARIANCE TIME SLICE IS AT -770MS IN THE STØ FM RESERVOIR LEVEL (B) FOUR MAIN ORIENTATIONS OF THE ORTHORHOMBIC FAULT SYSTEMS. EACH COLOUR REPRESENTS A FAULT ORIENTATION. WNW-ESE FAULTS ARE BLUE, N-S FAULTS ARE GREEN, NE-SW FAULTS ARE YELLOW, AND NNE-SSW FAULTS ARE RED. SEE FIGURE 1.1 FOR LOCATION OF THE SEISMIC DATA. 10

FIGURE 2.3: CROSS SECTION SHOWING THE FAULT BLOCKS AND STRATA DEPOSITED IN THE STUDY AREA. WELL 7324/8-3 WITH GAMMA RAY LOG AND WELL-TOPS IS INCLUDED. YELLOW IN THE LOG INDICATES SANDSTONE, WHILE GREEN SHOWS SHALE. SEE FIGURE 1.1C FOR LOCATION OF THE CROSS-SECTION. 11

FIGURE 2.4: STRATIGRAPHIC COLUMN OF THE STUDY AREA. RED RECTANGLE SHOWS THE MAIN RESERVOIRS (STØ AND FRUHOLMEN FMS) IN THE STUDY AREA. MODIFIED AFTER MEUNIER (2019) AND GLØRSTAD-CLARK ET AL. (2010). (B) CROSS SECTION SHOWING THE WELL 7324/8-3 WITH GAMMA RAY (GR) LOG, AND FORMATION TOPS. SIGNIFICANT THICKNESS CHANGES ARE OBSERVED IN THE KOLMULE FM. FLAT SPOT IS IN THE RESERVOIR LEVEL OF THE STØ FM AND IT TERMINATES AGAINST THE FAULT. 13

FIGURE 3.1: SCHEMATIC ILLUSTRATION OF P-CABLE ACQUISITION. THE MAIN ELEMENT OF THE P-CABLE ACQUISITION IS THAT THE STREAMERS ARE DRAGGED BY AND ARE PERPENDICULAR TO THE CROSS-CABLE. SMALL BIN SIZES RESULT FROM THE SMALL STREAMERS' SPACING (6-15M). (JAKOBSSON ET AL., 2016) 14

FIGURE 3.2: RELATIONSHIP BETWEEN FREQUENCY (F), VELOCITY (V) AND WAVELENGTH (λ) WITH DEPTH. FREQUENCY DECREASES WITH DEPTH. VELOCITY AND WAVELENGTH INCREASE WITH DEPTH. INCREASING WAVELENGTH RESULTS IN LOWER RESOLUTION. LATERAL RESOLUTION = ($\lambda/4$). MODIFIED AFTER BROWN, (1999). 15

FIGURE 3.3: AN EXAMPLE OF AMERICAN POLARITY. THE SEISMIC TRACE SHOWS A TROUGH BETWEEN LAYER 1 (LIMESTONE) AND LAYER 2 (SANDSTONE), WHICH IS DUE TO A DECREASING IMPEDANCE FROM LIMESTONE TO SANDSTONE. A PEAK OCCURS AT THE BOUNDARY OF LAYER 2 (SANDSTONE) AND LAYER 3 (SHALE). THIS IS DUE TO AN INCREASING IMPEDANCE FROM SANDSTONE TO SHALE. TOMASGAARD, (2018). 16

FIGURE 3.4: THE SYNTHETIC SEISMOGRAM RESULTS FROM CONVOLVING THE REFLECTIVITY SERIES WITH A WAVELET. IN ORDER TO HAVE A GOOD WELL TIE, THE PEAK OR TROUGH FROM THE SYNTHETIC SEISMOGRAM SHOULD MATCH THE CORRESPONDING PEAK OR A TROUGH IN THE SEISMIC TRACE. CZAJKOWSKI, (2015).....18

FIGURE 3.5: A SEMI-VARIOGRAM DISPLAYING DATA POINTS, THE RANGE, THE SILL, AND THE NUGGET. RED LINE REPRESENTS THE VARIOGRAM MODEL. THE POINTS REPRESENT THE MEAN VARIANCE OF ALL DATA PAIRS OF A SPECIFIC LAG. GENERALLY, THE CLOSER TWO DATA POINTS ARE TO EACH OTHER, THE SMALLER THE SEMI-VARIANCE VALUE. SCHLUMBERGER, (2017).....21

FIGURE 3.6: THE MOST COMMON VARIOGRAM MODELS. THE SPHERICAL HAS A LINEAR BEHAVIOUR AT SHORTER DISTANCE. THE EXPONENTIAL HAS A STEEP BEHAVIOUR AT SHORTER DISTANCE. THE GAUSSIAN SHOWS A HIGH DEGREE OF CONTINUITY AT SHORT DISTANCES AND TRANSITIONS TO A MORE EXPONENTIAL BEHAVIOUR AT LONGER DISTANCES. SCHLUMBERGER, (2017).....21

FIGURE 3.7: ILLUSTRATION OF THE KRIGING ALGORITHM. X_0 IS THE UNKNOWN VALUE THAT WILL BE ESTIMATED USING A COMBINATION OF WELL DATA (X_I) AND THE VARIOGRAM MODEL. SCHLUMBERGER (2017).....22

FIGURE 3.8: (A) BLUE HORIZON IS CUT BY YELLOW FAULT. THE SMALLEST THROW IS AT THE FAULT TIP WHEREAS THE LARGEST THROW IS AT THE CENTER OF THE FAULT. HORIZONS FROM FOOTWALL AND HANGING WALL ARE MARKED BY THE CUTOFFS. (B) CORRESPONDING ALLAN DIAGRAM. SEVERAL HANGING WALL AND FOOTWALL ZONES ARE PROJECTED ONTO THE FAULT. ALL COLORED ZONES ARE RESERVOIR UNITS. FOOTWALL BEDS ARE INDICATED BY THE BROWN COLOUR WHEREAS HANGING-WALL BEDS ARE IN GREEN. THE SHALE LAYERS ARE WHITE. SPILL POINTS ARE MARKED AT THE INTERSECTION OF HANGING-WALL AND FOOTWALL RESERVOIRS. HYDROCARBON WILL MOVE THROUGH THE SPILL POINTS IF THE

maximum hydrocarbon column height is reached. Ketterman et al. (2019), modified after Allan (1989). 24
Figure 3.9: Example of Shale smear. Black layers represent the shale beds. Shale smear coming from multiple source beds into a normal fault, resulting in a more continuous shale smear. Yielding et al. (1997), modified after Weber et al., (1978)..... 25
Figure 3.10: (a) A schematic diagram showing the calculation of SGR for explicit shale beds. Δz is the thickness of each shale bed. (b) Calculation for a sequence of reservoir zones. Δz is the thickness of reservoir zones and shale. Vsh is the shale volume fraction in the zone. Yielding et al. (1997). 26
Figure 4.1: Structure map showing the top Stø Fm, the location of well 7324/8-3, and the extension of the 3D seismic surveys. Red lines are seismic Xlines and inlines. 27
Figure 4.2: Power spectrum of both datasets. High-resolution seismic (blue), low-resolution seismic (purple). 28
Figure 5.1: Well 7324/8-3 with gamma-ray, resistivity, neutron, density, sonic, and acoustic impedance logs. Main reservoirs tops are marked with numbers 7 (top Stø) and 8 (top Fruholmen). Note that in the Stø reservoir level, resistivity logs show high value, indicating the hydrocarbon accumulation. Cross-over in the neutron-density logs marked by yellow colour indicates the sand zone. The acoustic impedance value where the density log is missing was calculated using Gardner's equation. 30
Figure 5.2: ISIS wavelet for the (a) low-resolution, and (b) high-resolution seismic. Note that the wavelet of the low-resolution seismic is characterized by large side lobes, while in the high-resolution seismic, the side lobes are smaller. The spread of the main lobe together with the size of the side lobes define the seismic resolution. 32
Figure 5.3: Comparison of seismic-well tie between P-cable data (high-resolution) and conventional data (low-resolution). Synthetic traces (peaks and trough) are found richer in the P-cable data. P-cable data gives more information of reservoir heterogeneity in the Stø Fm (between horizon 4 and 5) than in conventional data. Figure left to right (high-resolution seismic, high-resolution synthetic, density log, acoustic impedance log, low-resolution

synthetic, low-resolution seismic). Each wavelet below the seismic sections represents the seismic resolution. 33
Figure 5.4: Structure map of the top Stø and well 7324/8-3. Black square (A) shows the study area and grey rectangle (B) shows the area for fault analysis. Line (C) is the section shown in figure 5.5. Note that the well 7324/8-3 is located at a northernly tilted fault block. 35
Figure 5.5: (left) low-resolution, and (right) and high-resolution seismic section. The navigation is shown in figure 5.4. Both sections show well 7324/8-3 with gamma-ray log and well-tops. Yellow in the gamma-ray is sandstone while green is shale. Notice that the flat spot is only displayed in the high-resolution seismic. This fluid contact is located in the Stø Fm updip of the well and terminates against the fault 36
Figure 5.6: (a) Fault modelling processes. (b) Model construction. (c) Structural gridding. Number of layers and grid sizes are inserted in the structural gridding process. 38
Figure 5.7: The vertical variogram for facies modelling. The blue line represents the variogram model whereas the points are the averaged semivariance of the data pairs. The red point indicated the variogram range. 39
Figure 5.8: The vertical variogram for property modelling. The blue line represents the variogram model whereas the points are the averaged semivariance of the data pairs. The red point indicated the variogram range. 40
Figure 6.1: Well 7324/8-3 with gamma-ray, resistivity, neutron, density, sonic and acoustic impedance logs, and the stacking pattern. The main reservoir is in the Stø Fm between tops 7 and 8. Note that in this interval, the resistivity logs show high value, indicating a hydrocarbon accumulation. Cross-over of the neutron-density logs marked by the stippled yellow colour indicates the sand zone. Two coarsening upward and one fining upward interval are observed. The fining upward interval corresponds to the shale rich Fuglen and Hekkingen Fms. See well location in Figure 5.4 42
Figure 6.2: Variance attribute from the (a) low-resolution, and (b) high-resolution data. Both time slices are at -770ms (Stø Fm reservoir level). Note that the faults are sharper in the high-resolution seismic and are indicated by higher variance. 45

FIGURE 6.3: (A) UNINTERPRETED AND (B) INTERPRETED LOW-RESOLUTION SEISMIC LINE. NOTE THAT ALL HORIZONS ARE FOLDED IN THE EASTERN PART OF THE AREA. (C) UNINTERPRETED AND (D) INTERPRETED HIGH-RESOLUTION SEISMIC LINE. TOP KOLJE AND TOP FUGLEN ARE FOLDED IN THE EASTERN PART, WHILE TOP STØ AND TOP FRUHOLMEN ARE FAULTED. SEE NAVIGATION LINE IN FIGURE 6.2.....46

FIGURE 6.4: RMS AMPLITUDE EXTRACTED ON THE TOP STØ IN THE (A) LOW-RESOLUTION SEISMIC, AND (B) HIGH-RESOLUTION SEISMIC. FROM BOTH FIGURES, THE HIGH RMS AMPLITUDE VALUES ARE IN THE VICINITY OF THE WNW-ESE FAULT. HOWEVER, IN THE HIGH-RESOLUTION SEISMIC, THE HIGH RMS AMPLITUDES COVER A LARGER AREA.....47

FIGURE 6.5: (A) LOW-RESOLUTION, AND (B) HIGH-RESOLUTION SEISMIC SECTION. BOTH SECTIONS SHOW WELL 7324/8-3 WITH GAMMA RAY LOG AND WELL-TOPS. YELLOW IN THE GAMMA-RAY IS SANDSTONE WHILE THE GREEN IS SHALE. THE FLAT SPOT IS DISPLAYED ONLY IN THE HIGH-RESOLUTION SEISMIC. IT IS IN THE STØ FM, UPDIP OF THE FAULT AND TERMINATES AGAINST THE FAULT. SEE NAVIGATION LINE IN FIGURE 6.4. 49

FIGURE 6.6: HORIZONS' UNCERTAINTIES. RED LINES CORRESPOND TO THE LOW-RESOLUTION SURFACES WHILE BLACK LINES ARE THE HIGH-RESOLUTION SURFACES. BOTH SURFACES ARE DISPLAYED ON THE HIGH-RESOLUTION SEISMIC. LOW-RESOLUTION TOP STØ AND TOP FRUHOLMEN DO NOT HONOUR THEIR WELL-TOPS AND THE SEISMIC REFLECTORS. SURFACES FROM THE LOW-RESOLUTION SEISMIC BECOME MORE IRREGULAR WITH DEPTH. THE NAVIGATION LINE IS GIVEN IN LINE C OF FIGURE 5.4. 51

FIGURE 6.7: DIFFERENCES BETWEEN HORIZONS INTERPRETED IN THE LOW- AND HIGH-RESOLUTION SEISMIC. NOTE THAT THE STANDARD DEVIATION INCREASES WITH THE HORIZON DEPTH. 52

FIGURE 6.8: STØ FM ISOCHORE MAP BASED ON THE (A) HIGH-RESOLUTION (HR) AND (B) LOW-RESOLUTION (LR) DATA. THE STØ FM VERTICAL THICKNESS IS MORE CONSISTENT IN THE HIGH-RESOLUTION VARIATION. BLACK LINES INDICATE THE FAULT ZONES. THE ISOCHORE MAPS COVER THE AREA A IN FIGURE 5.4. 53

FIGURE 6.9: FAULT NETWORK FROM (A) LOW-RESOLUTION AND (B) HIGH-RESOLUTION MODEL. THE CONTINUOUS LINES ARE THE FOOTWALL CUTOFFS WHILE THE DASHED LINES ARE THE HANGING WALL CUTOFFS. NOTE THAT THE PINK-RED FAULT IS NOT PRESENT IN THE LOW-RESOLUTION MODEL. THE MODEL COVERS AREA A OF FIGURE 5.4. 54

FIGURE 6.10: WNW-ESE FAULT PLANE WITH CUTOFFS FROM (A) THE LOW-RESOLUTION AND (B) THE HIGH-RESOLUTION MODEL. CUTOFFS IN THE LOW-RESOLUTION MODEL ARE MORE IRREGULAR WITH DEPTH. SEE AREA B IN FIGURE 5.4 FOR THE LOCATION OF THE FAULTS. 55

FIGURE 6.11: Fault throw from (a) low-resolution and (b) high-resolution model. Throw profiles from (c) low-resolution and (d) high-resolution model. Fault throw from high-resolution model is more consistent. See area B in Figure 5.4 for the location of the profile……57

FIGURE 6.12: ALLAN DIAGRAM FROM THE (A) LOW-RESOLUTION AND (B) HIGH-RESOLUTION MODEL. THE JUXTAPOSITION OF STØ FM AGAINST OTHER FORMATIONS ARE MARKED WITH DIFFERENT SYMBOLS. NOTE THAT IN THE HIGH-RESOLUTION MODEL, THE STØ FM IS JUXTAPOSED AGAINST ITSELF TO THE EAST, AGAINST THE FUGLEN FM IN THE CENTRAL PART OF THE FAULT, AND FULLY JUXTAPOSED AGAINST THE KOLJE FM TO THE WEST. IN THE HIGH-RESOLUTION MODEL, THE JUXTAPOSITION OF THE STØ AND FRUHOLMEN FMS CAN BE DIVIDED INTO THREE SEPARATE ZONES. THE ALLAN DIAGRAM FROM THE LOW-RESOLUTION MODEL CANNOT RESOLVE THESE DETAILS. SEE AREA B IN FIGURE 5.4 FOR THE LOCATION OF THE ANALYSIS.....60

FIGURE 6.13: (A) LOW-RESOLUTION AND (B) HIGH-RESOLUTION ALLAN DIAGRAM (FACIES). NOTE THAT IN THE LOW-RESOLUTION DIAGRAM, THE JUXTAPOSITIONS UNDULATE, WHILE IN THE HIGH-RESOLUTION DIAGRAM, THE JUXTAPOSITION ARE MORE CONSISTENT.....61

FIGURE 6.14: (A) LOCATION OF SHALE SMEAR AND (B) 3D DISTRIBUTION. THE VARIANCE TIME SLICE IS AT RESERVOIR LEVEL (-770MS). THE SHALE SMEAR GRADUALLY DEVELOPS FROM THE EAST (0-10M FAULT THROW), REACHING THE MAXIMUM CONTINUITY IN THE CENTRAL AREA (40-50M FAULT THROW) AND STOPS DEVELOPING IN THE WESTERN AREA (60-70M FAULT THROW). 62

FIGURE 6.15: HIGH-RESOLUTION SEISMIC SECTION SHOWING SHALE SMEARS ON (A) THE EASTERN PART OF THE FAULT, (B) THE CENTRAL PART OF THE FAULT, AND (C) THE WESTERN PART OF THE FAULT. SEE LINES A, B, C IN FIGURE 6.14A AS NAVIGATION LINES. SHALE SMEARS FROM THE TWO SOURCE BEDS DO NOT MIX IN THE EASTERN PART, WHILE IN THE CENTRAL PART THEY MIX. SHALE SMEAR IS NOT PRESENT IN SECTION C WHERE THE FAULT THROW REACHES ITS MAXIMUM VALUE.....64

FIGURE 6.16: (A) LOW-RESOLUTION SEISMIC LINE AND WELL 7324/8-3 WITH GAMMA-RAY LOG (B) SAME SECTION SHOWING HIGH-RESOLUTION SEISMIC AND WELL 7324/8-3 WITH GAMMA-RAY LOG. IN BOTH SECTIONS, THE SHALE GOUGE RATIO (SGR) ON THE FAULT IS DISPLAYED. YELLOW IN THE GAMMA RAY LOG IS SANDSTONE WHILE GREEN IS SHALE. THE HIGHEST SGR VALUE (60%) IS AT THE JUXTAPOSITION OF SHALE AGAINST SHALE, AND THE LOWEST SGR VALUE (5-15%) IS AT THE SAND-SAND JUXTAPOSITION (FIGURE 6.15B). AT THE STØ

reservoir level, the SGR value is around 25-50% indicating probable fault sealing. Line B in Figure 6.14a shows the section navigation. 66
Figure 6.17: (a) High-resolution seismic line and well 7324/8-3 with gamma-ray log. (b) Same line and log with fault with SGR values and the fluid contact. The Stø Fm at the well is filled with oil. The lowest known oil is down to 722.2m in the Fruholmen Fm (NPD). The flat spot terminates at the fault and updip of the well. Hence, the flat spot should correspond to the gas-oil contact. Line B in Figure 6.14a shows the section navigation. 67
Figure 6.18: (a) Structure map of the top Stø, well 7324/8-3 and cross sections b and c. (b) Cross section b showing the hydrocarbon accumulation at the well. In both model resolutions, the gas and oil contact is observed in the north-eastern block. The depth of the gas-oil contact was set based on the flat spot depth from the high-resolution seismic. (c) Cross-section c showing the hydrocarbon accumulation west of the well. Gas is present in the south-western block of the low-resolution model, but not in the high-resolution model. 70

1. Introduction

Geophysical exploration methods play a significant role in the oil and gas industry. One of these methods is seismic surveying. It is undoubtedly one of the most important geophysical techniques due to its ability to detect subsurface features (Mondol, 2010). High-resolution (P-Cable) seismic was patented in 2003 and was commercialized in 2008. Recently, it is used for the shallow hydrocarbon exploration, geohazard investigation, time-lapse seismic studies, as well as near-surface stratigraphy analysis (Smith and Mattox, 2020). In comparison to the low-resolution (conventional) seismic, the P-Cable seismic uses smaller streamer spacing which results in dense common midpoints with smaller bin sizes and increased seismic resolution. Furthermore, the P-Cable systems are built up of 12 to 24 very short streamers, allowing a cost-effective acquisition of seismic profiles (Planke et al., 2009).

With the recent energy demand and need for carbon sequestration projects, it is essential to explore the subsurface in greater detail. Reservoirs are getting more challenging in terms of tectonics, compartmentalization, and facies distributions. Therefore, seismic resolution is crucial for defining thin lithological layers and small faults. This information is important for describing the reservoir heterogeneity, compartmentalization, and seal integrity. Due to these challenges, high-resolution seismic becomes a necessity. Vertical and horizontal resolution are improved due to higher frequencies and shorter wavelengths (Mondol, 2010). The focus of this study is to contrast the gain in information when using high- versus low-resolution seismic from a shallow, heavily compartmentalized reservoir in the Norwegian Barents Sea.

1.1. Study objectives

Aim of the Study

The aim of the study is to compare the seismic signal from low- and high-resolution seismic, as well as quantify the impact of high-resolution seismic on the accuracy of the structural reservoir model.

Objectives

The objectives of the study are to evaluate:

1. The value of a low and a high-resolution seismic dataset from the same area, in terms of:
    a. Seismic attributes for fault detection and seismic anomalies identification
    b. Differences of the structure imaging

c. Uncertainties in seismic interpretation

2. The impact of the interpretation uncertainty on structural modelling and the estimated reservoir volume

3. The impact of the dataset resolution on fault juxtaposition relationships:
    a. How do the horizons' fault displacements change along strike?
    b. Do the structural models from the two datasets show different Allan diagrams and shale gouge ratio (SGR)?
    c. Can high-resolution seismic capture the distribution of shale smears?

1.2. Study area

The study area is the Wisting field, which is an oil field currently in the design phase (Stueland, 2016). Wisting is located in the Barents Sea, 300 kilometres west from the northern coast of Norway (**Figure 1.1**). The Wisting field was discovered in 2013 during the drilling of the 7324/8-1 exploration well. It is the first discovery to be made in the Hoop fault complex and Maud Basin. The field has an expected ~500mmboe but is quite challenging to develop because the reservoir is located at just 250-300m below the seabed (Boschi, 2017; Paulsen et al., 2019; Stueland, 2016). The reservoir is heavily faulted and contains oil in sandstones of the Stø and Fruholmen Fms. In addition, gas is found in sandstones of the Stø Fm. This thesis will focus mainly on the most prolific reservoir interval, which is in the Stø Fm.

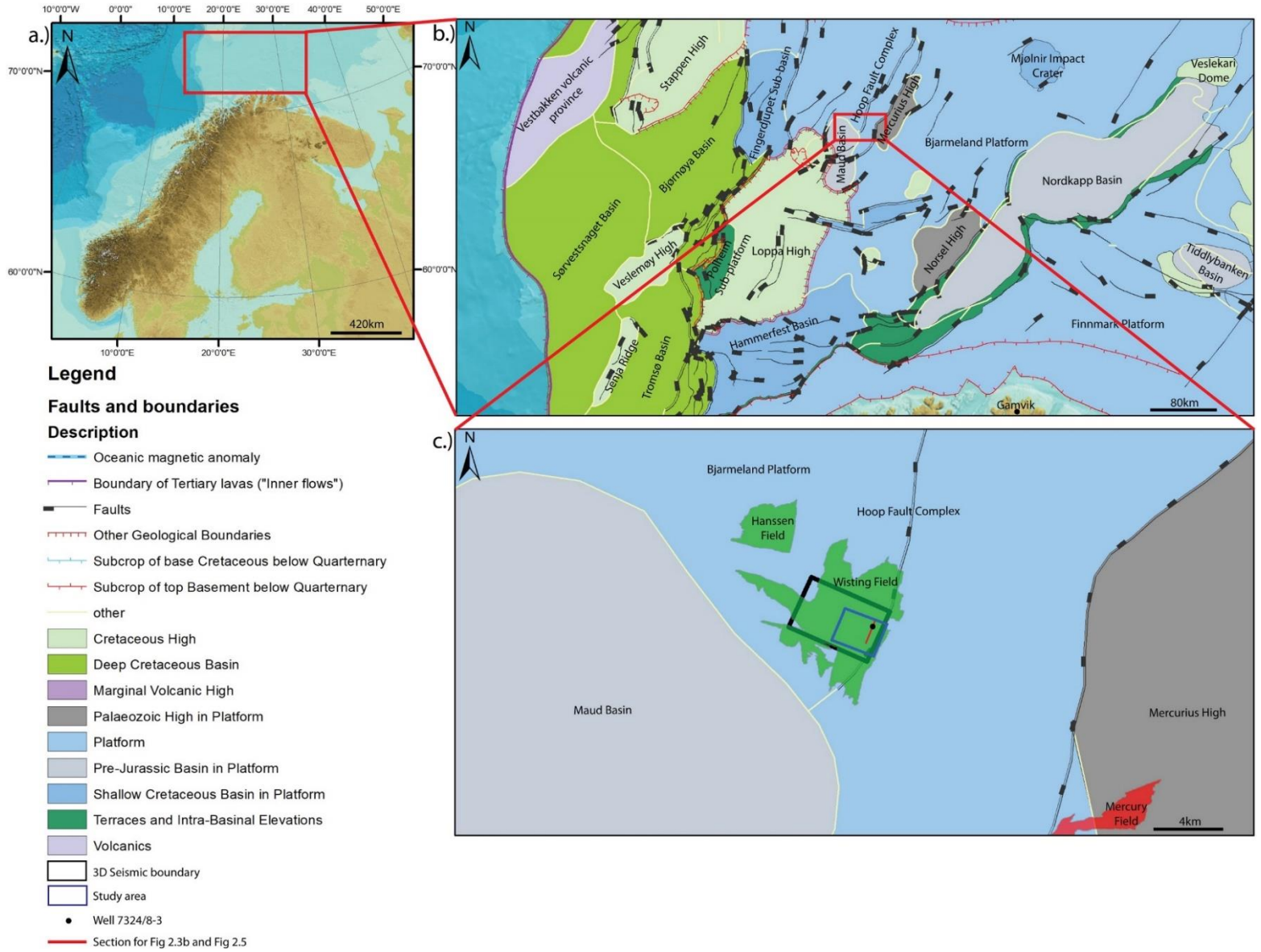

Figure 1.1: (a) Location of the southwestern Barents Sea. (b) Location of the study area. The Wisting field is located between the Hoop fault complex and the Maud Basin. (c) Zoom up of the Wisting field. Black rectangle shows the extension of the 3D seismic, and the blue square illustrates the main study area. Black dot shows the well 7324/8-3 and the red line shows the location of the section in Figures 2.3 and 2.4b. Oilfields are shown in green and a gas field in red.

2. Geological framework

2.1. Regional setting

At present day, the Barents Sea is subdivided into several platforms, highs, and basins (**Figure 1.1b**). In the north, the Barents Sea is bounded by the Svalbard archipelago and Franz Josef Land. The eastern boundary is Novaya Zemlya, which extends south to the Kola Peninsula and the Norwegian coast (Faleide et al., 1984). The main structural elements have dominant ENE-WSW to NE-SW and NNE-SSW to NNW-SSE trends (Gabrielsen et al., 1990) **(Figure 2.1b)**. The Barents Sea has experienced several rifting processes (Dengo and Røssland. 1992). Rifting occurred at four different times: Carboniferous, Permian, Late Jurassic-Early Cretaceous, and Late Cretaceous-Paleocene. These rifting events were important for the creation of major basins and the development of the petroleum system.

Carboniferous rifting

The first major rifting of the Barents shelf occurred during the Carboniferous. Several major basins such as the Tromsø, Bjørnøya, Hammerfest, Maud and Nordkapp basins were formed during this event (Dengo and Røssland. 1992; Faleide et al., 2010). During this period, the Caledonides structures had an impact on the configuration of the Barents platform. They controlled the distribution of basins and highs (Collanega et al., 2017; Gudlaugsson et al., 1998). As a result, the sedimentation pattern in the Barents Sea was also affected. Carbonate build-ups were formed at the basin margins and intra-basinal highs during the Carboniferous rifting (Collanega et al., 2017; Gudlaugsson et al., 1998) **(Figure 2.1)**. Towards the end of the Carboniferous rifting, the fault movement stopped, and the structural relief was gradually filled by Upper Carboniferous-Permian sediments.

Permian rifting

The previous rift structures from the Carboniferous had an impact on the sedimentation in the Late Permian (Collanega et al., 2017; Gudlaugsson et al., 1998). Clastic deposition began primarily at the end of the Carboniferous rifting. This event marked the initial development of a sag basin until the Late Permian. The Upper Permian succession was marked by the deposition of cherty limestones and shales (Faleide et al., 2010) **(Figure 2.1)**. During this period, the rifting mainly took place in the western Barents Sea. In the Late Permian-Early Triassic, the western Barents Sea was affected by renewed faulting, uplift, and erosion. This

rifting phase was characterized by a N-S structural trend along the entire western margin (Faleide et al., 2010).

Late Jurassic-Early Cretaceous rifting

Large volumes of sediments were deposited during the Triassic. Sediment deposition was affected by the erosion of the Uralian Mountains located to the east and south-east of the Barents Sea. The regional subsidence of the Barents Sea was marked by an alluvial-deltaic system prograding to the west and northwest, with thicknesses reaching 2000m. These successions are characterized by primarily locally organic-rich clay, with silt and sand intervals as secondary deposits (Collanega et al., 2017; Glørstad-Clark et al., 2010) **(Figure 2.1)**. The shoreline moved basinwards in the Late Triassic and resulted in regression and erosion of the Late Triassic deposits (Faleide et al., 2010).

Triassic deposits and structures had an impact on the Early Jurassic paleogeography. In the Early Jurassic, deltaic and alluvial systems were formed. However, in the Middle Jurassic, a regional transgression affected sediment deposition. The coastline shifted landward, allowing larger space for the shoreline environment (Henriksen et al., 2011b). In general, prior to the Late Jurassic rifting, several reservoir successions were deposited in the western Barents Sea. These reservoirs belong to the Kapp Toscana Group. During the deposition of these reservoirs, the area was relatively quiet (Glørstad-Clark et al., 2010; Henriksen et al., 2011b).

Regional extension and strike-slip faulting was produced by the Late Jurassic-Early Cretaceous rifting. The structures formed during this event affected the development of the Bjørnøya, Tromsø, and Harstad basins (Faleide et al., 2010).

Late Cretaceous-Paleocene rifting

The Late Jurassic-Early Cretaceous rifting had an impact on the western Barents Sea. During the Early-Middle Cretaceous, the western Barents Sea subsided progressively (Fitriyanto, 2011). Shales and limestones were the main sediments filling the SW Barents Sea basins (**Figure 2.1**). These units were mainly deposited in a marine environment dominated by distal conditions (Faleide et al., 2010).

The Late Cretaceous-Paleocene rifting was mainly related to the opening of the Norwegian-Greenland Sea and the northward spreading of the Central Atlantic. The main deformation during this event was the reactivation of the Late Paleozoic fault systems. It

resulted in a sheared margin on the western Barents Sea (Collanega et al., 2017; Glørstad-Clark et al., 2010).

Uplift and erosion

In the Late Cretaceous, A large portion of Barents Sea has experienced a major episode of uplift and erosion. The first phase of Barents Sea regional uplift is caused by the tectonic compression due to movement of Greenland towards the Barents Sea. It is resulting in the increasing net erosion in the Barents Sea. The second phase of uplift and erosion was in the Pliocene-Quaternary. In this period, uplift is related to the isostatic rebound caused by the intensified glaciation in the northern hemisphere. Ice sheets erosion resulted in the removal of vast amounts of sediments from the Barents shelf. As a result of the isostatic rebound, the crust has become tilted. The South Barents Basin experienced net erosion of about 1500m (Lasabuda e al., 2021). Understanding the history of uplift and erosion of the Barents Sea basins is critical for evaluating prospectivity, such as remigration of hydrocarbon to shallower traps, decreasing sealing capacity due to removal of overburden, reactivation of fault, as well as changes of hydrocarbon phase (oil to gas) (Henriksen et al., 2001a; Lasabuda et al., 2021)

a.)

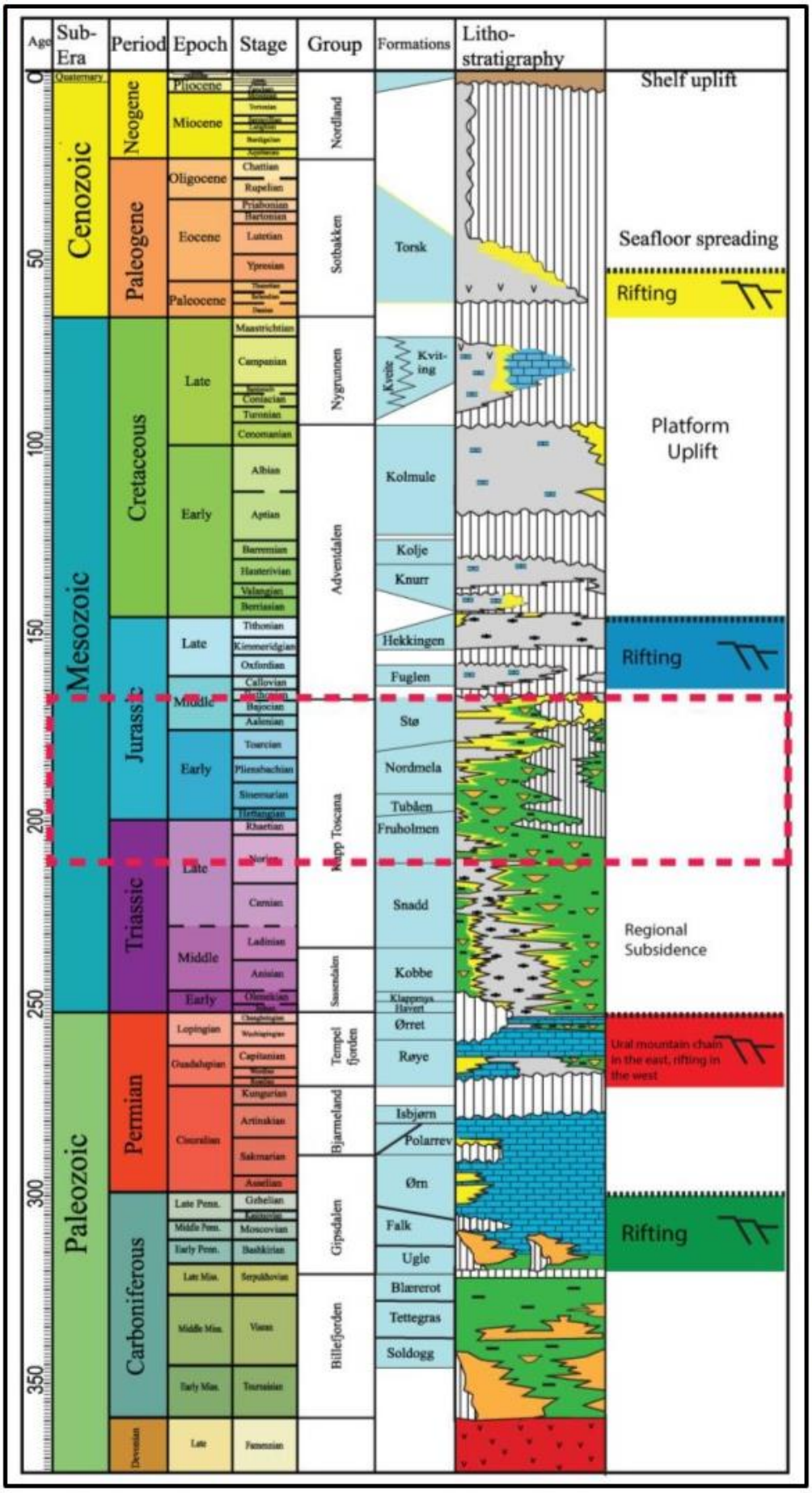
Age
Sub-Era
Period
Epoch
Stage
Group
Formations
Litho-stratigraphy
Cenozoic
Mesozoic
Paleozoic
Quaternary
Neogene
Paleogene
Cretaceous
Jurassic
Triassic
Permian
Carboniferous
Devonian
Pliocene
Miocene
Oligocene
Eocene
Paleocene
Late
Early
Middle
Nordland
Sotbakken
Nygrunnen
Adventdalen
Kapp Toscana
Sassendalen
Tempel fjorden
Bjarmeland
Gipsdalen
Billefjorden
Torsk
Kvitnos
Kviting
Kolmule
Kolje
Knurr
Hekkingen
Fuglen
Stø
Nordmela
Tubåen
Fruholmen
Snadd
Kobbe
Klappmys
Havert
Ørret
Røye
Isbjørn
Polarrev
Ørn
Falk
Ugle
Blærerot
Tettegras
Soldogg
Shelf uplift
Seafloor spreading
Rifting
Platform Uplift
Rifting
Regional Subsidence
Ural mountain chain in the east, rifting in the west
Rifting

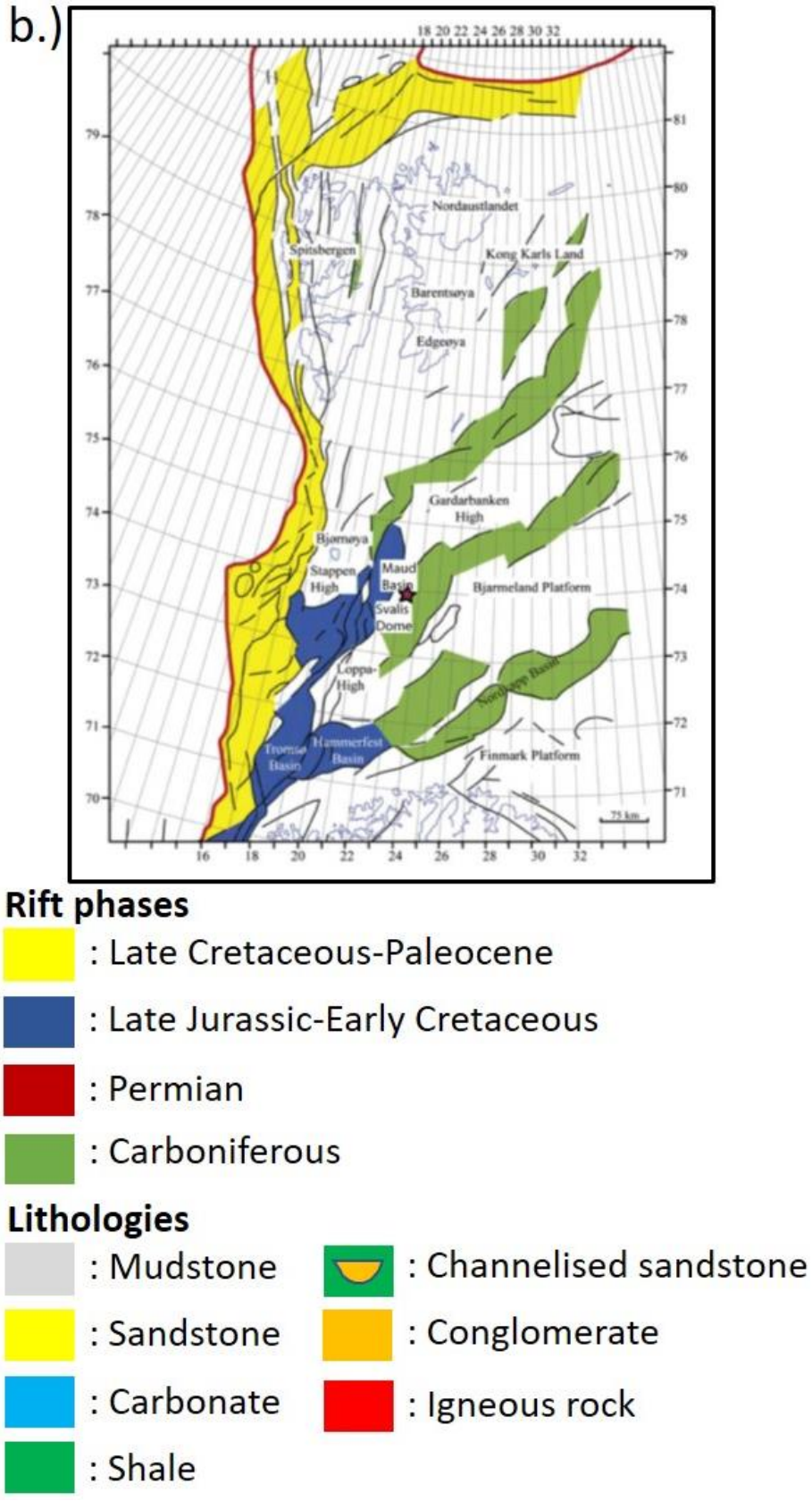

Figure 2.1: (a) Tectonostratigraphic chart of the Barents Sea. Red dashed rectangle shows the main reservoirs in the study area. They consist of the Stø and Fruholmen Fms (b) Rifting phases in the Barents Sea. Colours refer to the rifting phases. Modified after Meunier, (2019), Glørstad-Clark et al. (2010), Faleide et al. (2008) and Gabrielsen et al. (1990).

2.2. Hoop fault complex

The Hoop fault complex is bounded by the Bjarmeland Platform in the north and the Loppa High in the south. The central part of the complex had an impact on the development of the Maud Basin and the Svalis Dome. It is characterised by normal faulting with NE-SW trend. This fault system controlled the sedimentation of the Maud Basin in the Late Carboniferous and Permian. The Hoop Fault complex was reactivated during the Middle Triassic, Late Jurassic-Early Cretaceous, and Tertiary (Gabrielsen et al., 1990). This implies old weakness zones across the Hoop fault complex (Collanega et al., 2017).

The Hoop fault complex is characterized by an orthorhombic fault system. The development of this system started in the late Mesozoic, and it was influenced by the interaction between the Atlantic and Arctic rifting (Collanega et al., 2017). **Figure 2.2a** shows a variance time slice from the high-resolution dataset. The time slice is in the Stø Fm reservoir level (-770ms). It clearly displays the main orientations of the orthorhombic fault system. These are WNW-ESE, NNE-SSW, NE-SW and N-S faults (**Figure 2.2b**).

The northern segment of the Hoop fault complex is represented by a NE-SW half graben (**Figure 2.3**). This graben separates the Bjarmeland Platform from the Fingerdjupet subbasin. The throw of the NE-SW fault decreases south towards the Maud Basin. The WNW-ESE and NNE-SSW faults form a system of small horsts and grabens (Collanega et al., 2017) (**Figure 2.2b, 2.3**).

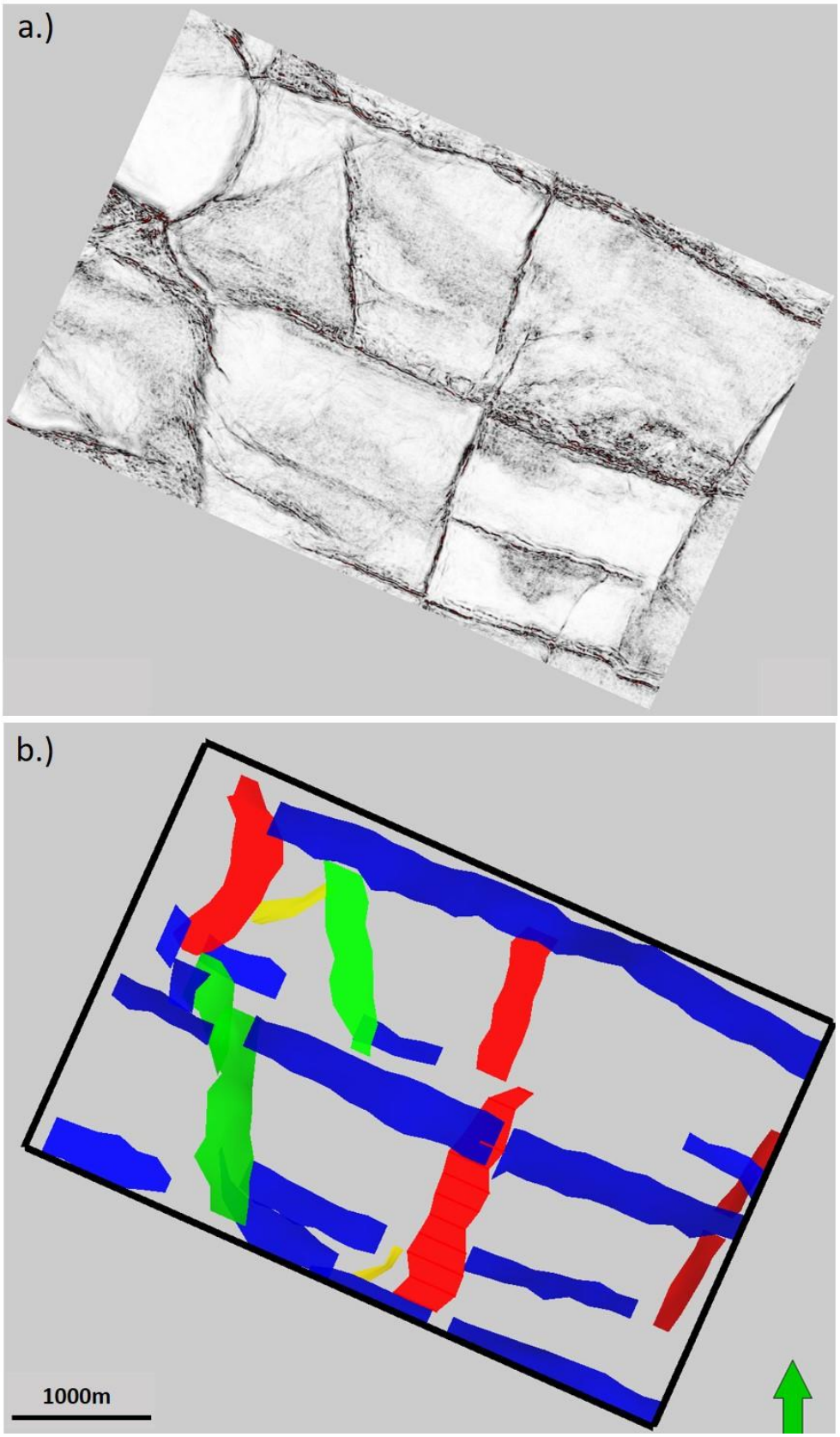

Figure 2.2: (a) Variance attribute from the high-resolution data. The variance time slice is at -770ms in the Stø Fm reservoir level (b) Four main orientations of the orthorhombic fault systems. Each colour represents a fault orientation. WNW-ESE faults are blue, N-S faults are green, NE-SW faults are yellow, and NNE-SSW faults are red. See Figure 1.1 for location of the seismic data.

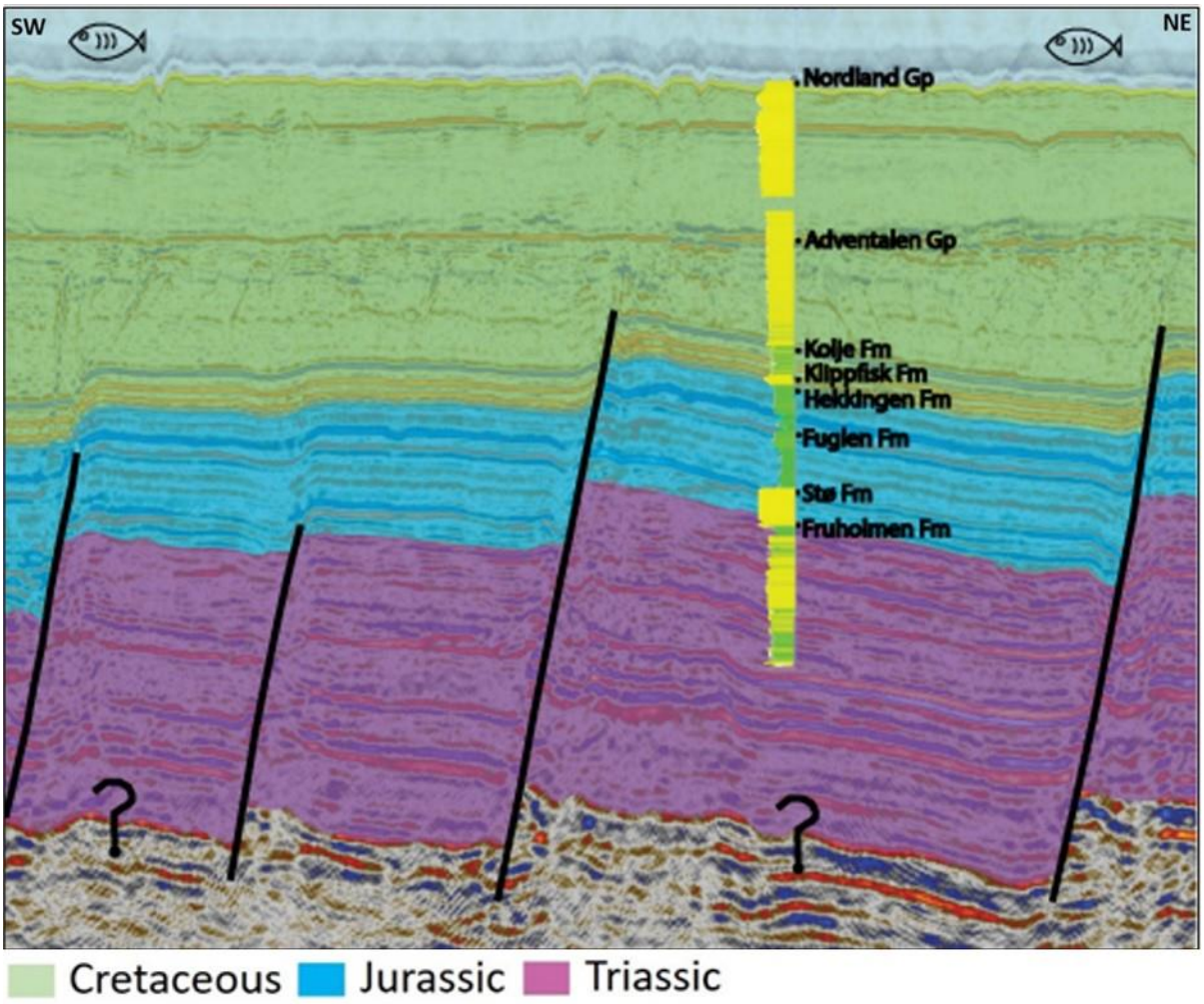

Figure 2.3: Cross section showing the fault blocks and strata deposited in the study area. Well 7324/8-3 with Gamma ray log and well-tops is included. Yellow in the log indicates sandstone, while green shows shale. See Figure 1.1c for location of the cross-section.

2.3. Local stratigraphy

The Lower Cretaceous succession in the study area consists of the Kolmule, Kolje, and Klippfisk Fms. These formations form part of the Adventdalen Group **(Figure 2.4)**. The Kolmule Fm is characterized by shale which was deposited in a marine environment. The Kolje Fm primarily consists of mudstones **(Figure 2.4)** which were deposited in a distal open-marine environment. Unlike the Kolmule and Kolje Fms, the Klippfisk Fm was deposited in platform areas. It is dominated by limestones which gradually change into calcareous claystones deposited on a deeper shelf (Faleide et al., 2019; Smelror et al., 1998). In the study area, the Adventdalen Group is 67m thick and it is bounded by a top regional unconformity **(Figure 2.4)**. This unconformity was caused by the uplift and erosion of the Upper Cretaceous-Paleogene strata (Henriksen et al., 2011a).

The main reservoir intervals in the Wisting field are in the Upper Triassic-Jurassic Kapp Toscana Group. The Jurassic reservoirs are the most prolific, and the shallowest Jurassic

reservoir is just 250m below the seabed. The Jurassic reservoirs consist of the Stø Fm **(Figure 2.4)**. The Stø Fm was deposited in a shoreface environment and represents a transgressive succession. It consists of homogenous sandstones up to 20m thick. The Fruholmen Fm is 112m thick and it is comprised of channelized sandstones and shale. In the Hoop area, the Fruholmen Fm is overlain unconformably by the Stø Fm (Klausen et al., 2019).

Polygonal faults are also found in the Kolmule Fm above the reservoir interval. Due to the presence of faults from the Hoop complex and the polygonal faults, the seal rock integrity might be compromised, and hydrocarbon leakage may occur.

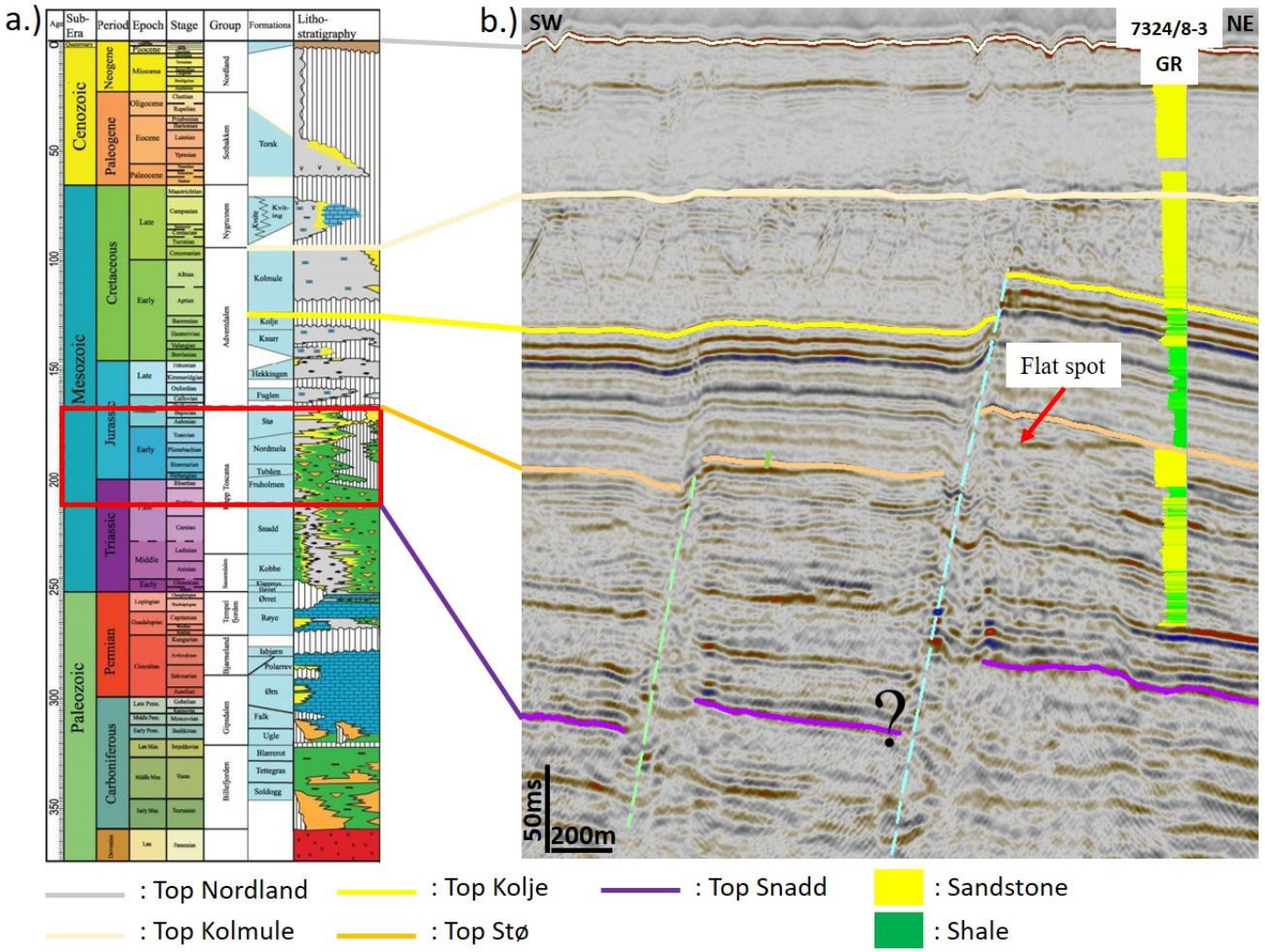

Figure 2.4: Stratigraphic column of the study area. Red rectangle shows the main reservoirs (Stø and Fruholmen Fms) in the study area. Modified after Meunier (2019) and Glørstad-Clark et al. (2010). (b) Cross section showing the Well 7324/8-3 with gamma ray (GR) log, and formation tops. Significant thickness changes are observed in the Kolmule Fm. Flat spot is in the reservoir level of the Stø Fm and it terminates against the fault.

3. Theory

3.1. Seismic data

The acquisition of the high-resolution seismic is based on the P-Cable technology. This technology was patented in 2003 and was commercialized in 2008 (Smith and Mattox, 2020). The P-cable system is made up of 12 to 24 very short streamers dragged by a cross cable that runs perpendicular to the streamers' direction. This design enables the acquisition of multiple seismic profiles at the same time in a cost-efficient way. Unlike the P-Cable, conventional 3D seismic technology is based on very long streamers up to 10km long, with more costly operations (Planke et al., 2009).

Figure 3.1 shows the configuration of the P-cable acquisition method. A paravane is located at each edge and it is designed to span the cross cable. The cross cable is usually placed between 1.25-2.75m below the sea level. The cross cable provides support to 24 active streamers that extend 25-100m. These streamers are spaced 6-15m apart. Switches are attached to the cross cable and located next to the streamers. The system is completed by two tow ropes and signal cables that are attached to the paravanes and the cross cable (Jakobsson et al., 2016).

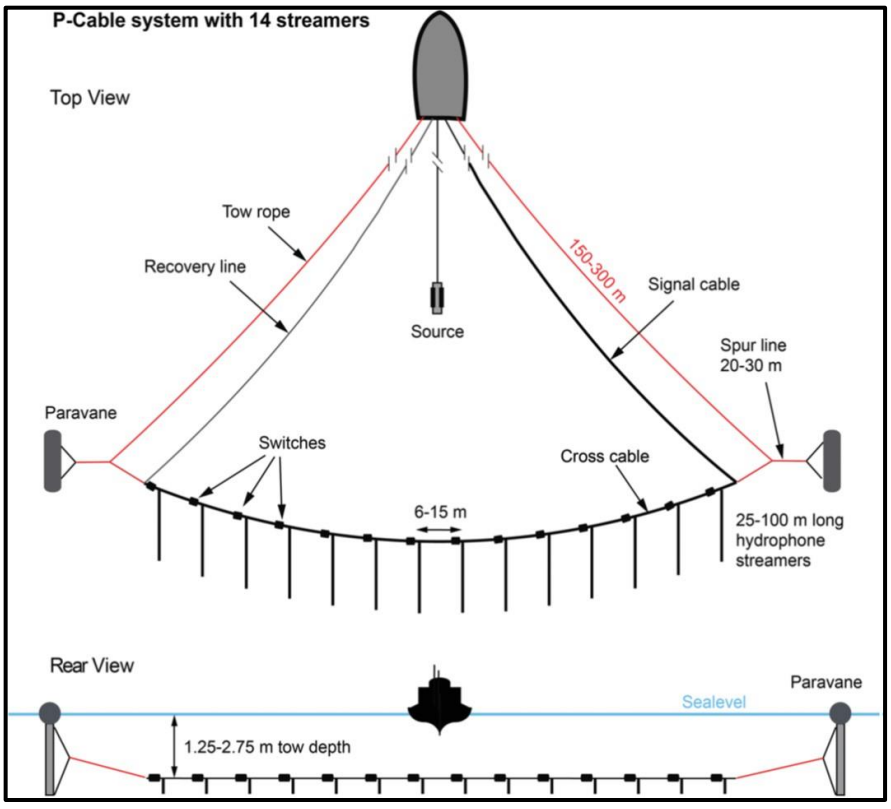

Figure 3.1: Schematic illustration of P-cable acquisition. The main element of the P-cable acquisition is that the streamers are dragged by and are perpendicular to the cross-cable. Small bin sizes result from the small streamers' spacing (6-15m). (Jakobsson et al., 2016).

The use of smaller streamer spacing results in dense common midpoint with bin sizes as small as 6 x 6m or 3 x 3m, whereas the bin size in conventional 3D seismic is 12.5 x 12.5m or 25 x 25m. This configuration allows the P-Cable data to have higher resolution than the conventional 3D seismic data (Jakobsson et al., 2016).

3.1.1. Seismic resolution

The lateral seismic resolution is the ability to distinguish between two features. The vertical seismic resolution defines how thick a layer needs to be in order to be seen in the seismic and it is closely linked to the tuning thickness. The lateral seismic resolution is controlled by the Fresnel zone which is defined by one quarter of the dominant seismic wavelength ($\lambda/4$). The wavelength (λ), velocity (v) and frequency (f) are related to each other in the following way:

$$\lambda = \frac{v}{f} \qquad (1)$$

The seismic velocity increases with depth due to compaction whereas frequency decreases with depth. This is because higher frequencies in the seismic signal are attenuated more with increasing depth than low frequencies (Brown, 1999) (**Figure 3.2**). Therefore, the lateral resolution decreases with depth. The limit of separability or vertical resolution can be estimated as a quarter of the dominant period (T). For a thickness lower than the limit of separability, the amplitudes are gradually attenuated, and it becomes challenging or even impossible to distinguish between top and bottom reflectors in seismic (Brown, 1999).

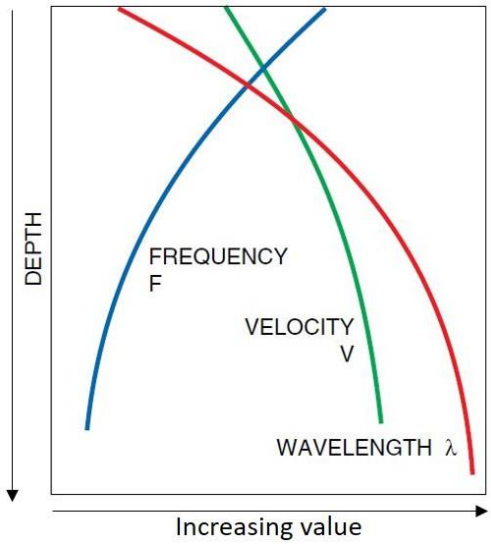

Figure 3.2: Relationship between frequency (f), velocity (v) and wavelength (λ) with depth. Frequency decreases with depth. Velocity and wavelength increase with depth. Increasing wavelength results in lower resolution. Lateral resolution = ($\lambda/4$). Modified after Brown, (1999).

3.1.2. Seismic polarity

Seismic traces result from filtering of the reflection coefficient (RC). This reflection coefficient is controlled by the acoustic impedance (AI), which is a product of velocity (v) and density (ρ) . These relations are defined as:

$$RC = \frac{AI_2 - AI_1}{AI_2 + AI_1} \qquad (2)$$

$$RC = \frac{V_2\rho_2 - V_1\rho_1}{V_2\rho_2 + V_1\rho_1} \qquad (3)$$

Understanding the general relationship between velocity, density, and acoustic impedance is critical for determining the polarity of seismic data. Seismic polarity is generally divided into two standards: American polarity and European polarity. A peak is defined as a "positive or hard" event in the American polarity, and a trough as a "negative or soft" event. In this polarity, an increasing impedance results in a positive amplitude while decreasing impedance produces a negative amplitude (Avseth et al., 2005) (**Figure 3.3**)

As opposed to the American polarity, European polarity defines a peak as a "negative or soft" event, and a trough as a "positive or hard" event. An increasing impedance results in a negative amplitude whereas decreasing impedance produces a positive amplitude. One way to check the polarity is to observe the seabed reflector. The seabed reflector should show an increasing impedance due to an increasing velocity and density from water to sediments underneath. If the seabed reflector shows a peak, the seismic data can be categorized as American polarity. On the other hand, if the seabed reflector shows a trough, the seismic data can be categorized as European polarity (Avseth et al., 2005).

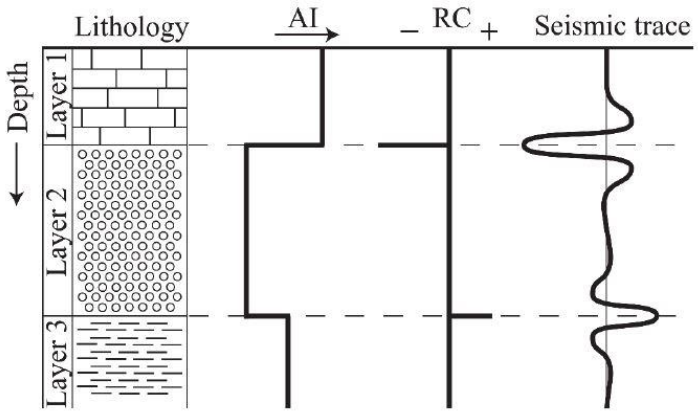

Figure 3.3: An example of American polarity. The seismic trace shows a trough between layer 1 (limestone) and layer 2 (sandstone), which is due to a decreasing impedance from limestone to sandstone. A peak occurs at the boundary of layer 2 (sandstone) and layer 3 (shale). This is due to an increasing impedance from sandstone to shale. Tomasgaard, (2018).

3.2. Seismic well-tie

The first step before interpreting a horizon from seismic data is to establish a relationship between the well and the seismic traces (Bacon et al., 2003). In this process, a synthetic seismogram must match to a real seismic trace in order to correlate features from the well to the seismic data (White and Simm, 2003). The procedure for tying a well to the seismic data are as follows:

1. Check shot calibration

Typically check shots are used for converting well data from the depth domain into the time domain. Often check shots are sparsely sampled. Sonic log calibration introduces additional samples between the check shot points in order to get a more accurate time-depth relationship. However, the sonic log and the seismic are measured at different frequency ranges which may result in too high velocities compared to the seismic velocities (dispersion). Therefore, quite often the synthetic trace derived from the time converted sonic and density log using the calibrated check shots (see below) needs minor adjustments between the check shot points to match the seismic signal (Yadav et al., 2004).

2. Gardner's equation

Gardner's equation is used to predict the density value when it is missing. Gardner et al. (1974) conducted empirical studies determining the relationship between velocity and density: The relation is defined as:

$$\rho = aV^{\frac{1}{4}} \qquad (4)$$

where ρ is density (g/cm^3), a has a value of 0.31 when velocity (V) is given in m/s and 0.23 when V is measured in ft/s.

3. Synthetic seismogram

As mentioned in section **3.1.2**, a reflection coefficient is derived from the changes in the acoustic impedance. In this study, a deterministic wavelet is extracted from the seismic data using the reflectivity derived from the sonic and the density logs. The so-called ISIS frequency wavelet is used in this study. This wavelet extraction minimizes the misfit between the synthetic trace and the seismic trace and therefore produces models with the highest possible amount of coherent signal (Pindel, 2020; Schlumberger 2019). Convolution of this wavelet with the reflectivity series result in the synthetic seismogram.

4. Seismic-well tie

The synthetic seismogram is calculated over the entire log sections down to the area of interest. Quite often the reservoir exhibits poor reflectors, making it difficult to correlate the synthetic and seismic traces. In this case, the seismic events in the overburden become important to correlate. Another reason for matching the synthetic and seismic traces of the overburden is to link the seismic horizons to the well-tops. This makes it easier to correlate seismic events in the area of interest (reservoir interval). The main task in this process is to match a synthetic seismogram peak to a seismic trace peak, or a synthetic seismogram trough to a seismic trace trough (**Figure 3.4**). Stretching and squeezing the synthetic should be avoided as it modifies the time-depth relationship given by the calibrated check shots (White and Simm, 2003). Applying a constant shift to match the synthetic with the seismic, however, is generally acknowledged.

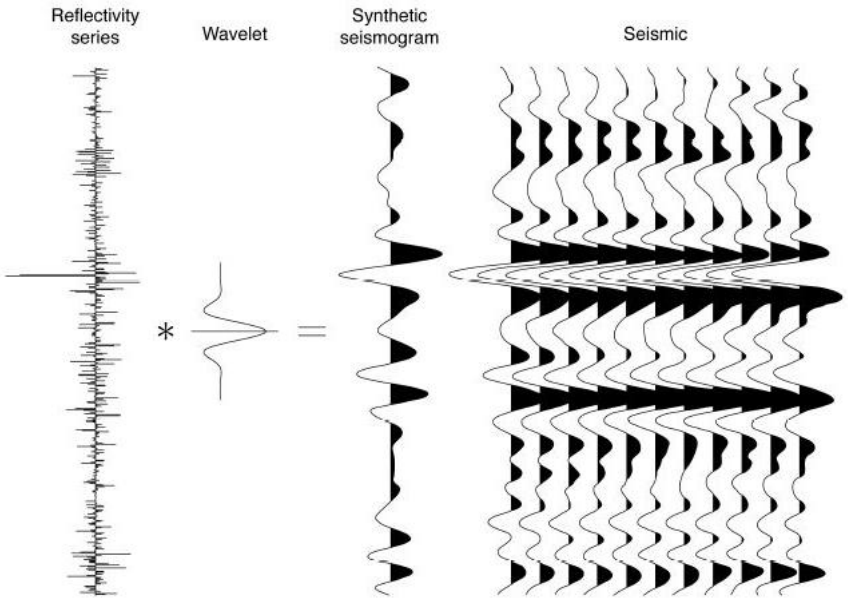

Figure 3.4: The synthetic seismogram results from convolving the reflectivity series with a wavelet. In order to have a good well tie, the peak or trough from the synthetic seismogram should match the corresponding peak or a trough in the seismic trace. Czajkowski, (2015).

3.3. Velocity modelling

In this study, the interpretation was done in the time domain. To be able to build a 3D model for volumetric analysis, horizon and fault interpretation must be converted into the depth domain. Velocity information such as check shots or a seismic velocities cube are not available. The seismic data, on the other hand, are available in the time and depth domains. Based on the interpretation of horizons in both the time and depth seismic cubes, interval velocities between neighbouring surfaces were calculated and were adjusted to their tops at well 7324/8-3. The

resultant velocity model was used for the depth conversion of all interpreted horizons and faults.

3.4. Seismic attributes

3.4.1. Variance

The variance attribute is an edge detection method that estimates the localized variance in the seismic signal. It is calculated in 3D and represents trace-to-trace variability over a specific sample interval. A discontinuity in the seismic horizon produces high-variance coefficients whereas continuous seismic horizons result in low-variance coefficients (Li and Zhao, 2014). The variance of seismic traces is scaled to a value range from 0 to 1. Dissimilar seismic events due to fault offset are mapped as high variance (close to 1), while lowly varying events have a variance coefficient close to 0.

3.4.2. RMS amplitude

The RMS amplitude is an important attribute that can be used to highlight changes of amplitude strength in horizontal and vertical dimensions. Variations in amplitude strength can be used as an indicator for facies variations, channel bodies, hydrocarbon saturated intervals, and other geological features (Almasgari et al., 2020; Ismail et al., 2020). For instance, a sand body embedded in shale may show an acoustic impedance contrast. This contrast may be enhanced in the case of gas or oil pore fill. However, the amplitudes may also be increased in the case the reservoir thickness approaches the tuning thickness.

3.5. Volume of shale

The volume of shale is an important parameter in the calculation of the shale gouge ratio (SGR). The volume of shale can be calculated by several methods, each with its own merits. One of these methods uses a gamma-ray log to determine the shale volume. The gamma-ray log is used due to its ability to measure the amount of potassium (^{40}K), uranium, and thorium in the formation. Potassium is an important element of some clay minerals while thorium is also commonly associated with shale as it tends to be in the shale or silt sized particles (Kennedy, 2015).

The index gamma ray (IGR) is an estimation of the shale volume and is derived from the gamma-ray log. The equation below defines the index gamma ray (IGR) as a linear function of the gamma ray log signal.

$$I_{GR} = \frac{GR_{log} - Gr_{min}}{Gr_{max} - Gr_{min}} \quad (5)$$

However, quite often this linear equation over-estimates the shale volume, resulting in a pessimistic scenario for the reservoir quality. In order to solve this problem, the non-linear equation of Larionov (1969) was used in this study.

$$\textit{Volume of shale} = 0.33 \times (2^{2*I_{GR}} - 1) \quad (6)$$

This equation is expected to perform better when the shales are compacted (Kennedy, 2015).

3.6. Variogram

A variogram model is needed to calculate kriging weights as discussed in sections **3.7** and **3.8**. The variogram model expresses the relationship between two data points which are separated by a distance (h). The variance of all data pairs which have approximately the same separation distance (h) is calculated by the following equation:

$$y(h) = \frac{1}{3N_h}\sum_{i=1}^{N_h}\left((Z_{(i+h)}\right) - (Z_i))^2 \quad (7)$$

where y(h) is called the semi-variance because the summed variance of all data pairs $Z_{(i+h)}$ and $Z_{(i)}$ with separation distance h is divided by $2N_h$ where N is the number of data pairs. The semi-variance (y) increases with increasing separation distance of the data pairs and eventually reaches an upper limit. It has small values if the data pairs are closely spaced. (Ringrose and Bentley, 2015). Note that y(h) represents the mean semi-variance which means that the semi-variance of individual data pairs may be very different from the variogram value given for the same separation distance.

A semi-variogram model commonly known as a variogram is defined by three main parameters: the range, the sill, and the nugget. **Figure 3.5** illustrates the relationship between these three features. The red line represents the variogram model. This is an analytical function that approximates the variogram samples coming from the individual data pairs. The sill is defined as the semi-variance value where the separation distance (lag) is larger than the range. The range describes the distance at which the sill is reached. The variance of data pairs beyond this separation distance is around the sill value. The nugget is the extrapolated semi-variance (y) from the variogram samples to the origin. It can be interpreted as a measure of the uncertainty in the data (Ringrose and Bentley, 2015; Rotar, 2019; Schlumberger; 2017).

Figure 3.6 shows the most common variogram models which are the Spherical, Exponential and Gaussian models. The model is selected to fit best the sample variogram. Note that kriging honours the data only if the nugget is very small. If, for instance, the nugget is set to the sill value, kriging derives a constant value which is the mean of all data points.

In this study, well data was used to generate the vertical variogram. However, the lateral variogram was derived using geological analogues such as the reservoir depositional environment because of lack of wells.

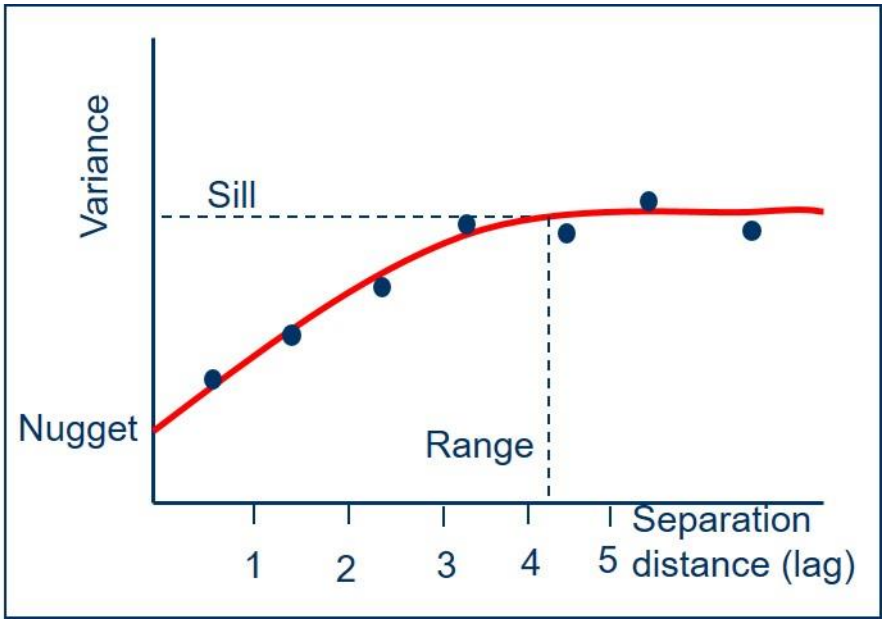

Figure 3.5: A semi-variogram displaying data points, the range, the sill, and the nugget. Red line represents the variogram model. The points represent the mean variance of all data pairs of a specific lag. Generally, the closer two data points are to each other, the smaller the semi-variance value. Schlumberger, (2017).

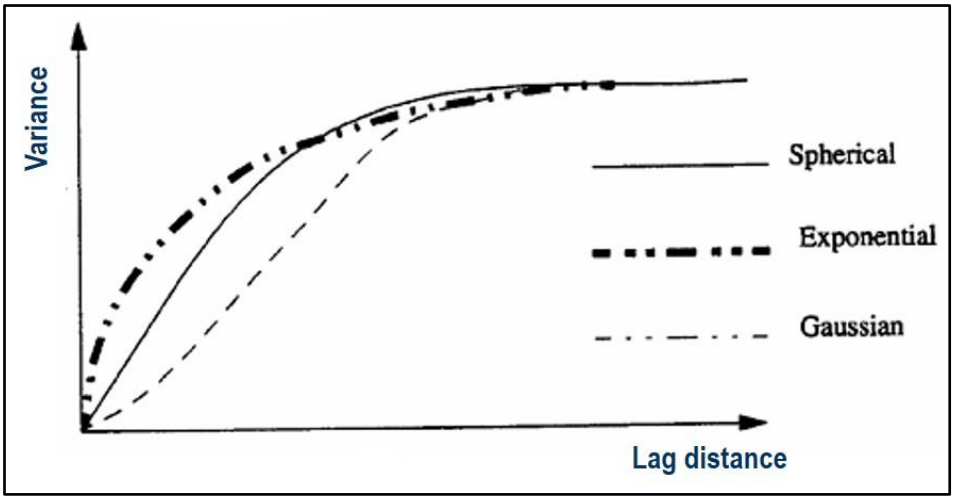

Figure 3.6: The most common variogram models. The spherical has a linear behaviour at shorter distance. The exponential has a steep behaviour at shorter distance. The Gaussian shows a high degree of continuity at short distances and transitions to a more exponential behaviour at longer distances. Schlumberger, (2017).

3.7. Kriging

Kriging is a distance-weighted statistical technique that was developed by Matheron and Krige in 1963 (Doyen, 2007). Kriging estimates the unknown value at each location using a combination of the well data (known values) and a variogram model derived from the data points. The variogram model is used to calculate the Kriging weights needed for interpolation of the data points. The Kriging weights will decrease as they move closer to the variogram range (Schlumberger, 2017). **Figure 3.7** illustrates how the Kriging algorithm works. At location (X_0) we want to estimate its value using the known values (X_i). In order to calculate the value at (X_0), the following formula is used:

$$Z(X_0) = \sum_{i=1}^{n} \omega_i Z(X_i) \qquad (8)$$

where Z(X_0) is the unknown value at point (X_0), ω_i is the kriging weight calculated using the variogram model and Z(X_i) is the known value at location X_i.

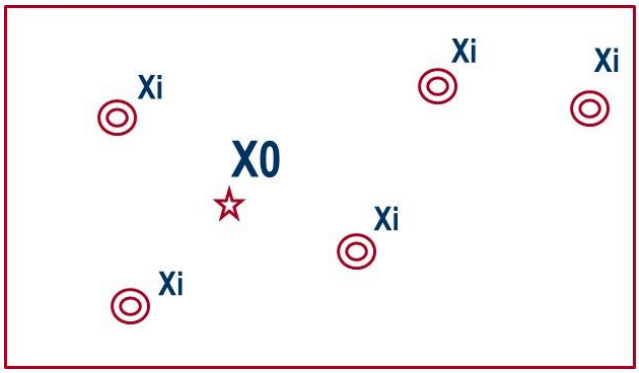

Figure 3.7: Illustration of the kriging algorithm. X_0 is the unknown value that will be estimated using a combination of well data (X_i) and the variogram model. Schlumberger (2017).

Several kriging algorithms exists. In this study, we use simple kriging.

$$Z(x_0) = \sum_i^n w_i\, Z(x_i) + [1 - \sum_i^n w_i]m \qquad (9)$$

Z(X_0) is the value at location X_0 to be calculated, Z(X_i) are the existing data points at location X_i, ω_i is the weights assigned to the data at location X_i, and m is the mean value derived from all data points. The sum of all weights may have a maximum value of 1. When all weights are zero, simple kriging delivers the mean value. Thus, simple kriging does not take the trend of the data into account.

3.8. Indicator Kriging

In this study, Indicator kriging was used to generate a facies model. Indicator kriging estimates the probability of encountering specific facies at a location. The following formula explains the underlying algorithm when calculating the sand probability:

$$P_{sand}(X_0) = \sum_i w_i I_{sand}(X_i) + (1 - \sum_i w_i) p_{Sand}^{Global} \qquad (10)$$

where the $P_{sand}(X_0)$ is the probability of sand at location X_0, I_{sand} is the sand indicator, p_{Sand}^{Global} is the global probability fraction derived from facies logs, and $\sum_i w_i$ is the sum of the weights. The facies at the wells gets the value of 1 if it is sand, and 0 if it is not sand. The global probability typically represents the facies fractions given by the well-logs and is used like the mean value in the simple kriging. For each facies, the probability is calculated at X_0. Finally, the facies with the highest probability is assigned to location X_0 (Schlumberger, 2017).

3.9. Fault seal mechanism

Faults are an important element in the entrapment and movement of hydrocarbons. Reservoir juxtaposition against impermeable horizons and the development of a high sealing capacity fault rock can create barriers to fluid flow (Fisher and Knipe, 1998). Yielding et al. (1997) propose a two-order step to conduct seal analysis. The first step of seal analysis is to determine the reservoir juxtaposition zones on the fault surface using the mapped horizons. The second step is to analyse a potential pressure difference within the sand-sand juxtapositions using the shale gouge ratio (see chapter **3.9.3**) and smear factor (chapter **3.9.2**). The shale gouge ratio is an estimation of shale coming from a wall rock to the fault zone, whereas the smear factor estimates the shale thickness that is drawn along the fault zone during faulting (Yielding et al., 1997).

Several mechanisms have been identified by which faults can act as seal (Knipe, 1992; Watts, 1987; Yielding et al., 1997). These mechanisms are:

1. Juxtaposition: Reservoir sands juxtaposed against a non- or low permeable unit
2. Shale smear: entrainment of shale into the fault zone, which results in a high capillary entry pressure of the fault itself.
3. Cataclasis: crushing of sand grains to produce a fault gouge consisting of finer grained material and therefore resulting in high capillary entry pressure of the fault.
4. Diagenesis: Cementation along the initially permeable fault plane may remove some or all the porosity, resulting in a hydraulic seal.

In this thesis, only the juxtaposition and shale smear mechanism will be discussed. This is because of the time constraint and lack of data to support an investigation on cataclasis and diagenesis.

3.9.1. Allan diagram

The juxtaposition diagram, also known as the Allan diagram, is a fault plane that depicts the lithology that comes into contact across the fault plane as a result of fault displacement (Allan, 1989; Clarke et al., 2005). The interpretation of the Allan diagram is based on three assumptions: (1) the fault itself does not have sealing properties, (2) the fault is not an open conduit, and (3) the trapping and migration relationships at the fault depend on the fault-juxtaposed stratigraphy. Therefore, a permeable zone juxtaposed against an impermeable zone is assumed to provide a seal in a structural closure, whereas juxtaposition of two permeable zones causes hydrocarbons to move across the fault (Allan, 1989).

The Allan diagram generates a two-dimensional model representation of the three-dimensional fault body (**Figure 3.8a)**. The lithology from the footwall and the hanging-wall are projected onto the fault plane and used to define the reservoir juxtaposition (**Figure 3.8b**).

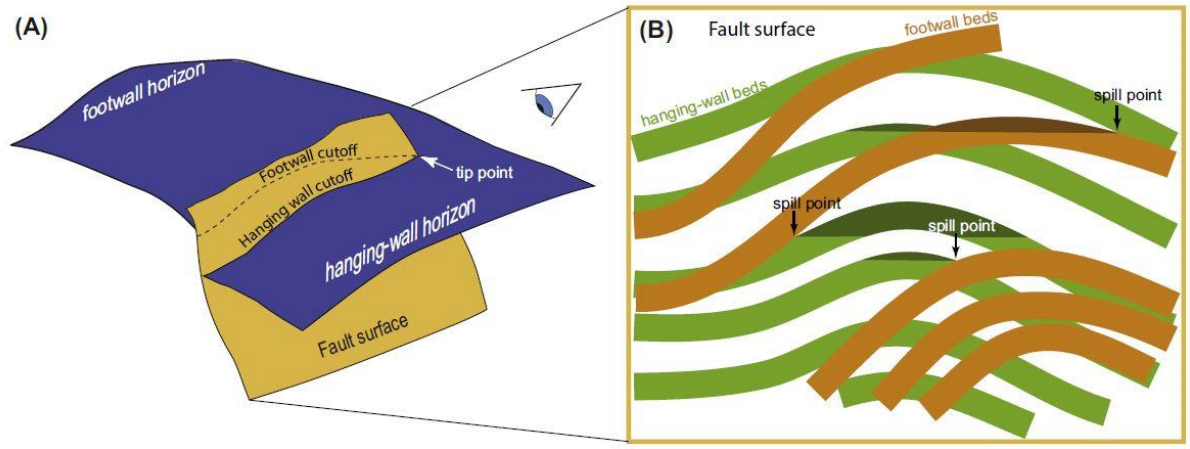

Figure 3.8: (a) Blue horizon is cut by yellow fault. The smallest throw is at the fault tip whereas the largest throw is at the center of the fault. Horizons from footwall and hanging wall are marked by the cutoffs. (b) Corresponding Allan diagram. Several hanging wall and footwall zones are projected onto the fault. All colored zones are reservoir units. Footwall beds are indicated by the brown colour whereas hanging-wall beds are in green. The shale layers are white. Spill points are marked at the intersection of hanging-wall and footwall reservoirs. Hydrocarbon will move through the spill points if the maximum hydrocarbon column height is reached. Ketterman et al. (2019), modified after Allan (1989).

3.9.2. Shale smear

Weber et al. (1978) conducted a series of shale smears observations from experiments and outcrop studies. A shale smear is a laminar volume of phyllosilicate-rich material that enters the fault zone. Faulting of sand-shale sequences can result in the formation of a continuous, multi-layered shale gouge across the fault plane. The thickest shale gouges observed by Weber et al. (1978) were about 0.5 m, derived from source beds that were 5 m thick. The shale gouge zone also becomes gradually thinner farther away from the source bed (Weber et al., 1978). The age of faulting has also an impact on creating the shale smears. Syn-depositional faulting is more likely to create shale smears along the fault plane. This is because deposition of the undercompacted shale occurs around the same time as faulting, and hence the undercompacted shale is more prone to smear (Harding and Tuminas, 1989; Knott, 1993).

Three types of shale smear are defined by Lindsay et al. (1993): (1) shear smear where the thickness of the smear decreases farther away from the source beds, (2) abrasion smear, which is the most common type, where the shale from the source bed is abraded and mixed with sand in the fault rock, and (3) injection smear which are caused by volume changes during faulting. In addition, Yielding et.al. (1997) stated that more source beds result in more continuous smear (**Figure 3.9**). For all these types, the shale smear is more likely to break as the fault throw increases (Ketterman et al., 2019; Lindsay et al., 1993; Yielding et al., 1997).

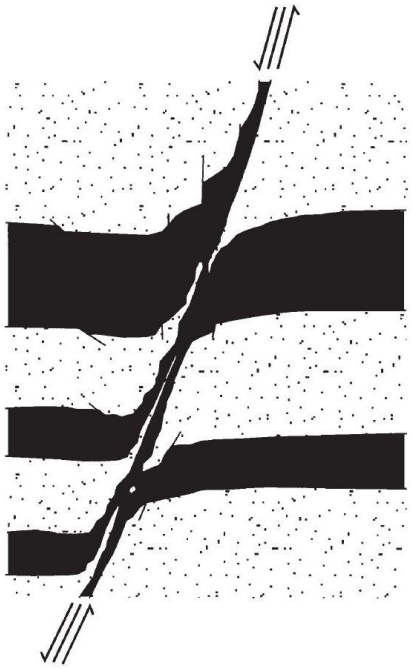

Figure 3.9: Example of Shale smear. Black layers represent the shale beds. Shale smear coming from multiple source beds into a normal fault, resulting in a more continuous shale smear. Yielding et al. (1997), modified after Weber et al., (1978).

3.9.3. Shale gouge ratio (SGR)

In general, the shale gouge ratio (SGR) is based on a model where the shale is smeared along the fault. Yielding et al. (1997) introduced two formulas to calculate the shale gouge ratio (**Figure 3.10**). The first formula is simpler and is based on the ratio of the thickness of the shale that is offset and the fault throw. The second formula is based on the ratio of reservoir thickness times the shale volume fraction and the fault throw. In this thesis, the second formula is used to calculate the shale gouge ratio.

$$\text{SGR} = \frac{\sum(\textit{Shale bed thickness})}{\textit{Fault throw}} \times 100\% \quad (11)$$

$$\text{SGR} = \frac{\sum(\textit{Zone thickness}) \times (\textit{Zone shale fraction})}{\textit{Fault throw}} \times 100\% \quad (12)$$

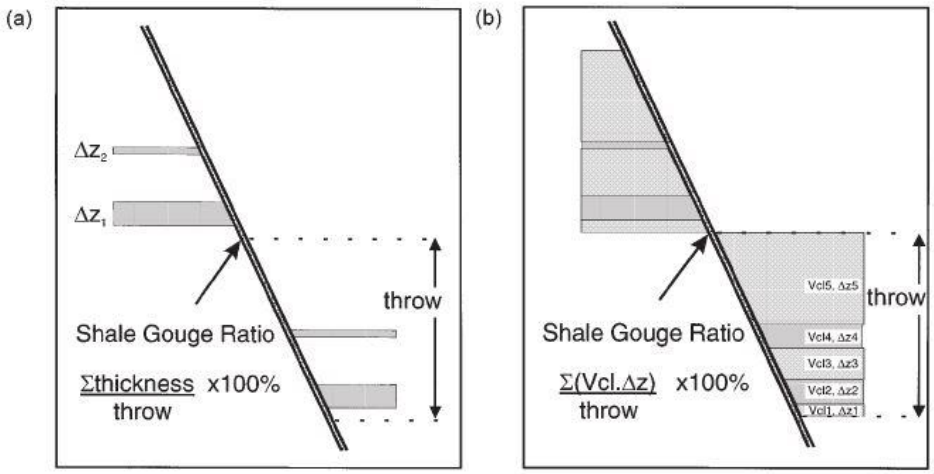

Figure 3.10: (a) A schematic diagram showing the calculation of SGR for explicit shale beds. Δz is the thickness of each shale bed. (b) Calculation for a sequence of reservoir zones. Δz is the thickness of reservoir zones and shale. Vsh is the shale volume fraction in the zone. Yielding et al. (1997).

The shale gouge ratio indicates how much shale enters the fault zone. The more shaly the wall rocks are, the greater the proportion of shale in the fault zone, and the higher the fault's capillary entry pressure. The capillary entry pressure is the pressure needed by the hydrocarbon to overcome the capillary force of the water in the pore space of the fault zone. This value increases with decreasing pore size, and consequently a fault zone can successfully form a seal if it is filled with shale. The shale gouge ratio can be applied either to the footwall or the hanging-wall. If the calculation is applied to both footwall and hanging-wall, the throw and the sum of the SGR in the footwall and hanging-wall need to be divided by two in order to get the average shale gouge ratio (Yielding et al., 1997). The calibration from a number of datasets from different fields reveals that a SGR value of 15-20% is the threshold at which smear continuity is still sufficient for sealing (Clarke et al., 2005; Yielding, 2002).

4. Data

The data used in this study consist of two 3D high-resolution seismic cubes and two 3D low-resolution seismic cubes in time and depth domain (**Figure 4.1**). The high-resolution data was acquired in 2014 in block 7234 of the Norwegian Barents Sea. The seismic survey covers an area of 16km^2 encompassing the Wisting field. The dataset was obtained by OMV Norge AS and at present, it is publicly available via DISKOS. All seismic cubes have American polarity in which the seabed corresponds to a hard kick which is displayed as a positive amplitude. In the high-resolution seismic, the frequencies range from 7 to 185 Hz, while in the low-resolution seismic, the frequencies range from 10 to 70 Hz (**Figure 4.2**). The frequency ranges are taken from the -10dB points. Several wells are included in the dataset. However, the study area has only one well (7324/8-3). Well-tops and well-logs are available from this well. However, checkshots, facies and porosity logs are missing (**Table 4.1**).

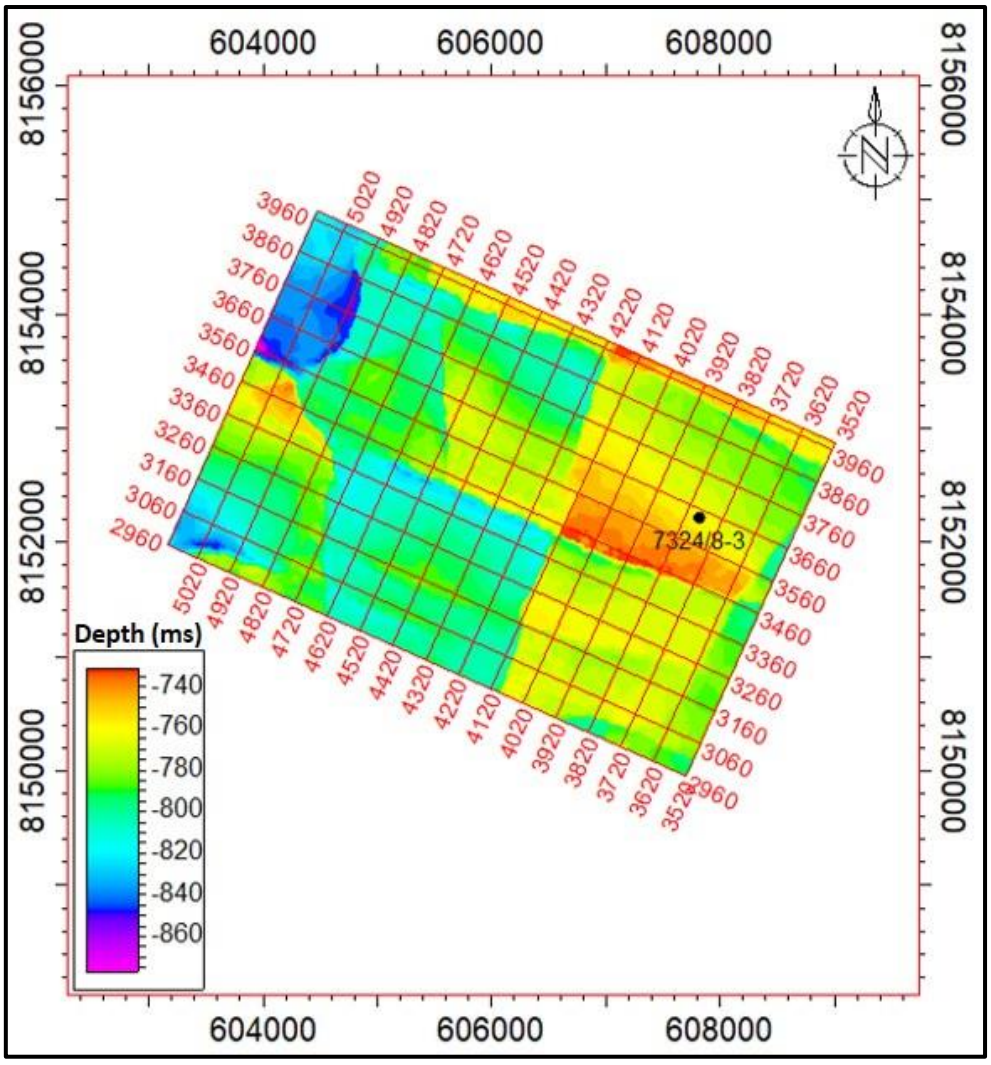

Figure 4.1: Structure map showing the top Stø Fm, the location of well 7324/8-3, and the extension of the 3D seismic surveys. Red lines are seismic Xlines and inlines.

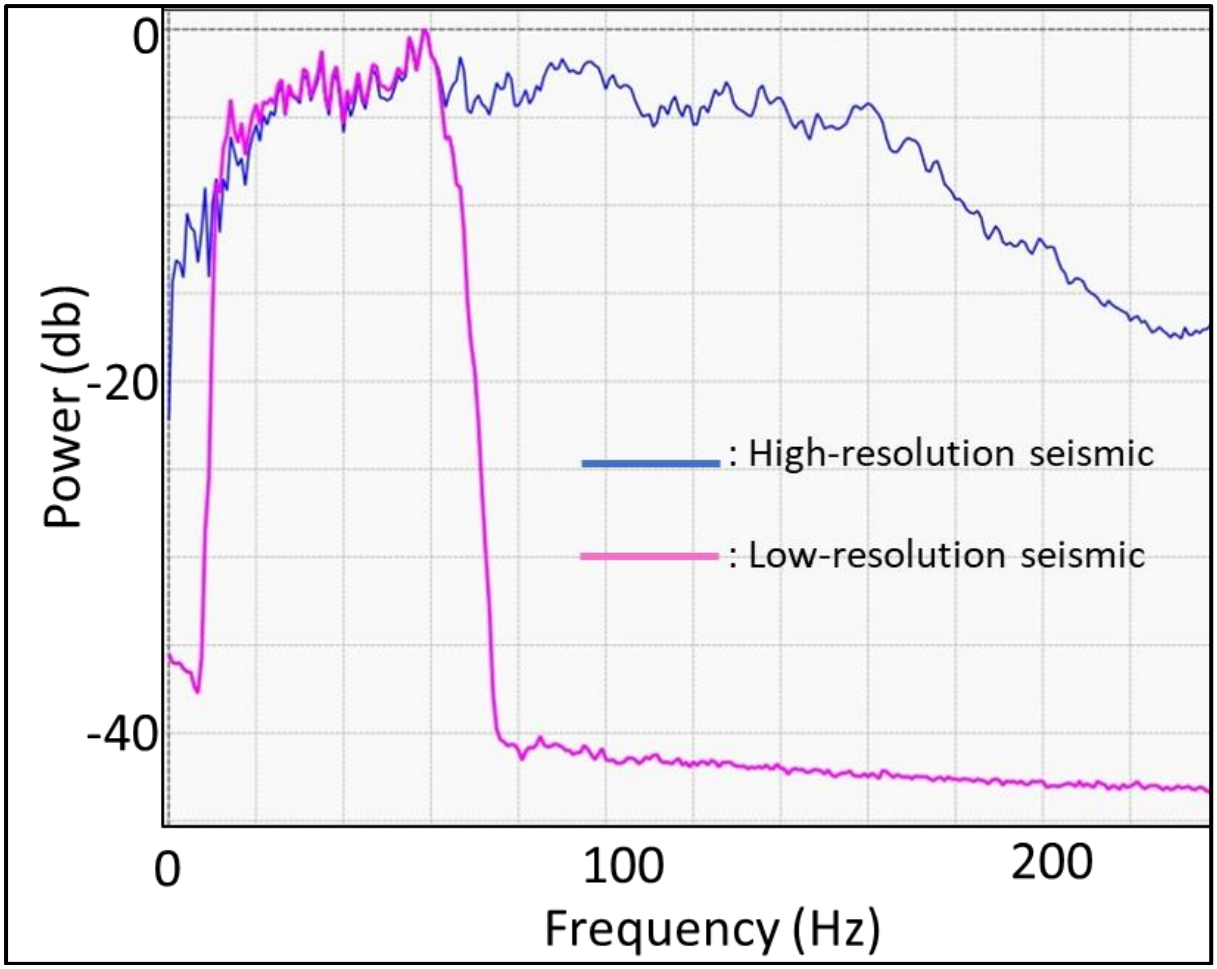

Figure 4.2: Power spectrum of both datasets. High-resolution seismic (blue), low-resolution seismic (purple).

Table 4.1: Overview of the available well with well-logs

Well	Checkshots	GR	Resistivity			Neutron	Density	Facies	Porosity
			Micro	Medium	Deep				
7324/8-3		X	X	X	X	X	X		

5. Methodology

5.1. Well-log interpretation

Well-log interpretation was conducted to describe the lithology, fluid contacts, and to distinguish reservoir levels and shale zones. Sandstones are characterized by relatively low gamma ray values (<90 gAPI) whereas shales are defined by high gamma ray values (>90 gAPI). This threshold was used to make a facies log for facies modelling in section **5.6.2**. A crossover display of the density and neutron log allows identifying the sandstone zones. Resistivity logs were used to confirm the hydrocarbon at the Stø reservoir level. High values of resistivity indicate hydrocarbon content (**Figure 5.1**). The volume of shale was derived using gamma-ray in the following way: Firstly, the linear equation (Eq .5) was used to calculate the index gamma-ray. Then, the non-linear formula of Larionov (1969) for older rocks was used to calculate the shale volume (Eq. 6). This formula was used because the reservoir was deposited in the Middle Jurassic.

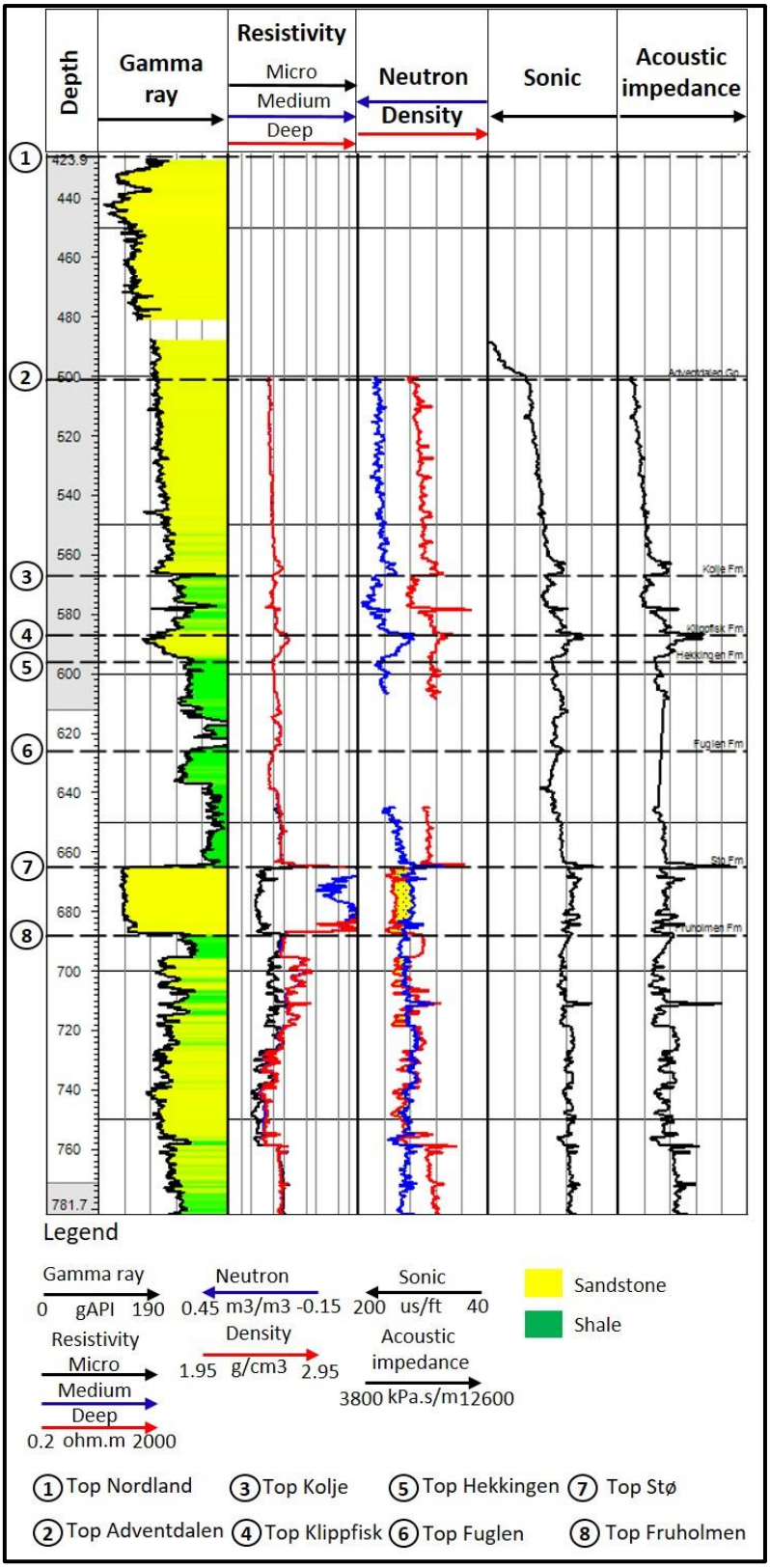

Figure 5.1: Well 7324/8-3 with gamma-ray, resistivity, neutron, density, sonic, and acoustic impedance logs. Main reservoirs tops are marked with numbers 7 (top Stø) and 8 (top Fruholmen). Note that in the Stø reservoir level, resistivity logs show high value, indicating the hydrocarbon accumulation. Cross-over in the neutron-density logs marked by yellow colour indicates the sand zone. The acoustic impedance value where the density log is missing was calculated using Gardner's equation.

5.2. Seismic-well tie

Check shot calibration was made in the well 7324/8-3. The checkshots were derived from the seismic horizons interpreted in the time and depth domains. The drift points derived from the check shot points and the corresponding time points derived from the sonic log were linearly interpolated. A deterministic wavelet (ISIS frequency) was extracted from each seismic time cube. Both wavelets are in zero phase (**Figure 5.2**). The wavelets were used to construct the synthetic trace for the low- and high-resolution seismic **(Figure 5.3)**. The Gardner equation was used to fill the depth range where the density log is missing.

Several key reflectors were compared with the synthetic reflectors to check if the synthetic traces on the well match the seismic and the well-tops. These reflectors are the top Kolje, top Fuglen, and top Stø. **Figure 5.3** shows the seismic well-tie in well 7324/8-3. The top Kolje is characterized by a strong negative amplitude and can be tracked throughout the study area. The top Fuglen is identified by a small positive amplitude. The Fuglen Fm consists of a 38m thick shale layer in the study area.

The sandstone reservoir in the Stø Fm has a thickness of ~ 20m (**Figure 5.1**). Unlike the top Fuglen, the top Stø is characterized by a soft kick resulting in a negative amplitude reflector. This is due to the changes of acoustic impedance from high values of the shale (top Fuglen) to the low values of the sand reservoir (top Stø) (**Figure 5.3**).

The seismic well-tie both in the low- and high-resolution seismic gives a good match between the synthetic trace and the seismic trace. However, the high-resolution data show more reflectors than the low-resolution data. For instance, in the reservoir level of the Stø Fm, several synthetic events can be observed in the high-resolution seismic, whereas in the low-resolution seismic, the same reservoir is only characterized by a peak and a through.

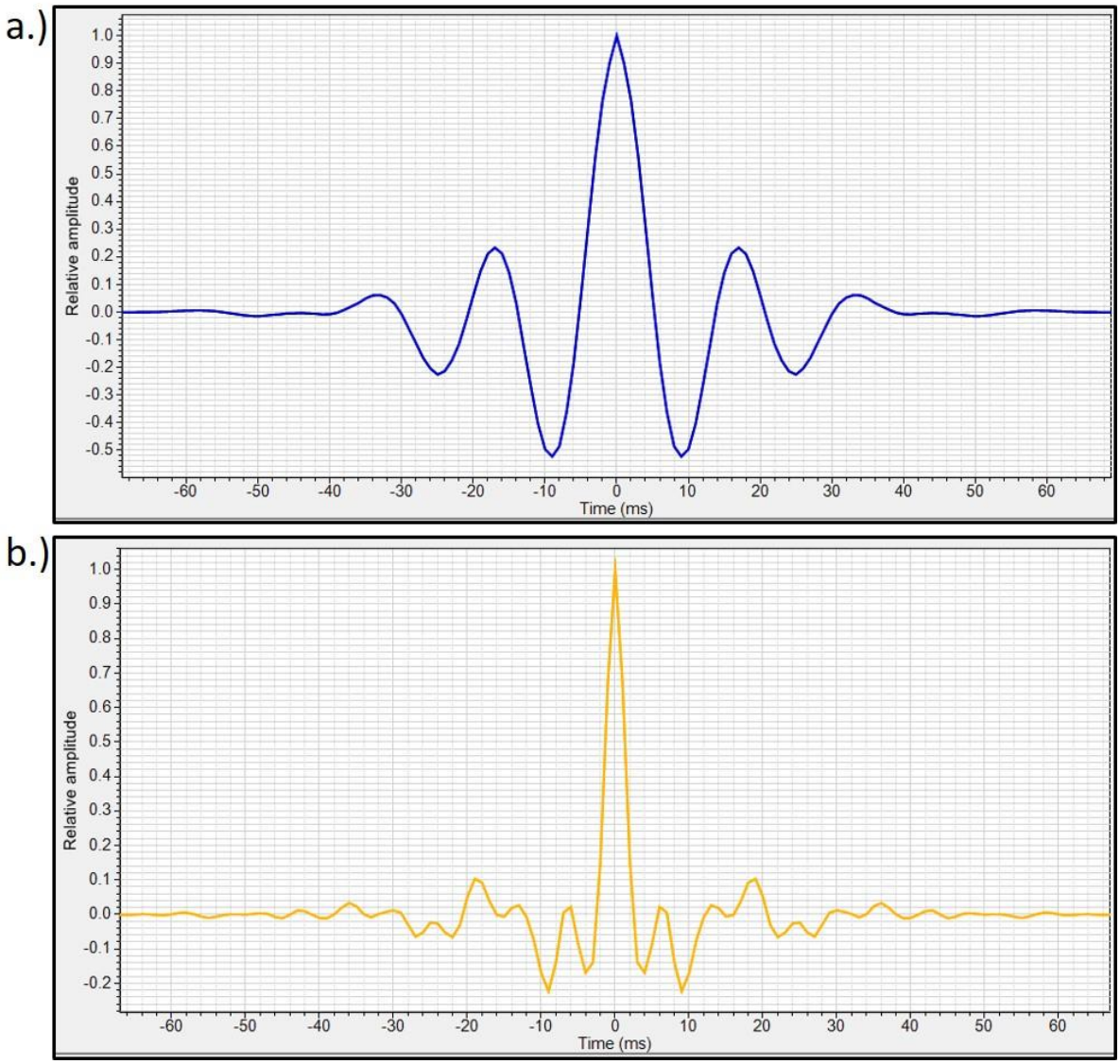

Figure 5.2: ISIS wavelet for the (a) low-resolution, and (b) high-resolution seismic. Note that the wavelet of the low-resolution seismic is characterized by large side lobes, while in the high-resolution seismic, the side lobes are smaller. The spread of the main lobe together with the size of the side lobes define the seismic resolution.

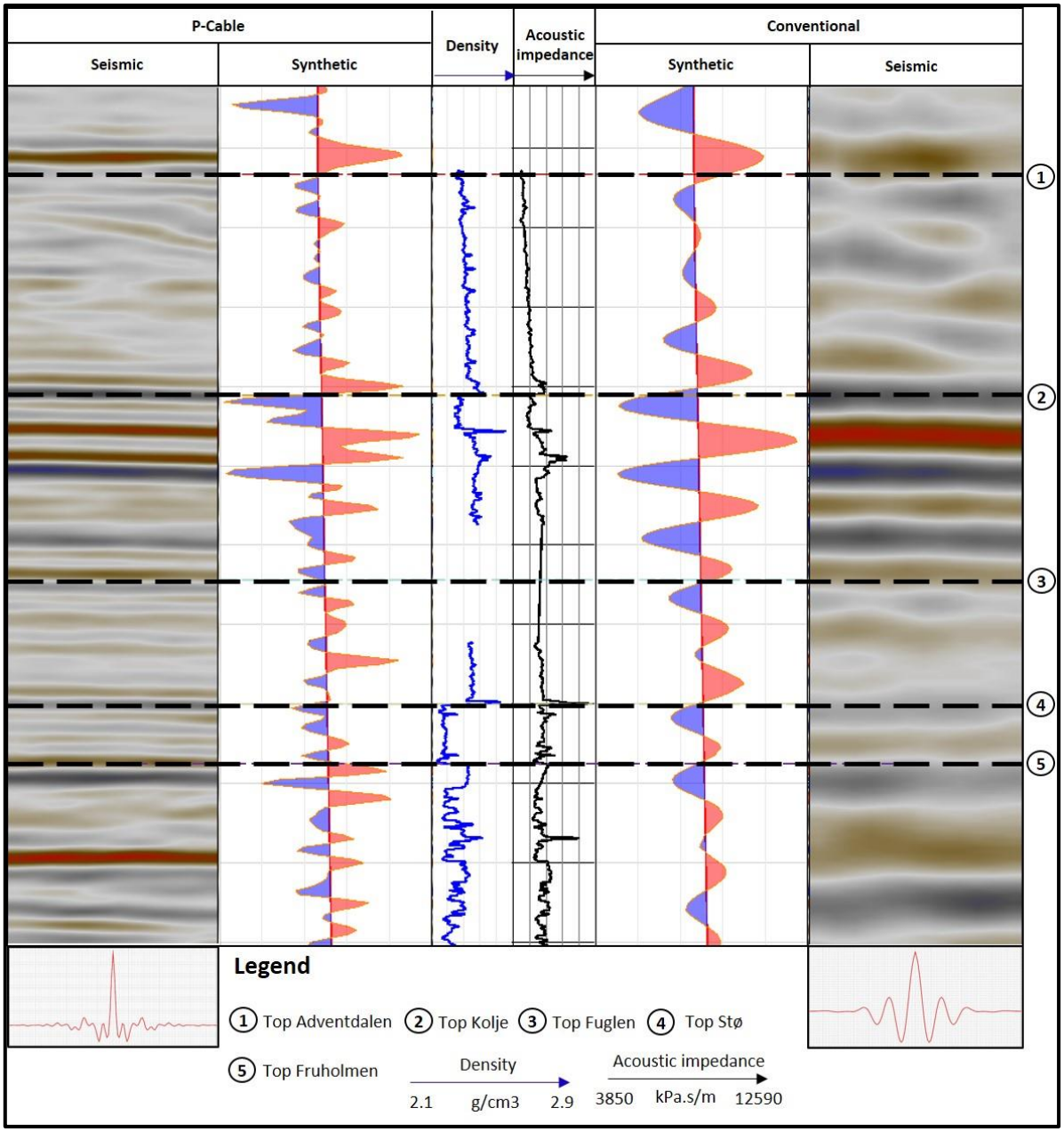

Figure 5.3: Comparison of seismic-well tie between P-cable data (high-resolution) and conventional data (low-resolution). Synthetic traces (peaks and trough) are found richer in the P-cable data. P-cable data gives more information of reservoir heterogeneity in the Stø Fm (between horizon 4 and 5) than in conventional data. Figure left to right (high-resolution seismic, high-resolution synthetic, density log, acoustic impedance log, low-resolution synthetic, low-resolution seismic). Each wavelet below the seismic sections represents the seismic resolution.

5.3. Seismic interpretation

The seismic interpretation was conducted in the low- and high-resolution seismic in the time domain. The study area is located at a tilted fault block and includes one well (**Figure 5.4**). This area is used to quantify the horizon uncertainties, to build the structural models, and to conduct structural analysis.

Fault interpretation was conducted in the initial phase. This interpretation was guided by the seismic variance attribute. In addition, the variance attribute was used to understand the fault network and to interpret the intersections of the faults (branch lines). This attribute was applied to the 3D seismic cubes of the low- and high-resolution seismic.

The seismic interpretation started by observing the seabed reflectors to check the seismic polarity. As mentioned before, the seismic is in American polarity. After defining the seismic polarity, the key horizons including the top Kolje, Fuglen, Stø, Fruholmen and mid-Fruholmen were mapped. These horizons are used both in velocity modelling and reservoir modelling. The selection of these horizons was based on the observation that they could be tracked reliably within the study area. A combination of manual and guided auto-tracking was applied when interpreting the horizons.

A flat spot was identified next to a fault and up dip of the well 7324/8-3. This flat spot is located inside the Stø reservoir zone in a tilted fault block (**Figure 5.4; Figure 5.5**). However, the flat spot can only be identified in the high-resolution seismic (**Figure 5.5**). An RMS amplitude surface was also generated to map this hydrocarbon accumulation.

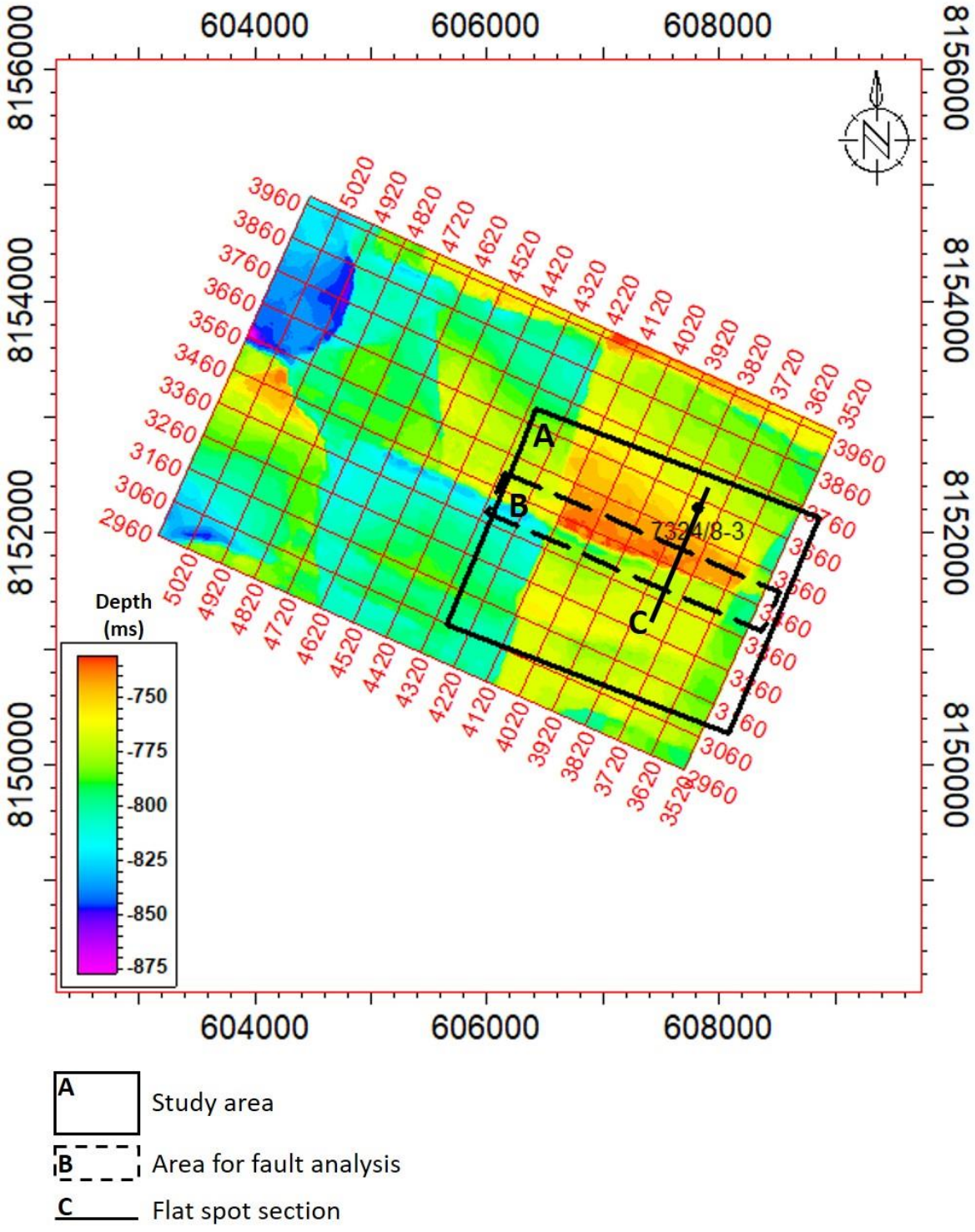

Figure 5.4: Structure map of the top Stø and well 7324/8-3. Black square (A) shows the study area and grey rectangle (B) shows the area for fault analysis. Line (C) is the section shown in figure 5.5. Note that the well 7324/8-3 is located at a northernly tilted fault block.

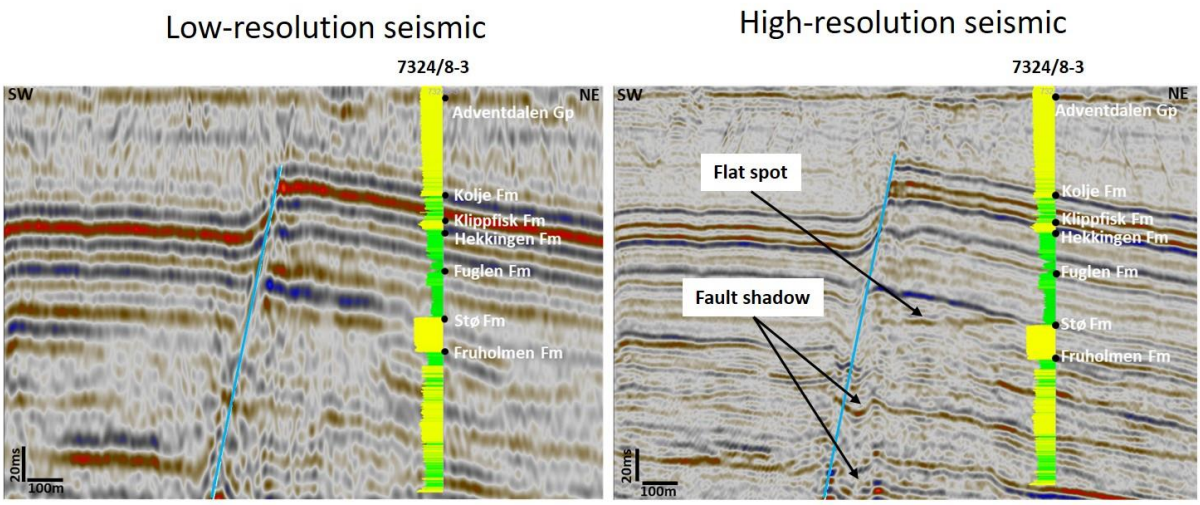

Figure 5.5: (left) low-resolution, and (right) and high-resolution seismic section. The navigation is shown in figure 5.4. Both sections show well 7324/8-3 with gamma-ray log and well-tops. Yellow in the gamma-ray is sandstone while green is shale. Notice that the flat spot is only displayed in the high-resolution seismic. This fluid contact is located in the Stø Fm updip of the well and terminates against the fault.

5.4. Horizons uncertainties

Horizon uncertainties were estimated by subtracting the same interpreted horizons from the high and low-resolution data. As mentioned before, these horizons are the top Kolje, top Fuglen, top Stø, and top Fruholmen. These four reflectors were chosen due to their presence in the well-tops and their wide distribution in both datasets. The interpretation was carried out in the northern segment around the well 7324/8-3. The high-resolution data display a 'fault shadow' zone in the footwall near the fault (**Figure 5.5**). This is an area where the seismic becomes unreliable. It results from rapid lateral velocity changes between the hanging wall and the footwall and commonly occurs in the footwall of the fault (Fagin, 1996; Hardwick and Rajesh, 2013). In this study, this area was trimmed to make sure that the uncertainties do not arrive from mis-interpreted horizons.

5.5. Depth conversion

5.5.1. Velocity modelling

To be able to build a structural model, faults and time surfaces were converted from the time to the depth domain. For this purpose, velocity modelling was done for the low- and high-resolution data. As no velocity data are available for this study, the velocity model had to be constructed from the horizons tracked in time and depth from the high- and low-resolution data. These horizons are the seabed, top Kolje, top Fuglen, and top Stø. The resultant velocity model represents interval velocities defined by the assigned time and depth surfaces. This model allowed us to convert the faults and the remaining time surfaces into the depth domain. The

results in the depth domain were checked against the depth seismic to make sure that the faults and horizons match the seismic events in depth.

5.6. Geomodel building

5.6.1. Structural modelling

Once the depth conversion was done, the next step was to construct the structural model. Two structural models were built based on the interpretation of the low- and high-resolution seismic data. Structural analyses such as Allan diagram, shale smears, and shale gouge ratio were carried out to analyse the sealing behaviour of the largest fault in the model. In addition, the fault network, fault cut-offs and fault throw were analysed to check the quality of both low and high-resolution models.

The process of constructing the structural model consists of several steps: fault modelling (**Figure 5.6a**), horizon model construction and refinement (**Figure 5.6b**), and finally structural gridding **(Figure 5.6c)**. The depth converted faults from both datasets have to be converted to a fault framework. Of critical importance is that the faults intersecting each other are correctly connected (**Figure 5.6a**). This operation was done by using the variance attribute and surface maps as a guide. The model boundary was set around the area of interest which is located at the southeast part of the Wisting field covering two fault compartments (area A of **Figure 5.4**). This area was chosen due to the following reason: firstly, it shows a flat spot up dip of the well (**Figure 5.5**), and secondly there is hydrocarbon which is identified by high resistivity values (**Figure 5.1**). These observations were supported by the RMS amplitude which displays this area as a high amplitude (**Figure 6.4**).

Figure 5.6b illustrates the model construction processes. In this step, the depth-converted horizons are integrated into the fault framework. For the high-resolution data, the modelled horizons are the top Kolje, top Fuglen, top Stø, inner reservoir 1, inner reservoir 2, top Fruholmen, and mid Fruholmen (**Table 5.2**). However, as mentioned before, in the low-resolution model, the horizons within the reservoirs are missing because they cannot be identified in the seismic (**Table 5.1**).

Well-tops were used to adjust the modelled horizons. As mentioned before, horizon data within the fault shadow area were filtered out because of the poor seismic signal to noise ratio. Instead, this area was modelled by extrapolating the data outside the shadow zone into the fault plane. Once the model construction was done, quality control was needed to check for

inconsistencies in the structural framework such as not correctly connected faults or mismatches between the vertical fault extension and the fault throw at the fault edges.

The next step is model refinement. The refinement of the model horizons involves a re-meshing step, a data fitting, and a smoothing operation. Based on the resultant structural model, a 3D grid was built (**Figure 5.6c**). In this step, the grid size was set to 25 x 25m to capture the morphology of the seismic horizons sufficiently. The same grid resolution was selected for the low- and high-resolution model. The layer thickness of each zone which defines the vertical resolution of the model was set to ca. 2m (**Table 5.1, 5.2**).

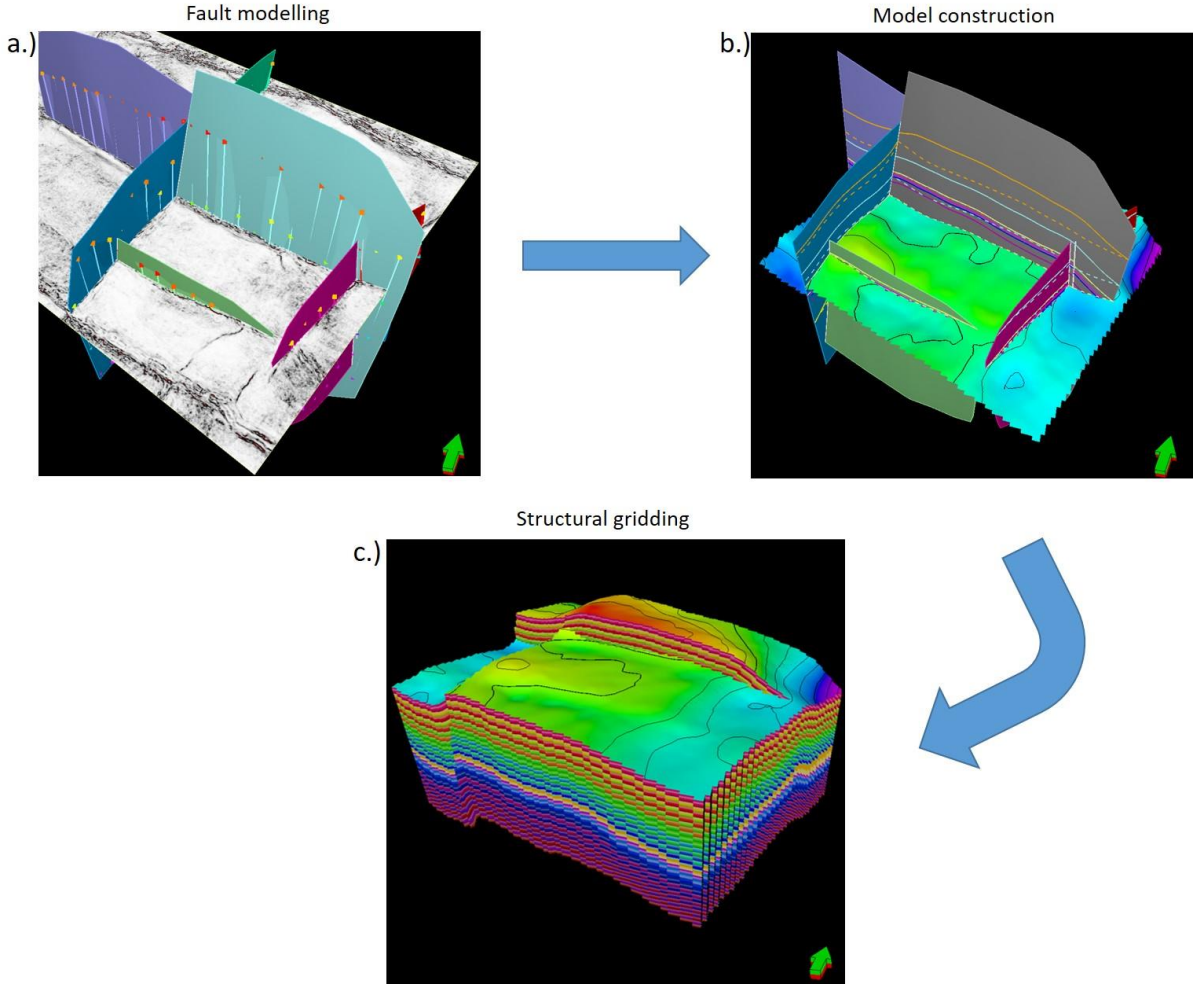

Figure 5.6: (a) Fault modelling processes. (b) Model construction. (c) Structural gridding. Number of layers and grid sizes are inserted in the structural gridding process.

Table 5.1: Number of layers in the low-resolution model

Seismic	Number of layers			
	Top Kolje – Top Fuglen	Top Fuglen – Top Stø	Top Stø – Top Fruholmen	Top Fruholmen – Top Mid Fruholmen
LR	25	20	8	30

Table 5.2: Number of layers in the high-resolution model

Seismic	Number of layers					
	Top Kolje – Top Fuglen	Top Fuglen – Top Stø	Top Stø – Top IR 1	Top IR 1 – Top IR 2	Top IR 2 – Top Fruholmen	Top Fruholmen – Top Mid Fruholmen
HR	25	20	2	2	4	30

5.6.2. Facies modelling

For this study, facies logs were not available and had to be interpreted mainly with the help of the gamma-ray log. Once this was done, the facies log was upscaled into both models. Facies modelling was conducted to capture the lateral and vertical distribution of each lithology. Indicator kriging was used to model the facies. The horizontal major and minor variogram ranges were set to 3000m and the vertical range to 12m. The horizontal ranges were estimated from the reservoir conceptual model (Stø Fm) which describes the reservoir as being deposited in a shoreface environment that covers a large area. **Figure 5.7** shows the vertical range (12m) which was derived from the sample variogram of the facies.

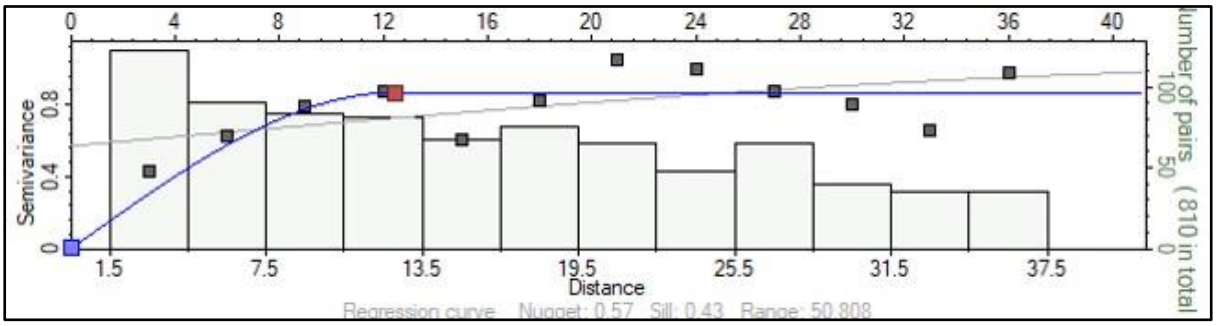

Figure 5.7: The vertical variogram for facies modelling. The blue line represents the variogram model whereas the points are the averaged semivariance of the data pairs. The red point indicated the variogram range.

5.6.3. Property modelling

The volume of shale was modelled because it is needed for fault seal analysis. The modelling was based on kriging using a horizontal variogram range of 3000m and a vertical variogram range of 12m (**Figure 5.8**). Petrophysical properties such as porosity were not included in the model because the porosity log data are missing. These data would have

potentially allowed to make a more detailed comparison between the low- and high-resolution data.

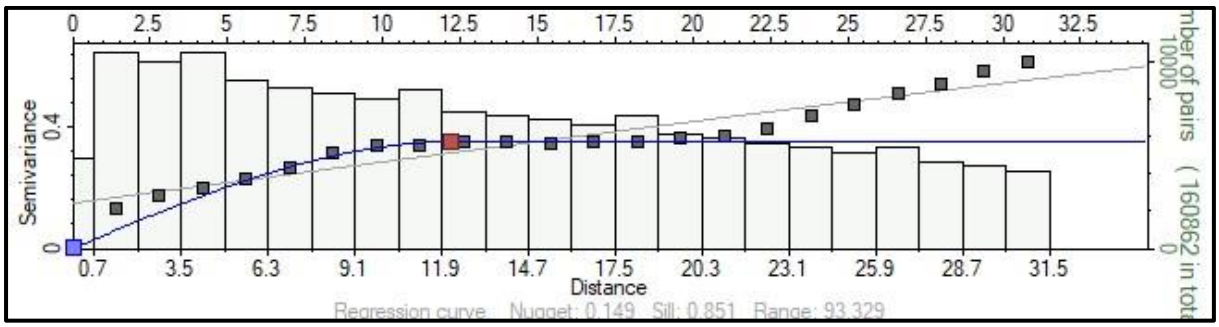

Figure 5.8: The vertical variogram for property modelling. The blue line represents the variogram model whereas the points are the averaged semivariance of the data pairs. The red point indicated the variogram range.

5.7. Fault seal analysis

5.7.1. Allan diagram

Two Allan diagrams were built in both models. The first Allan diagram was based on the zones defined by the modelled seismic depth surfaces and the second Allan diagram was based on the facies log. The facies were assigned to each zone based on the interpretation of the gamma ray log (**Section 5.1**).

5.7.2. Shale smear

Shale smears were analysed in one of the major faults (area B in **Figure 5.4**). The high-resolution data allow to map the shale smeared into the fault zone. Due to the high lateral variability of the smeared shale, it was tracked on each x-line of the high-resolution data.

5.7.3. Shale gouge ratio

The Shale gouge ratio (SGR) was calculated for all faults but analysed in just one of the major faults (area B in **Figure 5.4**). This SGR is based on the modelled distribution of volume of shale (Vsh). In this study, the SGR was calculated as an average value with shale contributions from both the footwall and the hanging-wall.

5.8. Gross rock volume estimation

The gross rock volume of the Stø reservoir was estimated in both models. Differences in the gross volume of the reservoir have a major impact on the hydrocarbon volume and therefore are important to capture.

6. Results

6.1. Data characterization

6.1.1. Well interpretation

Figure 6.1 shows the well 7324/8-3 with the gamma ray, resistivity, neutron, density, sonic, and acoustic impedance logs alongside. A fining upwards and two coarsening upwards intervals are identified. The first coarsening upward interval is observed from the Fruholmen to the Stø Fm. In this interval, shale and sandstone in the Fruholmen Fm gradually changes to more homogenous sandstone in the Stø Fm. This is indicated by the gamma-ray values, which are high in the Fruholmen Fm (>90gAPI) and low in the Stø Fm (<50gAPI). This also marks a change of depositional environment from fluvio-deltaic (Fruholmen Fm) to shoreface (Stø Fm).

The next succession has a fining upwards trend. This interval is characterized by an abrupt change from sandstone (Stø Fm) to shale (Fuglen and Hekkingen Fms). The change from sandstone to shale is related to a rifting event that occurred during the deposition of the Fuglen and Hekkingen Fms. A gradually coarsening upwards trend is observed from the Klippfisk Fm to the Nordland Group. This interval is characterized by decreasing gamma ray values towards the Nordland Group, indicating more sandstone.

The main reservoirs in well 7324/8-3 are the Stø Fm and the Fruholmen Fm. The Stø Fm is characterized by sandstone with high resistivity values indicating hydrocarbon accumulation. The crossover zone of the neutron and density logs confirms the sandstone zone. Furthermore, the Fruholmen Fm also shows high resistivity indicating the accumulation of hydrocarbons. The thick shale zones of the Fuglen Fm (38m) and the Hekkingen Fm (30m) overly the Stø Fm and act as top seals.

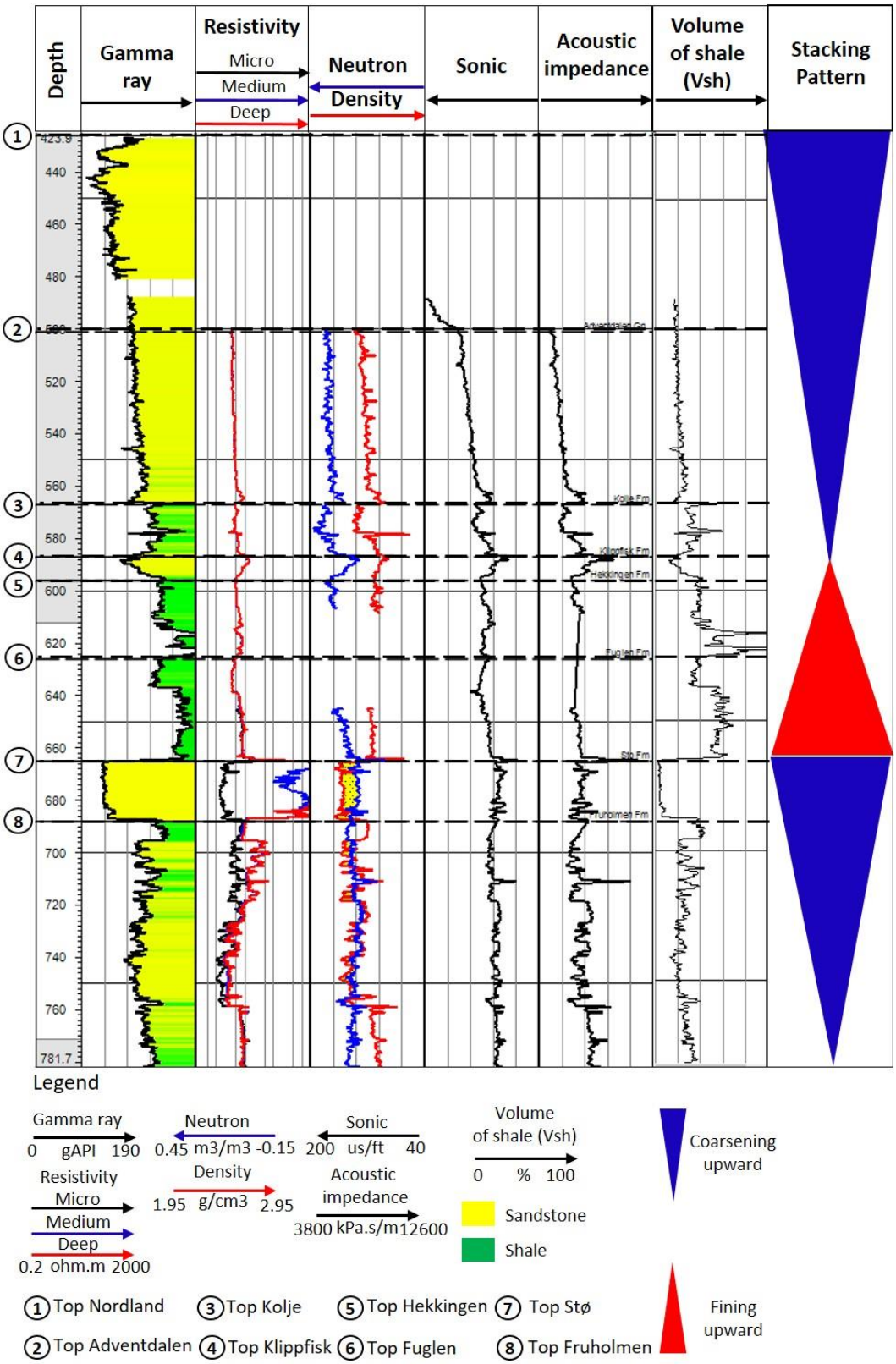

Figure 6.1: Well 7324/8-3 with gamma-ray, resistivity, neutron, density, sonic and acoustic impedance logs, and the stacking pattern. The main reservoir is in the Stø Fm between tops 7 and 8. Note that in this interval, the resistivity logs show high value, indicating a hydrocarbon accumulation. Cross-over of the neutron-density logs marked by the stippled yellow colour indicates the sand zone. Two coarsening upward and one fining upward interval are observed. The fining upward interval corresponds to the shale rich Fuglen and Hekkingen Fms. See well location in Figure 5.4

6.1.2. Seismic-well tie

The seismic-well tie highlights the importance of seismic resolution when comparing the P-cable data and the conventional data. Vertical resolution, in general, is slightly less than the tuning thickness. The tuning thickness is defined as one quarter of the wavelength, which corresponds to the lateral resolution (Simm and Bacon, 2014). The wavelength is calculated by dividing the seismic velocity by the seismic frequency. The high frequencies of the low-resolution (10-70Hz) and high-resolution (7-185Hz) are critical in determining the vertical and the lateral resolution. With increasing frequency, the wavelength decreases. As a result, the resolution is getting higher.

For a velocity of 2000m/s, the seismic resolution of the P-cable data can be as high as about 3m, whereas it is about 7m in the conventional seismic data. In addition, **Figure 5.2** shows the importance of the wavelet in the two seismic datasets. In the conventional data (low-resolution), the wavelet is characterized by large side lobes compared to the P-cable (high-resolution) data. The smaller size of the side lobes in the P-cable data increases the resolution.

Due to this property, the P-cable or high-resolution seismic gives additional information on the horizon recognition. The main reservoirs (Stø and Fruholmen Fms) are represented in a more detailed way. The high-resolution seismic can image the heterogeneity of the Stø Fm, and the thin layered channelized sandstone of the Fruholmen Fm. For instance, with a thickness of 20m, the Stø Fm is characterized by five reflectors in the high-resolution seismic. However, in the low-resolution seismic, the Stø Fm is only characterized by two reflectors (a trough and a peak) (**Figure 5.3**).

Figure 5.3 shows a small seismic section and the synthetic from the conventional (low-resolution) seismic and the P-cable (high-resolution) seismic. In the Adventdalen Gp (between horizons 1 and 2), the reflectors show a more consistent structure and continuity in the high-resolution seismic, whereas in the low-resolution seismic, the structure is more distorted. It is worth noting that a low angle horizon is visible in the high-resolution seismic in the upper part of this interval, but it is fragmented in the low-resolution seismic at the same level. The Kolje Fm (between horizons 2 and 3) and Fuglen Fm (between horizons 3 and 4) have more reflectors in the high-resolution seismic (10 and 9 reflectors) than in the low-resolution seismic (6 and 4 reflectors). The Fruholmen Fm (below horizon 5) shows 7 reflectors in the high-resolution seismic, and only 3 reflectors in the low-resolution seismic. To summarize, the P-cable seismic

has more seismic traces than the conventional data and follows more closely the acoustic impedance log.

6.1.3. Variance attribute

As discussed in section **5.3**, the variance attribute is used to guide the fault interpretation. In this chapter, the variance attribute (**Figure 6.2**) as well as seismic sections (**Figure 6.3**) from both datasets are compared.

Figure 6.2a (right) shows the zoomed time slice of the variance attribute (-770ms) from the low-resolution seismic. This time slice is at the Stø reservoir level. In **Figure 6.2a** (right), the NNE-SSW fault near the eastern boundary is displayed as low variance. This inability to capture the faults impacts the geomodel building as discussed in sections **6.3.1** and **6.3.2. Figure 6.2b** (right) displays the same area of the variance time slice (-770ms) from the high-resolution seismic. The WNW-ESE and NNE-SSW faults are sharper, and they are clearly indicated by high variance (black and red) values.

Figure 6.3 shows the seismic section along the navigation line A-B in **Figure 6.2**. **Figure 6.3a-b** are the uninterpreted and interpreted section of the low-resolution data. Four horizons corresponding to the top Kolje, top Fuglen, top Stø, and top Fruholmen are interpreted. A fault is not observed in this section. All mapped horizons are horizontal in the west and central part of the section, and they are folded in the eastern area. **Figure 6.3c-d** are the uninterpreted and interpreted section of the high-resolution data. In **Figure 6.3d,** the top Kolje and top Fuglen are folded in the eastern part. However, unlike the low-resolution section, a fault that offsets the top Stø and top Fruholmen is observed.

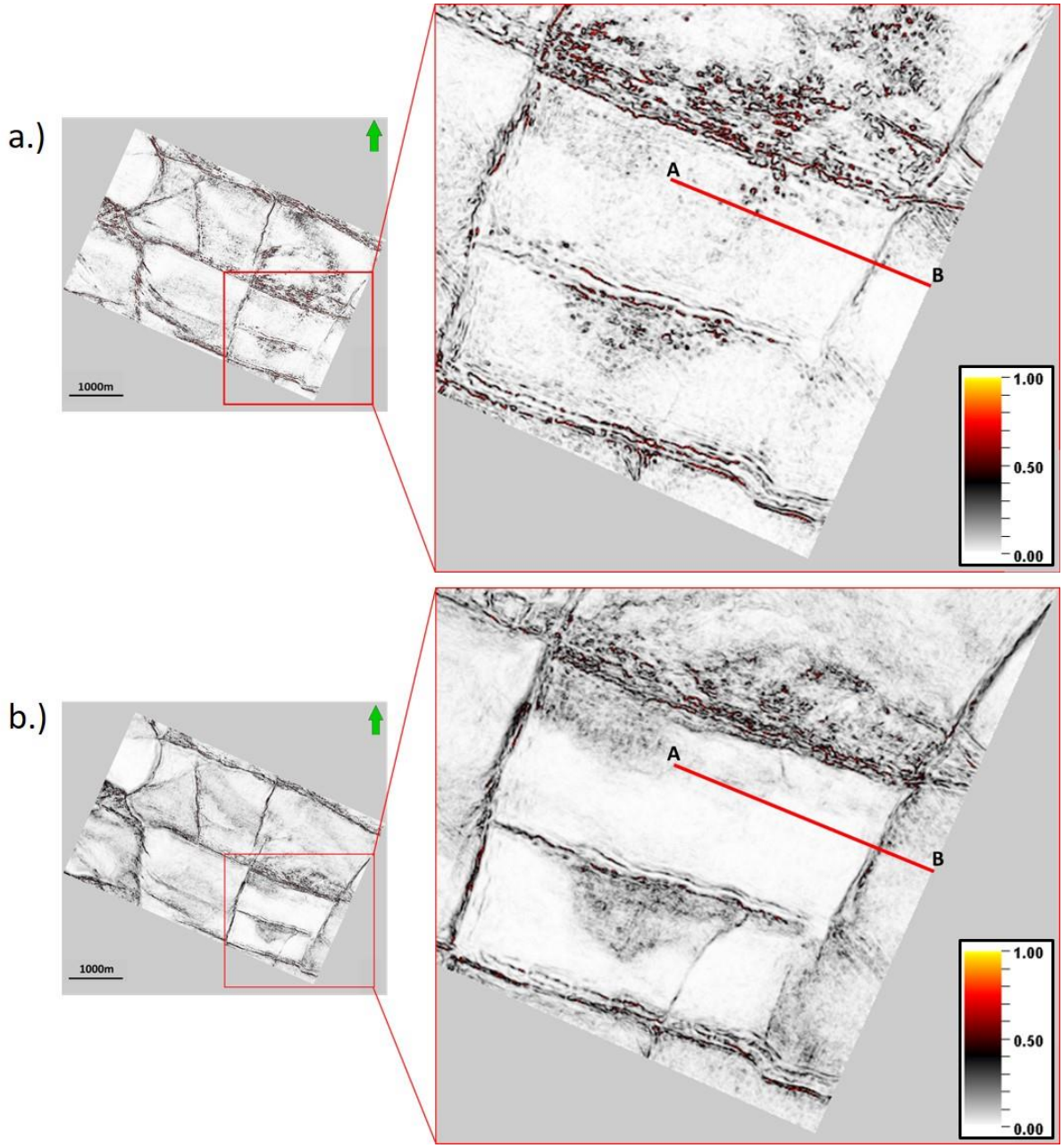

Figure 6.2: Variance attribute from the (a) low-resolution, and (b) high-resolution data. Both time slices are at -770ms (Stø Fm reservoir level). Note that the faults are sharper in the high-resolution seismic and are indicated by higher variance.

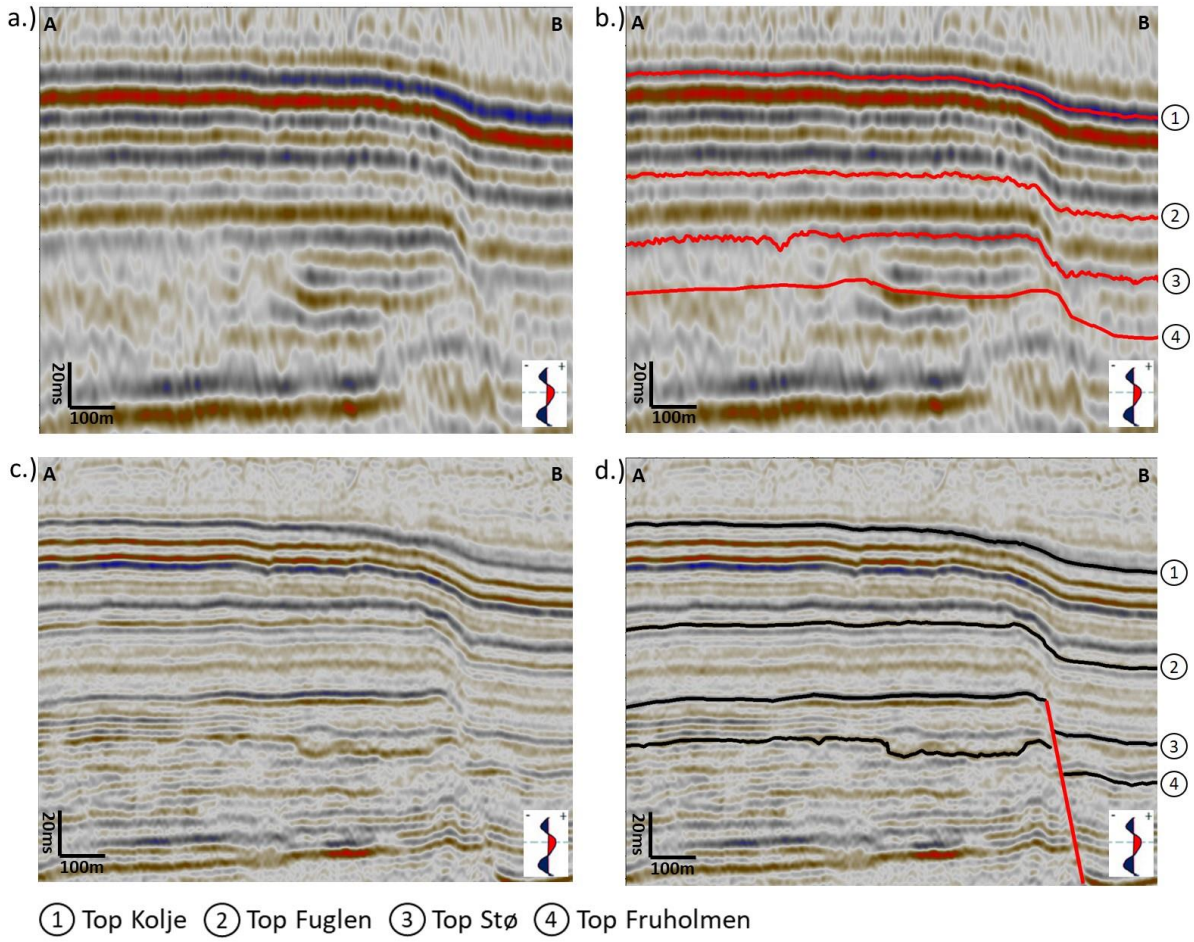

Figure 6.3: (a) Uninterpreted and (b) interpreted low-resolution seismic line. Note that all horizons are folded in the eastern part of the area. (c) Uninterpreted and (d) interpreted high-resolution seismic line. Top Kolje and top Fuglen are folded in the eastern part, while top Stø and top Fruholmen are faulted. See navigation line in Figure 6.2.

6.1.4. RMS amplitude attribute

The RMS amplitude is used to determine the area of hydrocarbon accumulation, which is the area modelled in this study. **Figure 6.4a** shows the RMS amplitude along the top of the Stø reservoir in the low-resolution seismic, while **Figure 6.4b** shows the RMS amplitude from the same surface in the high-resolution seismic. Both maps show high amplitude values (blue) in the vicinity of the WNW-ESE fault. This area corresponds to a hydrocarbon accumulation, as discussed in section **6.1.5**. However, in the high-resolution seismic (**Figure 6.4b**), the high RMS amplitude covers a larger area.

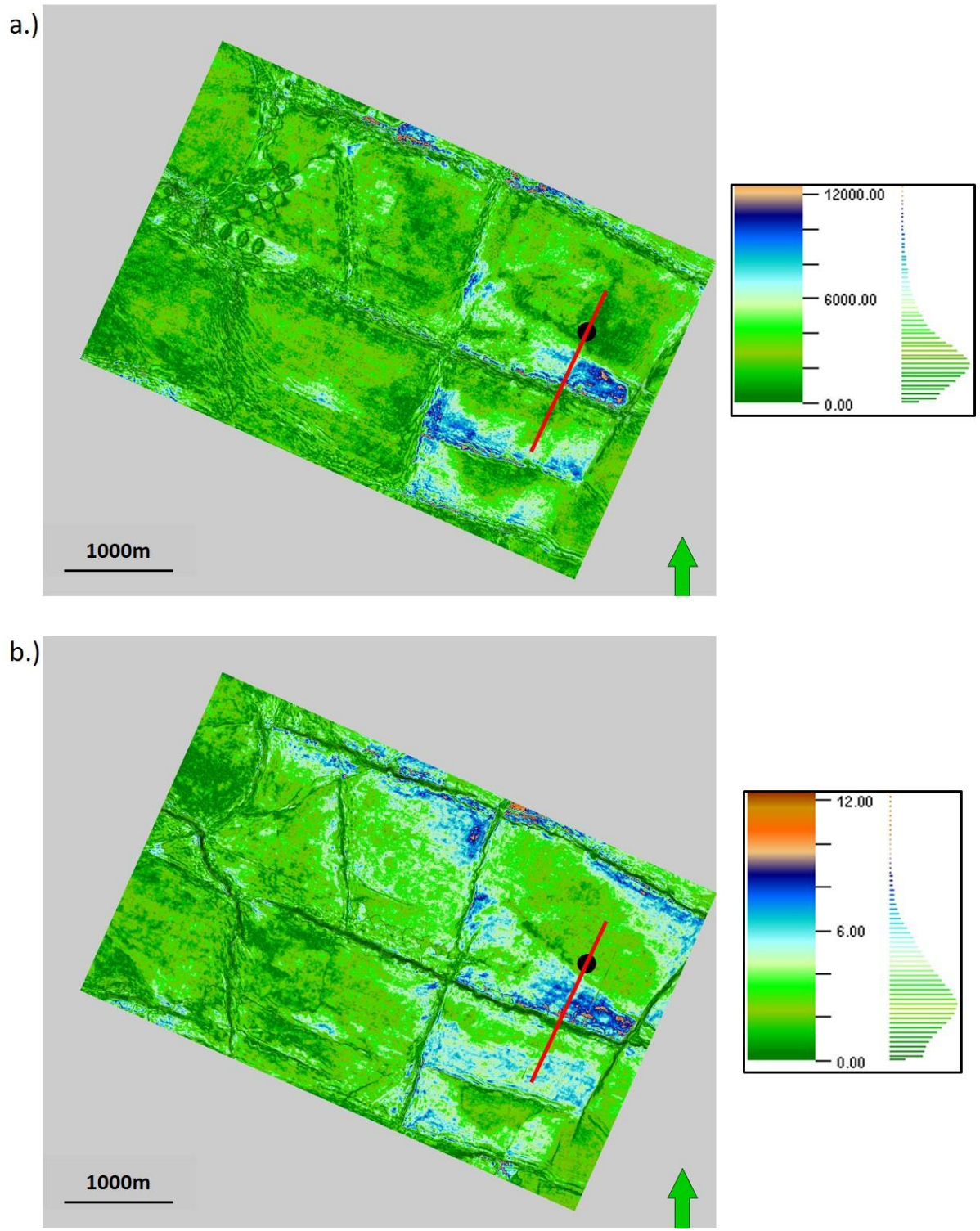

Figure 6.4: RMS amplitude extracted on the top Stø in the (a) low-resolution seismic, and (b) high-resolution seismic. From both figures, the high RMS amplitude values are in the vicinity of the WNW-ESE fault. However, in the high-resolution seismic, the high RMS amplitudes cover a larger area.

6.1.5. Flat spot

A flat spot is recognized updip of the well 7324/8-3. The presence of this fluid contact indicates a hydrocarbon accumulation. **Figure 6.5** shows the image of the flat-spot in the low- and high-resolution seismic. **Figure 6.5a** displays the low-resolution seismic section and well 7324/8-3 with the gamma ray log and well tops. The Stø Fm sandstone reservoir is shown by the yellow interval in the log. This reservoir is characterized in the seismic by a trough at the top and a peak at the bottom. Towards the fault, no horizontal reflector (flat spot) cutting the strata is observed. However, in **Figure 6.5b**, which shows the same section in the high-resolution seismic, a horizontal reflector (flat spot) cutting the strata and terminating against the fault is observed at the Stø reservoir level. With the information from well 7324/8-3 that indicates an oil column in the Stø reservoir (high resistivity in **Figure 6.1**), the flat spot, which is updip of the well, should correspond to the gas-oil contact. This gas accumulates at the highest elevation of the tilted fault block and is laterally sealed by the normal fault to the southwest.

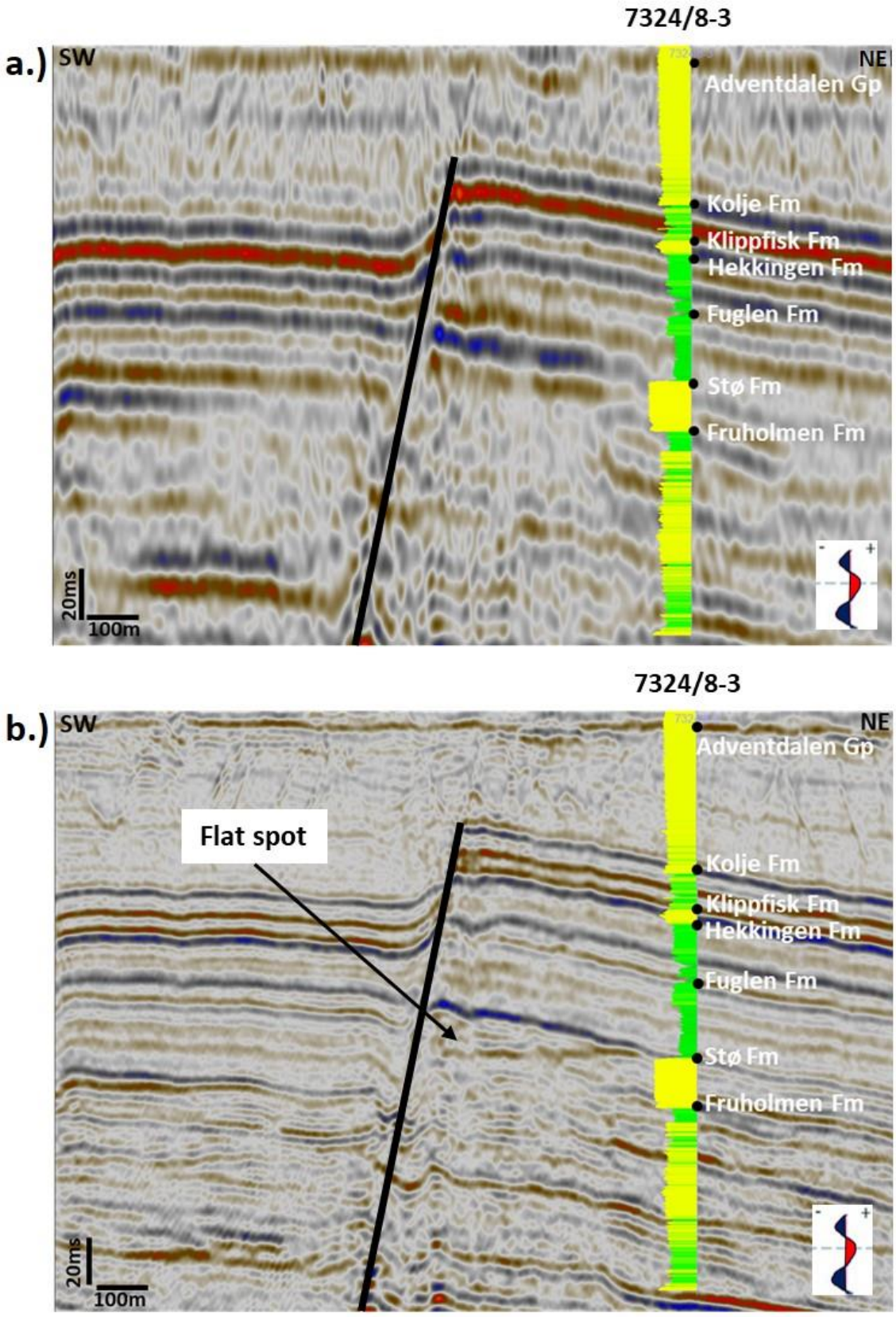

Figure 6.5: (a) Low-resolution, and (b) high-resolution seismic section. Both sections show well 7324/8-3 with gamma ray log and well-tops. Yellow in the gamma-ray is sandstone while the green is shale. The flat spot is displayed only in the high-resolution seismic. It is in the Stø Fm, updip of the fault and terminates against the fault. See navigation line in Figure 6.4.

6.2. Horizons' uncertainties and isochore maps

6.2.1. Horizons' uncertainties

As mentioned in section **5.4**, the differences of the interpreted horizons between the low- and high-resolution seismic is regarded as the horizons' uncertainties. **Figure 6.6** shows a section from the high-resolution seismic alongside with the well 7324/8-3. The high resolution surfaces top Kolje, top Fuglen, top Stø, and top Fruholmen are shown in black, whereas the same interpreted surfaces from the low-resolution seismic are displayed in red. The top Kolje and top Fuglen show small differences as illustrated by the histograms in **Figure 6.7**. The standard deviation of the differences between the low- and high resolution top Kølje is 0.65ms, whereas for the top Fuglen, it is 1.19ms (**Figure 6.7**). The highest differences in the top Fuglen are in the southwest of the well.

The high-resolution top Stø and top Fruholmen honour their well tops. In contrast, the same surfaces interpreted from the low-resolution seismic do not honour the well-tops, or the high-resolution seismic reflectors (**Figure 6.6**). As mentioned in section **6.1.2**, the sandstone zone of the Stø Fm is not well defined by the low resolution seismic. The standard deviation of the top Stø between the low- and high resolution seismic is 3.24ms, while that of the top Fruholmen is 2.98ms (**Figure 6.7**). Thus, surfaces from the low-resolution seismic become more irregular and their uncertainties increase with depth.

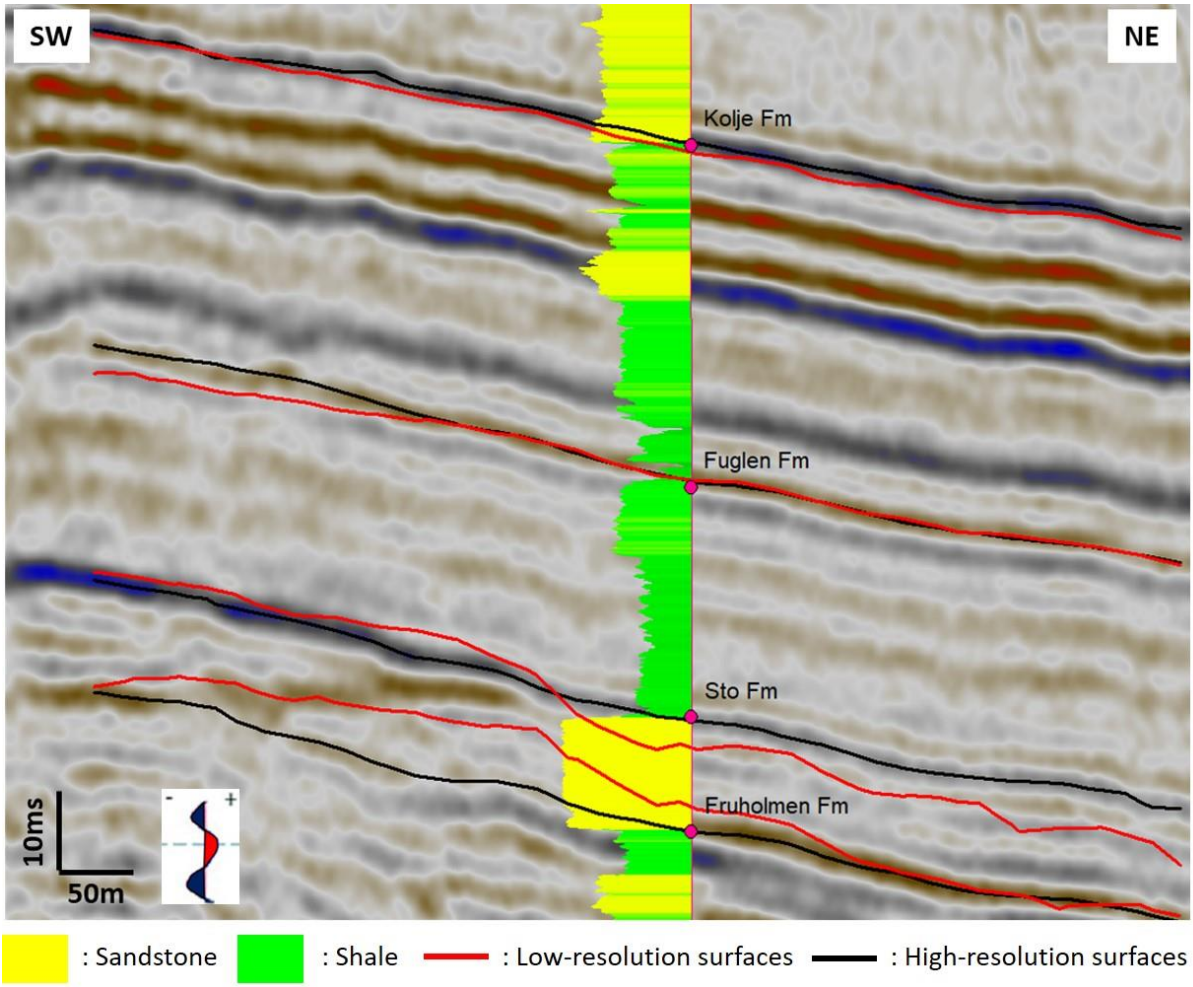

Figure 6.6: Horizons' uncertainties. Red lines correspond to the low-resolution surfaces while black lines are the high-resolution surfaces. Both surfaces are displayed on the high-resolution seismic. Low-resolution top Stø and top Fruholmen do not honour their well-tops and the seismic reflectors. Surfaces from the low-resolution seismic become more irregular with depth. The navigation line is given in line C of Figure 5.4.

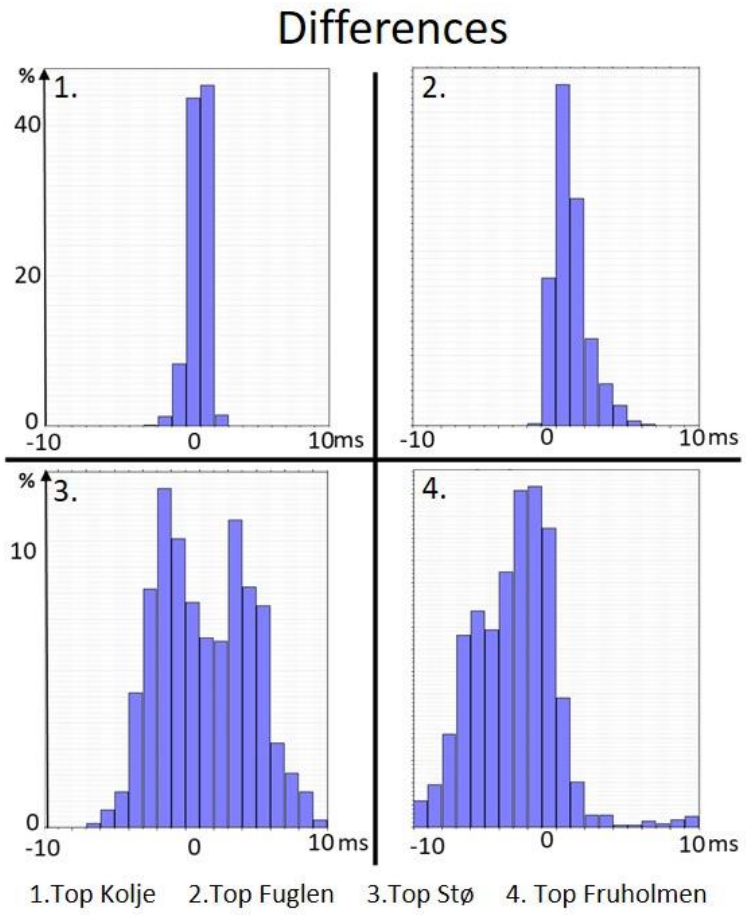

	Top Kolje	Top Fuglen	Top Stø	Top Fruholmen
Standard Deviation (ms)	0.65	1.19	3.24	2.98

Figure 6.7: Differences between horizons interpreted in the low- and high-resolution seismic. Note that the standard deviation increases with the horizon depth.

6.2.2. Isochore map

Isochore (vertical thickness) maps were generated from the interpretation of the low- and high-resolution data. Here we only show the isochore of the Stø Fm. **Figure 6.8** clearly demonstrates the difference between the high-resolution (HR) and the low-resolution (LR) isochore map. **Figure 6.8a** shows small thickness variation of the Stø Fm from the-high resolution data. The average thickness of the Stø Fm is 18-22ms. However, around the faults, the thickness varies. This is due to folding and steepening of the horizons towards the faults, which results in more vertical thickness. **Figure 6.8a** clearly indicates the faults by low (<5ms) thickness of the Stø Fm. In contrast, **Figure 6.8b** from the low-resolution data displays a less-fault controlled thickness variation of the Stø Fm. In the northeast, the thickness varies from 5-15ms, while in the southwest, the Stø Fm thickness increases up to 20-30ms. No clear sign of the faults as well as inconsistency of thickness variation confirm the unreliability of the low-resolution (LR) isochore map.

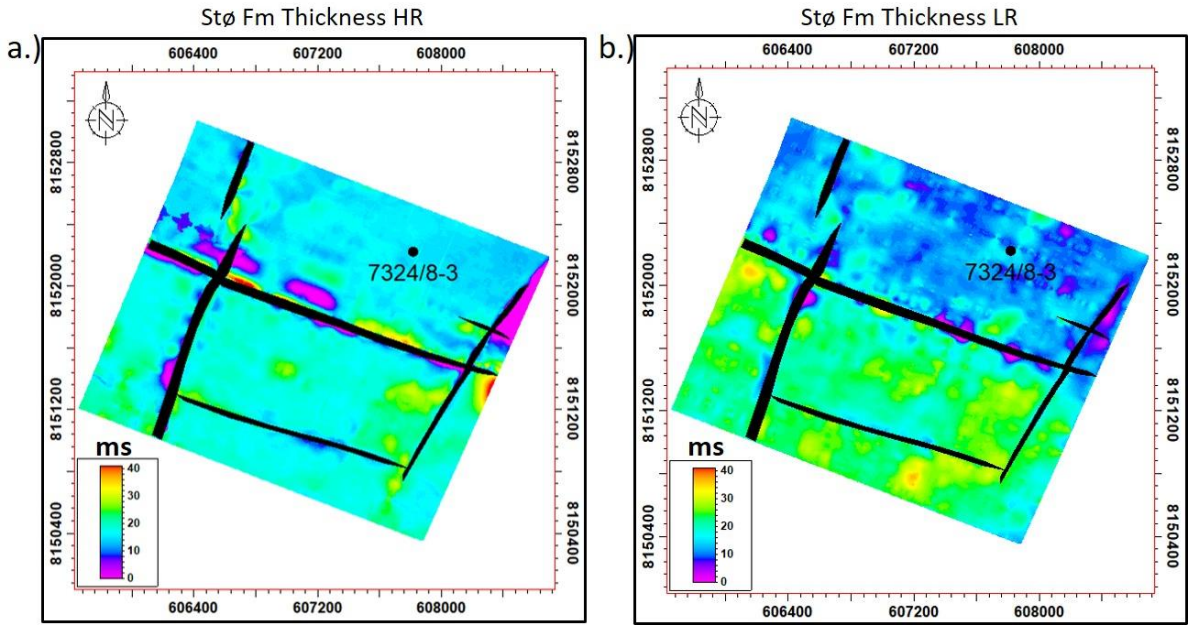

Figure 6.8: Stø Fm isochore map based on the (a) high-resolution (HR) and (b) low-resolution (LR) data. The Stø Fm vertical thickness is more consistent in the high-resolution variation. Black lines indicate the fault zones. The isochore maps cover the area A in Figure 5.4.

6.3. Geomodel building

6.3.1. Fault network

Here we compare the quality and consistency of the fault network between the low- and high-resolution seismic. **Figure 6.9** shows the fault network from both datasets. The study area is divided into fault compartments. **Figure 6.9a** shows the fault network from the low-resolution model, while **Figure 6.9b** shows the fault network from the high-resolution model. In both models, the WNW-ESE grey-purple fault is offset by the NNE-SSW blue-green fault. The main difference between the two models is the number of faults. The NNE-SSW pink-red fault is visible in the high-resolution data, but it cannot be observed in the low-resolution data (**Figure 6.2a-b, Figure 6.3b, Figure 6.3d**). This fault is offset by the WNW-ESE grey-purple fault (**Figure 6.9b**). The branch lines of the different fault intersections can be seen in **Figure 6.10**.

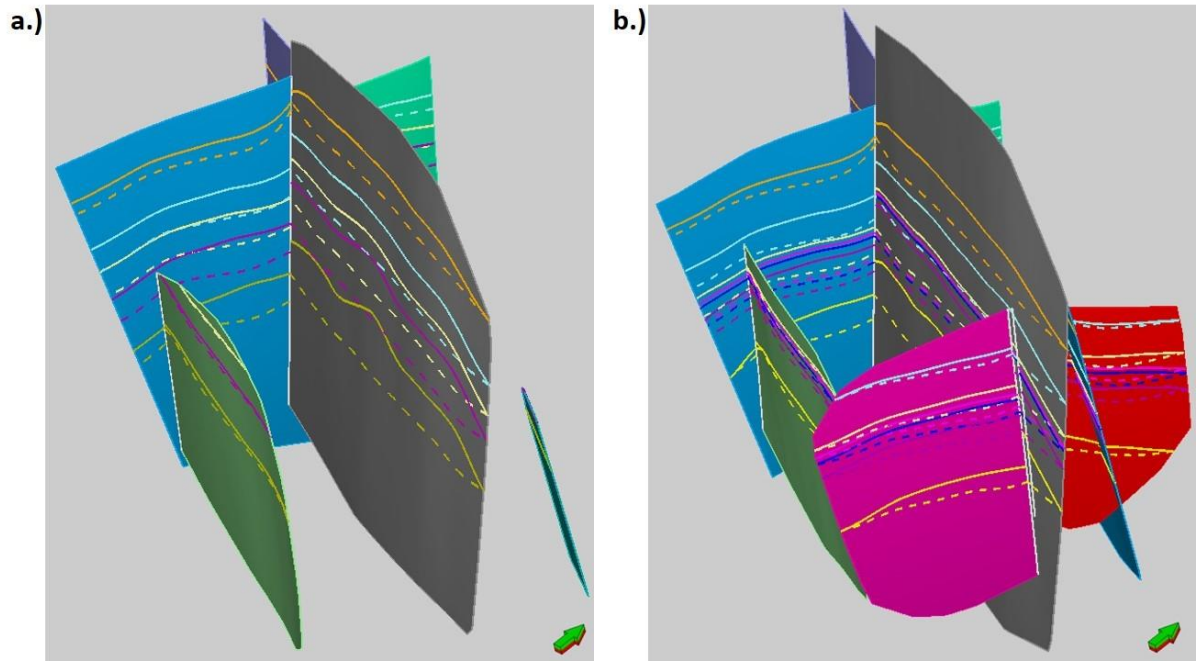

Figure 6.9: Fault network from (a) low-resolution and (b) high-resolution model. The continuous lines are the footwall cutoffs while the dashed lines are the hanging wall cutoffs. Note that the pink-red fault is not present in the low-resolution model. The model covers area A of Figure 5.4.

6.3.2. Fault cutoffs

Fault cutoffs are the intersections of the modelled horizons with the fault planes. **Figure 6.10** illustrates the fault cutoffs from both models. **Figure 6.10a** shows the cutoffs from the low-resolution model. The cutoffs gradually get more irregular with increasing depth. **Figure 6.10b** shows the cutoffs from the high-resolution model. In contrast to the low-resolution

model, the cutoffs in the high-resolution model are more consistent. Moreover, two additional cutoffs can be determined within the Stø reservoir. These are observed between cutoffs 3 and 4 (**Figure 6.10b**). As mentioned before, the grey-purple fault is offset by the NNE-SSW fault in the western part of the area. This intersection is represented by the white branch line that separates the grey and the purple fault segments. To the east, two white branch lines are observed. These branch lines represent the intersections with the NNE-SSW pink-red fault, which is offset by the grey fault. These observations suggest that the WNW-ESE and NNE-SSW faults were formed simultaneously (Collanega et al., 2017).

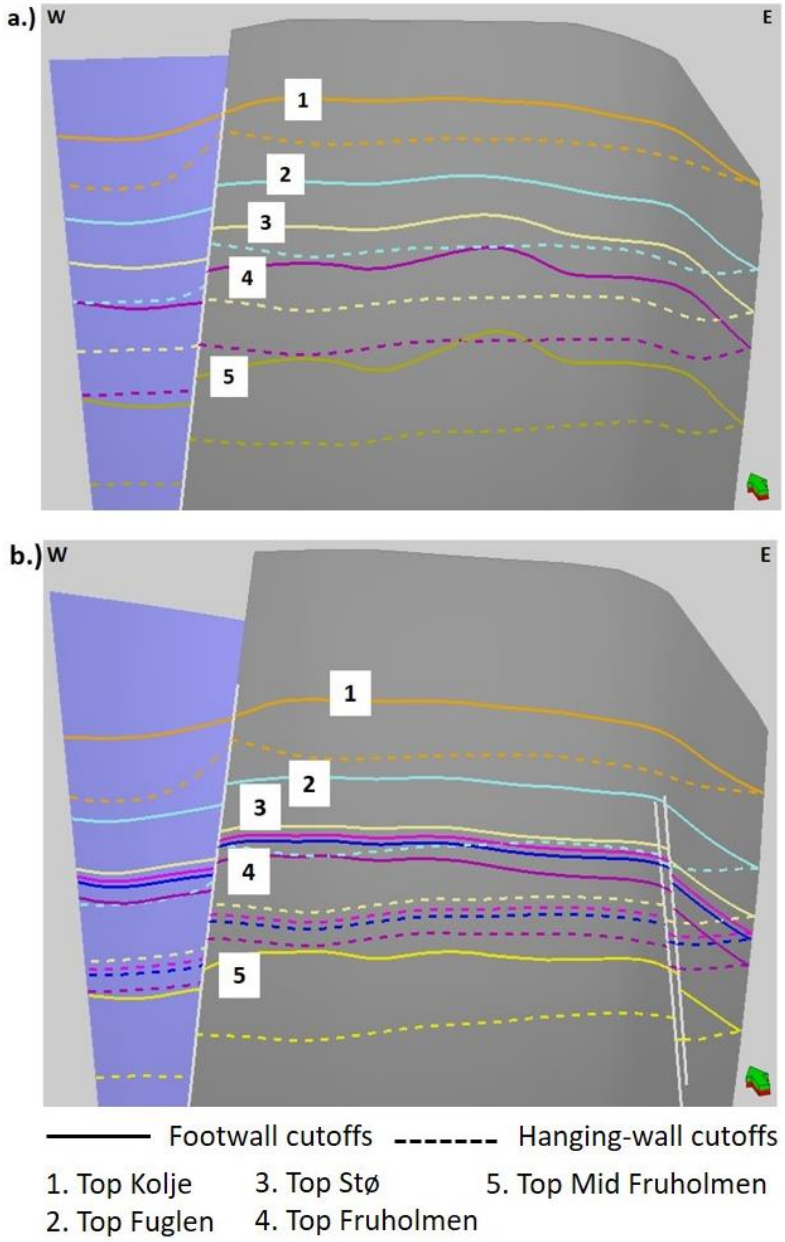

Figure 6.10: WNW-ESE fault plane with cutoffs from (a) the low-resolution and (b) the high-resolution model. Cutoffs in the low-resolution model are more irregular with depth. See area B in Figure 5.4 for the location of the faults.

6.3.3. Fault throw

The fault throw is the vertical component of the dip displacement between the footwall and hanging wall. In this section, the fault throw from the low-resolution model is compared to the high-resolution model. **Figure 6.11a** shows the throw distribution from the low-resolution model. A small throw (0-10m) is observed at the eastern fault tip line. The fault throw gradually increases to the west. Two fault throw maxima (60-70m) indicated by yellow and red colours are observed on the central part of the fault. **Figure 6.11b** shows the throw distribution from the high-resolution model. The lowest fault throw (0-10m) is also observed at the eastern fault tipline, and gradually the throw increases to the west. However, in the high-resolution model, only one fault throw maximum (60-70m) can be observed on the central part of the fault. Therefore, this model has a more consistent fault throw distribution. Fault segment 2 shows also a large throw, since segments 1 and 2 are part of the same fault. The large throw is also caused by the NNE-SSW intersecting fault (blue-green) in **Figure 6.9**.

The fault throw distribution in each model can be visualized by throw profiles. As seen in **Figure 6.11c**, the throw profile of the low-resolution model shows large undulations. For instance, horizons 2-5 show two throw maxima and one throw minimum. Moreover, horizons 3, 4 and 5 overlap on the central part of the fault. This indicates large vertical variations of the throw which is not realistic. **Figure 6.11d** shows the throw profile from the high-resolution model. The high-resolution model has a smoother fault throw distribution. There is just one throw maximum on the western part of the fault, and the displacement gradually decreases to the east. Also, the horizons' throw profiles do not overlap. Two additional (green and yellow) horizons can be observed in the figure. These are located in the Stø Fm between horizons 3 and 4.

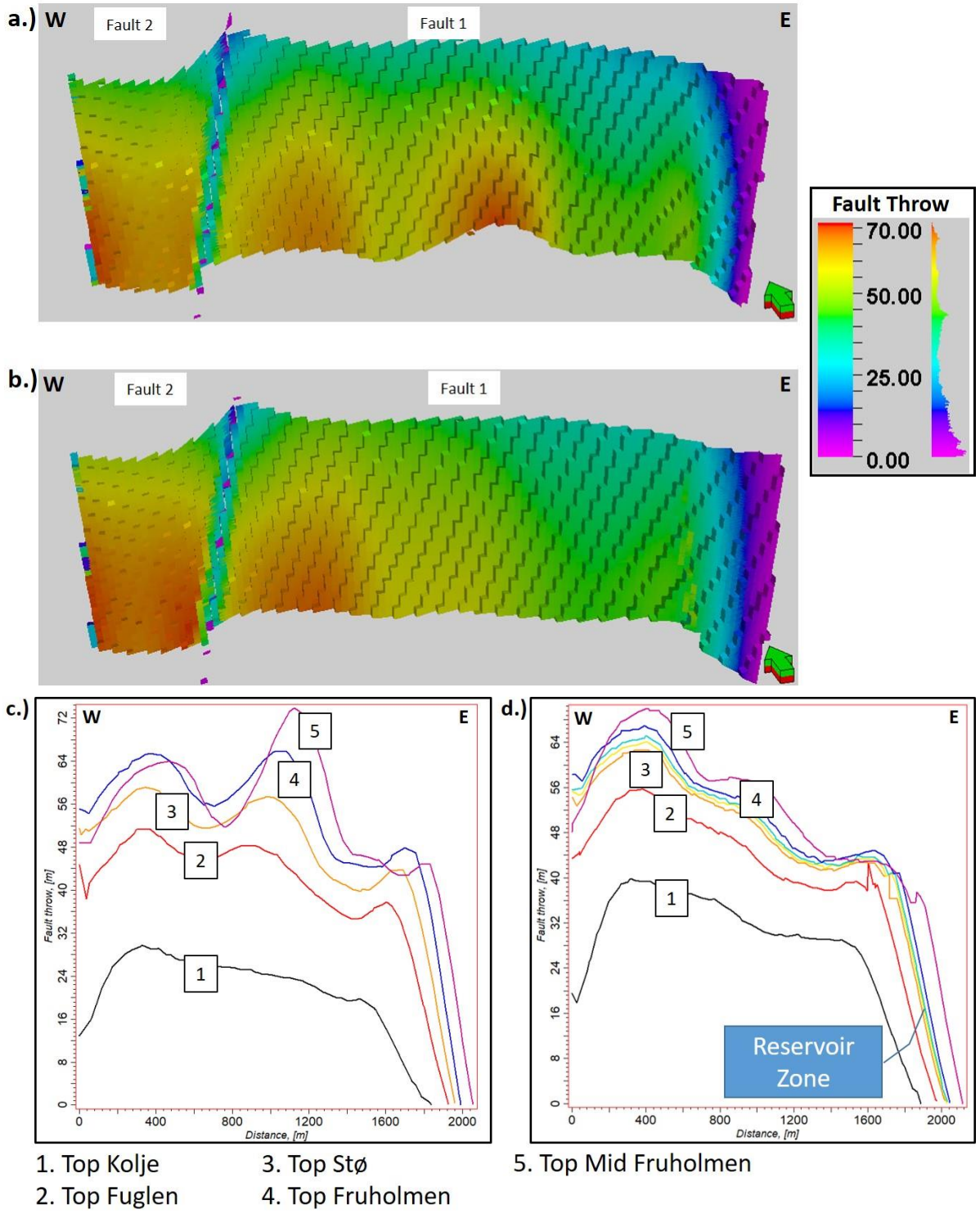

Figure 6.11: Fault throw from (a) low-resolution and (b) high-resolution model. Throw profiles from (c) low-resolution and (d) high-resolution model. Fault throw from high-resolution model is more consistent. See area B in Figure 5.4 for the location of the profile.

6.4. Fault seal analysis

6.4.1. Allan diagram (zones)

The Allan diagram displays the stratigraphy from the hanging wall and the footwall that is superimposed along the fault plane. The Allan diagram will be discussed mainly to explain and compare the juxtaposition of the Stø Fm against the Kolje, Fuglen, Stø itself, and Fruholmen Fm in both models (**Figure 6.12**). Each colour in the diagram represents the juxtaposition of the same formation or two different formations. Understanding the colour legend is critical for determining the juxtaposition relationships. As an example, the colour legend from the low-resolution model (**Figure 6.12a**) will be discussed briefly. A number is assigned to each zone. For instance, the Stø Fm zone is labelled by number 3, while the Kolje, Fuglen, and Fruholment Fms are labelled by numbers 1, 2, and 4, respectively. At location (1, 3), illustrated by the yellow colour, the Stø Fm is juxtaposed against the Kolje Fm. At location (2, 3), shown by light green colour, the Stø Fm is juxtaposed against the Fuglen Fm. Finally, at location (3, 3), marked with light blue colour, the Stø Fm is juxtaposed against itself.

In Figure **6.12**, four symbols are used for labelling the juxtaposition of the Stø Fm against itself and the other formations. A red circle marks the juxtaposition of the Stø Fm against the Kolje Fm. In the low-resolution model, this juxtaposition can be observed continuously from west to east (**Figure 6.12a**). However, in the high-resolution model, the juxtaposition of the Stø Fm against the Kolje Fm is divided into three colours (black, grey, and white) (**Figure 6.12b**). These colours represent the inner units of the Stø reservoir. To the east, only the upper part of the Stø reservoir is juxtaposed against the Kolje Fm. However, to the west, the entire Stø reservoir is juxtaposed against the Kolje Fm, indicating an increase of fault throw (**Figures 6.12b, 6.11d**).

A red star illustrates the juxtaposition of the Stø Fm against the Fuglen Fm. In the low-resolution model (**Figure 6.12a**), this juxtaposition can be observed along most of the fault, but it is not present in the central part of the fault. In contrast, in the high-resolution model (**Figure 6.12b**), the Stø Fm-Fuglen Fm juxtaposition is indicated by three different shades of brown colour reflecting the inner zones of the Stø Fm. This juxtaposition is mainly observed on the eastern part of the fault. In the central part of the fault, only the lower part of the Stø reservoir is juxtaposed against the Fuglen Fm, and this juxtaposition is not present to the west where the fault throw reaches its maximum (**Figures 6.12b 6.11d**).

The red triangle shows the juxtaposition of the Stø Fm against itself. In both the low- and high-resolution models (**Figure 6.12a** and **Figure 6.12b**), this juxtaposition shows a similar pattern, but it is more extensive in the high-resolution model (**Figure 6.12b**). This juxtaposition can only be observed on the eastern part of the fault where the fault throw is minimum (**Figures 6.12**, **6.11c-d**).

Finally, a red cross illustrates the juxtaposition of the Stø Fm against the Fruholmen Fm. In both models, this juxtaposition shows similar patterns along the fault (**Figure 6.12a-b**) However, in the high-resolution model, this juxtaposition shows three zones as result of the better definition of the inner structure of the Stø Fm (**Figure 6.12b**). To summarize, the high-resolution model provides more details in the juxtaposition relationships of the Stø Fm.

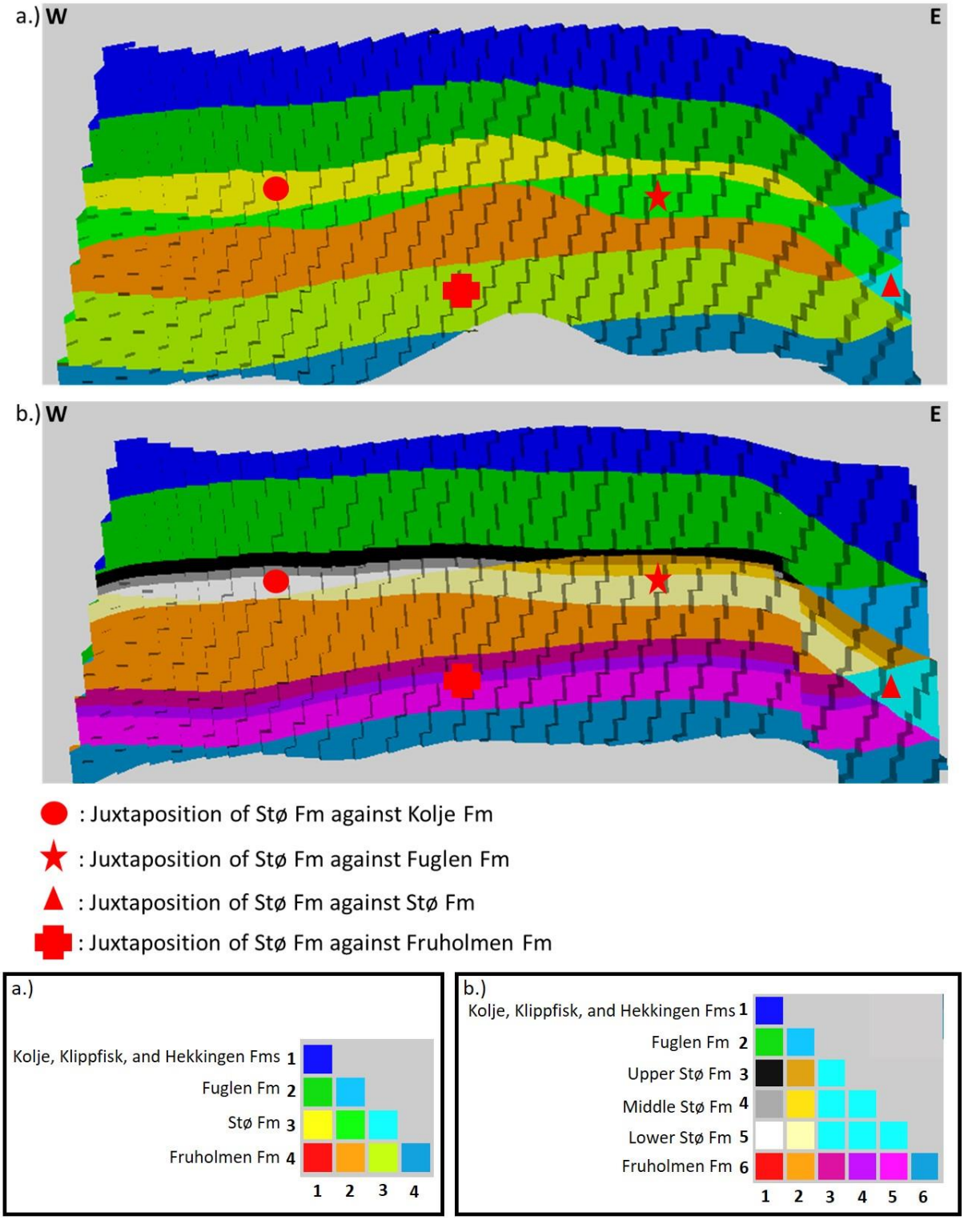

Figure 6.12: Allan diagram from the (a) low-resolution and (b) high-resolution model. The juxtaposition of Stø Fm against other formations are marked with different symbols. Note that in the high-resolution model, the Stø Fm is juxtaposed against itself to the east, against the Fuglen Fm in the central part of the fault, and fully juxtaposed against the Kolje Fm to the west. In the high-resolution model, the juxtaposition of the Stø and Fruholmen Fms can be divided into three separate zones. The Allan diagram from the low-resolution model cannot resolve these details. See area B in Figure 5.4 for the location of the analysis.

6.4.2. Allan diagram (facies)

In this section, we will focus on the Allan diagram that is produced by the facies model. **Figure 6.13** shows the Allan diagram (facies) of both seismic resolutions. In the low-resolution Allan diagram (**Figure 6.13a**), the sand-sand (red) and sand-shale (green) juxtapositions have an undulating shape. This results from the undulating fault cutoffs in **Figure 6.10a**. In the high-resolution model (**Figure 6.13b**), two inner zones of the Stø Fm are mapped, and the morphology of the juxtapositions is smoother and more consistent. In addition, the sand-sand juxtaposition in the lower part of the fault is more continuous and creates lenses. These red lenses mark the juxtaposition of sandstones of the Stø and Fruholmen Fms. On the eastern part of the fault, both models show self-juxtaposition of the Stø and Fruholmen sandstones. This corresponds with small fault throw (**Figure 6.11**).

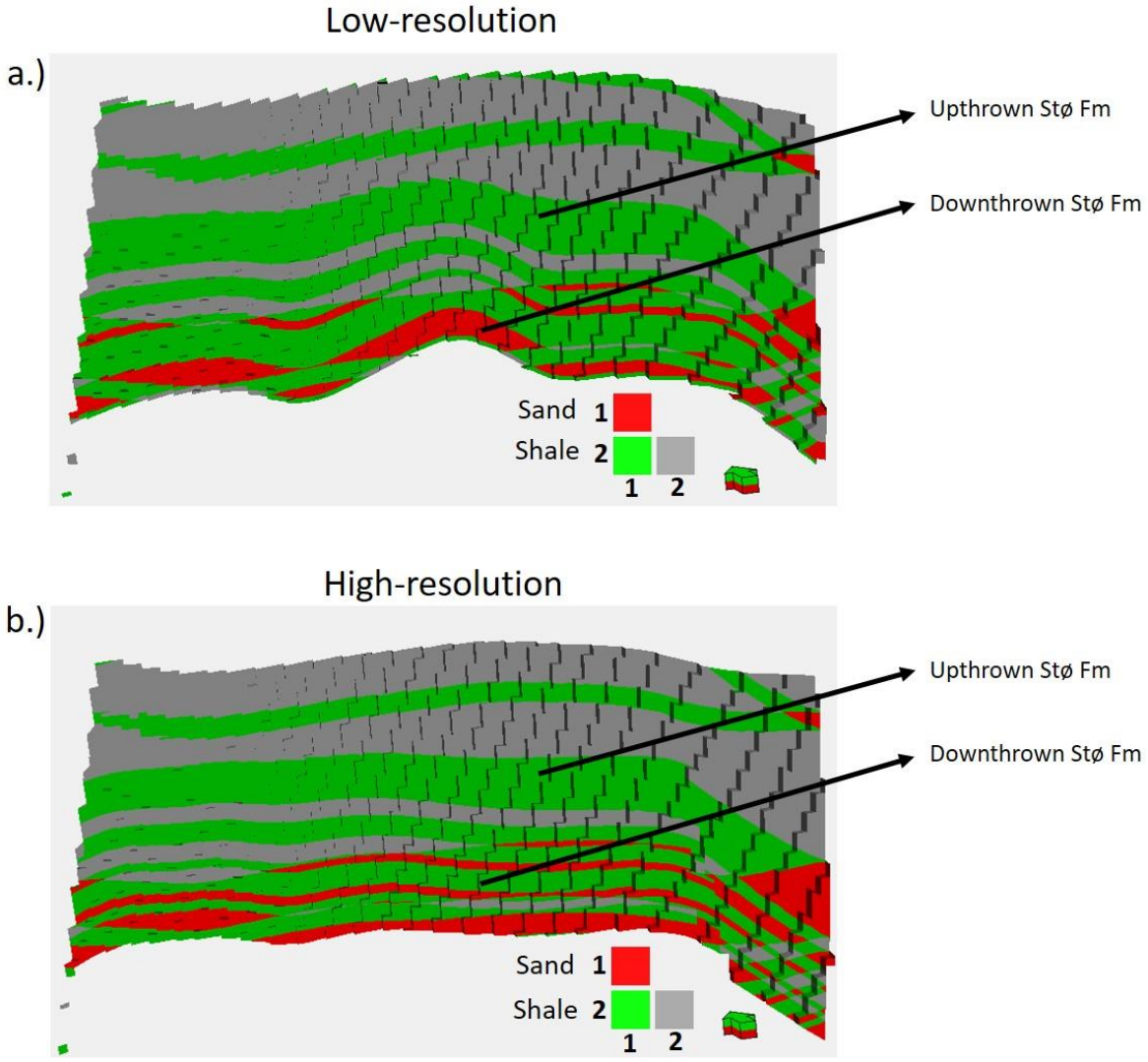

Figure 6.13: (a) Low-resolution and (b) high-resolution Allan diagram (facies). Note that in the low-resolution diagram, the juxtapositions undulate, while in the high-resolution diagram, the juxtaposition are more consistent

6.4.3. Shale smear

Shale smears occur when fine grained sediments rich in phyllosilicate minerals are dragged along the fault. The shale smear is only observed in the high-resolution seismic. In this section, the distribution of the shale smear along the WNW-ESE fault (grey fault in **Figure. 6.9**) will be described. The shale smear is derived from two different source beds, the Hekkingen and the Fuglen Fms. These formations are rich in shale and are prone to smear along the fault. To support this discussion, the fault throw and the Allan diagram (sections **6.3.3** and **6.4.1**) will be considered.

Figure **6.14** shows the location and the 3D view of the shale smear. The shale smear is not present everywhere. Its vertical continuity changes along the fault (**Figure 6.14b**). The continuity of the shale smear gradually increases from the east until it reaches a maximum in the central part of the fault. The shale smear is not developed in the western part of the fault. In some areas, the shale smear is only observed in the upper part and does not continue downwards. In other areas, it is present in the upper and lower parts, but is missing at central depths. This might indicate local changes of the lithology from the two different source formations. The shale content (Vsh) in Hekkingen Fm ranges from 33-100% while it is 29-65% in the Fuglen Fm (**Figure 6.1**).

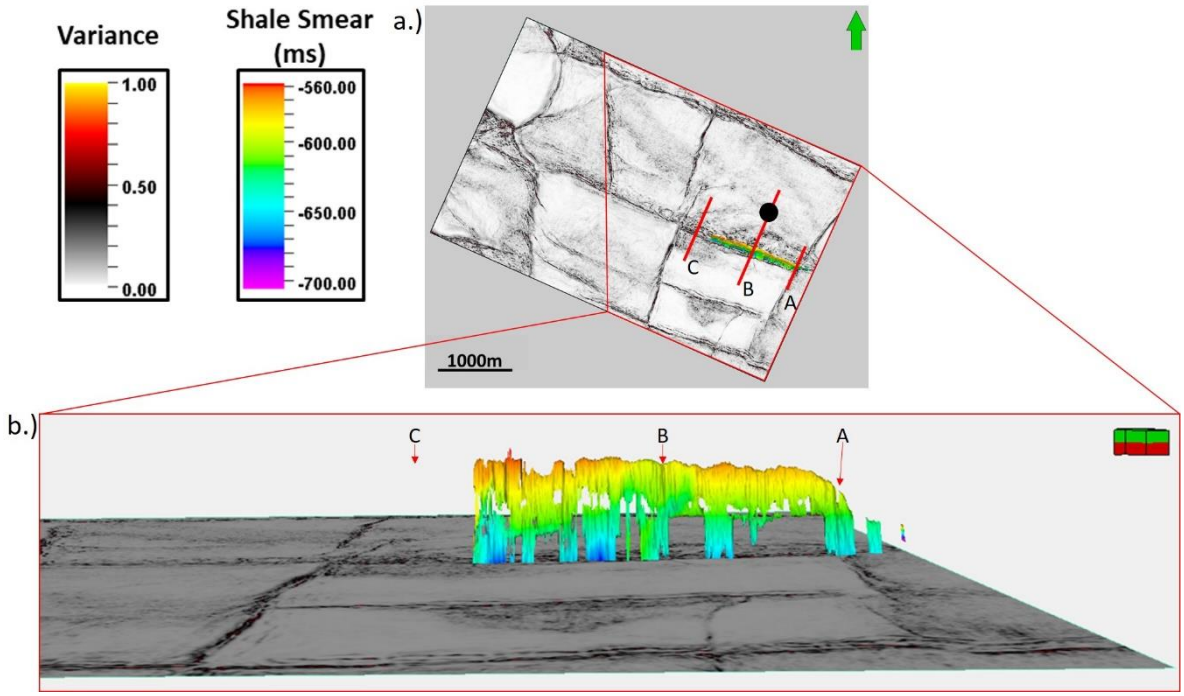

Figure 6.14: (a) Location of shale smear and (b) 3D distribution. The variance time slice is at reservoir level (-770ms). The shale smear gradually develops from the east (0-10m fault throw), reaching the maximum continuity in the central area (40-50m fault throw) and stops developing in the western area (60-70m fault throw).

Figure 6.15a shows the shale smear on the eastern part of the fault. The fault throw in this area is relatively small (0-10m), and hence, the Stø reservoir is juxtaposed against itself. The shale is smeared from two different source beds. The upper part corresponds to the Hekkingen Fm and the lower part to the Fuglen Fm. In this section, the shales from these two formations do not mix, but instead form two separate smears.

Figure 6.15b illustrates the shale smear on the centre of the fault. In this section, the fault throw is higher (40-50m) than in the eastern area. The higher fault throw impacts the juxtaposition of the Stø Fm. The Stø Fm is juxtaposed against the shale zone of the Fuglen Fm and the shale smear. The shale smears from the Hekkingen and Fuglen Fms are connected in the fault zone. This mixing of the source beds creates a more continuous smear. **Figure 6.15c** displays the western part of the fault. The fault throw reaches its maximum value (60-70m) and shale smear is no longer visible in this section.

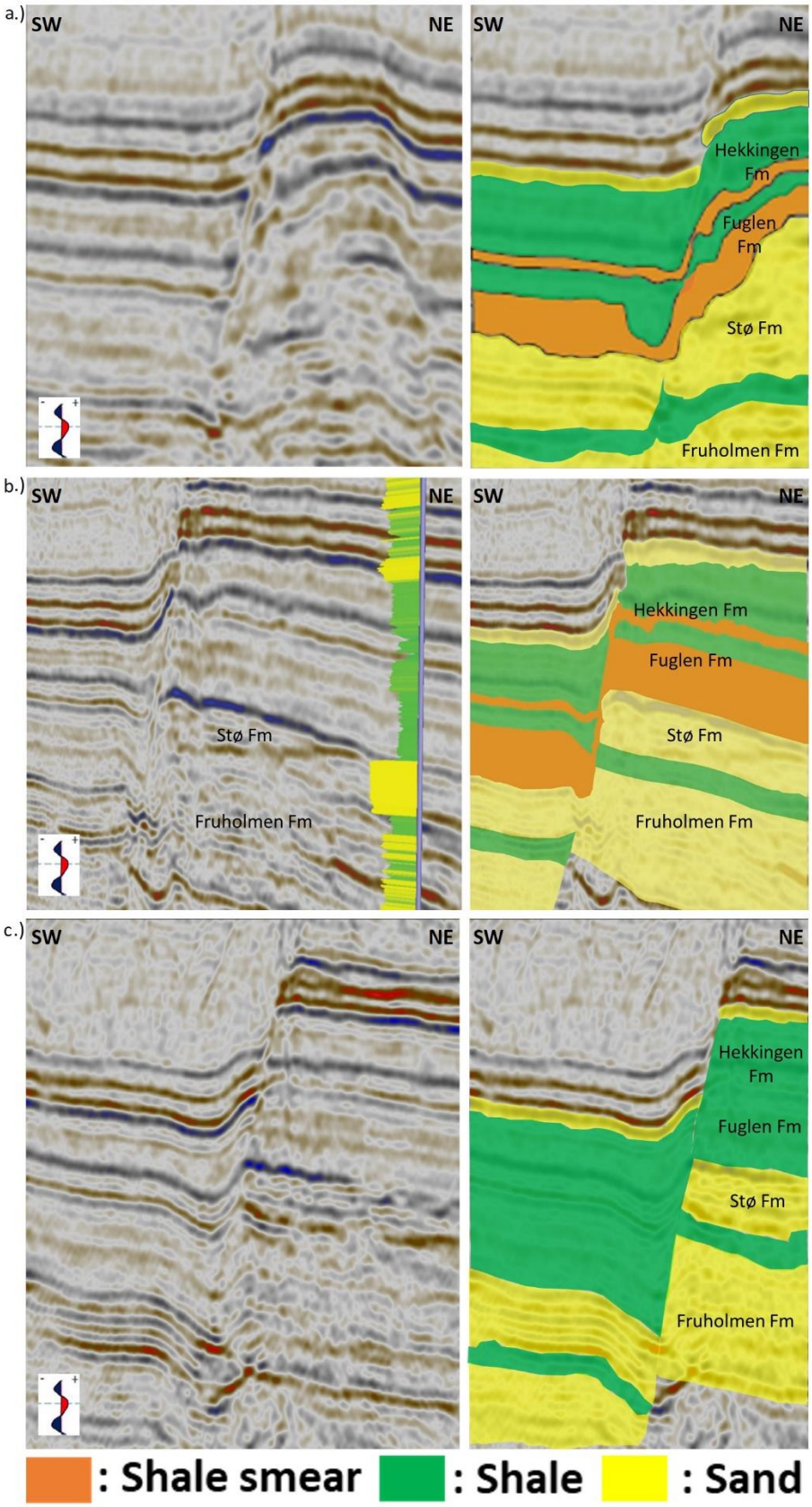

Figure 6.15: High-resolution seismic section showing shale smears on (a) the eastern part of the fault, (b) the central part of the fault, and (c) the western part of the fault. See lines A, B, C in Figure 6.14a as navigation lines. Shale smears from the two source beds do not mix in the eastern part, while in the central part they mix. Shale smear is not present in section c where the fault throw reaches its maximum value.

6.4.4. Shale gouge ratio and the fluid contact

The shale gouge ratio (SGR) is determined by the percentage of the shale fraction that enters the fault zone. In this chapter, the shale gouge ratio will be used to define the sealing nature of the fault. The shale smear description of **section 6.4.3** is used to support the discussion.

Figure 6.16 shows a seismic line from the low-resolution seismic (**a**), and high-resolution seismic (**b**). The well 7324/8-3 with gamma ray log, as well as the fault plane with the SGR distribution are included. In **Figure 6.16a**, the sandstone of the Stø Fm is only characterized by a trough and a peak, while in **Figure 6.16b** the Stø Fm is displayed in much more detail (two troughs and three peaks). In the low- and high-resolution models, the SGR values do not change significantly laterally, but they vary vertically. The highest SGR value is 60% which is located at the shale-shale juxtaposition and along the shale smear zone (**Figure 6.15b**). The lowest SGR value (5-15%) is at the juxtaposition of the Fruholmen Fm (sandstone) in the footwall against the Stø Fm in the hanging-wall (**Figure 6.15b**). At the Stø reservoir level in the footwall, the SGR value is 25-50%, indicating fault sealing. This value is consistent with the juxtaposition of the Stø Fm with the shale smear and the shale zone (**Figure 6.15b**).

Figure 6.17 shows the impact of a high shale gouge ratio (SGR). The flat spot (fluid contact) can only be observed in the high-resolution seismic. The report of well 7324/8-3 (Norwegian Petroleum Directorate) states that the Stø reservoir is filled with oil and the lowest known oil is down to 722.2 m at the Fruholmen Fm. In **Figure 6.17b**, the flat spot terminates against the fault, updip of the 7324/8-3 well. Thus the flat spot should correspond to the gas-oil contact. Shale smears and shale-shale juxtaposition (**Figure 6.15b**), and high SGR value (25-50%) (**Figure 6.17b**) allow the Stø Fm to retain hydrocarbons (gas and oil) in the tilted fault block.

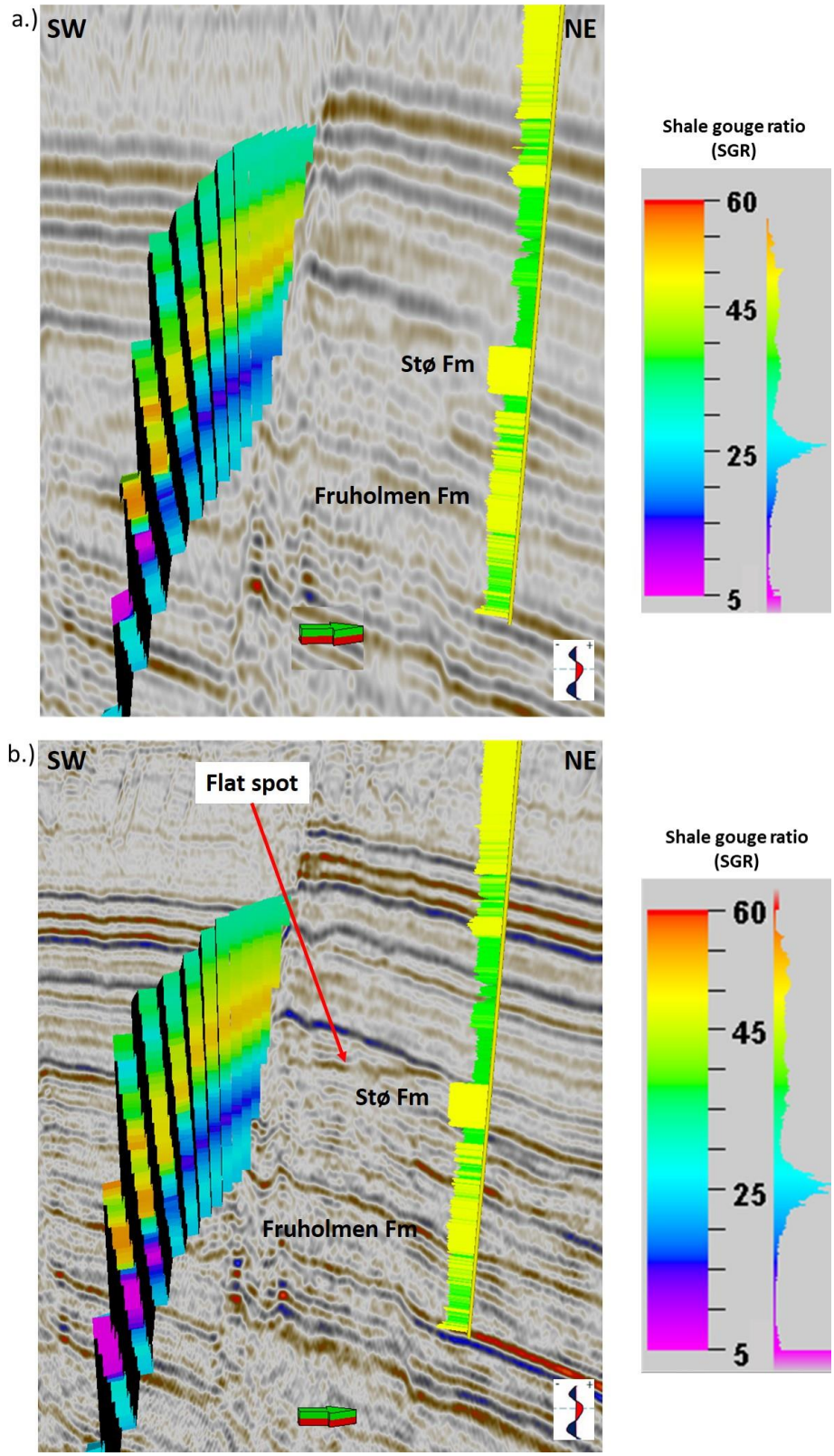

Figure 6.16: (a) Low-resolution seismic line and well 7324/8-3 with gamma-ray log (b) Same section showing high-resolution seismic and well 7324/8-3 with gamma-ray log. In both sections, the shale gouge ratio (SGR) on the fault is displayed. Yellow in the gamma ray log is sandstone while green is shale. The highest SGR value (60%) is at the juxtaposition of shale against shale, and the lowest SGR value (5-15%) is at the sand-sand juxtaposition (Figure 6.15b). At the Stø reservoir level, the SGR value is around 25-50% indicating probable fault sealing. Line B in Figure 6.14a shows the section navigation.

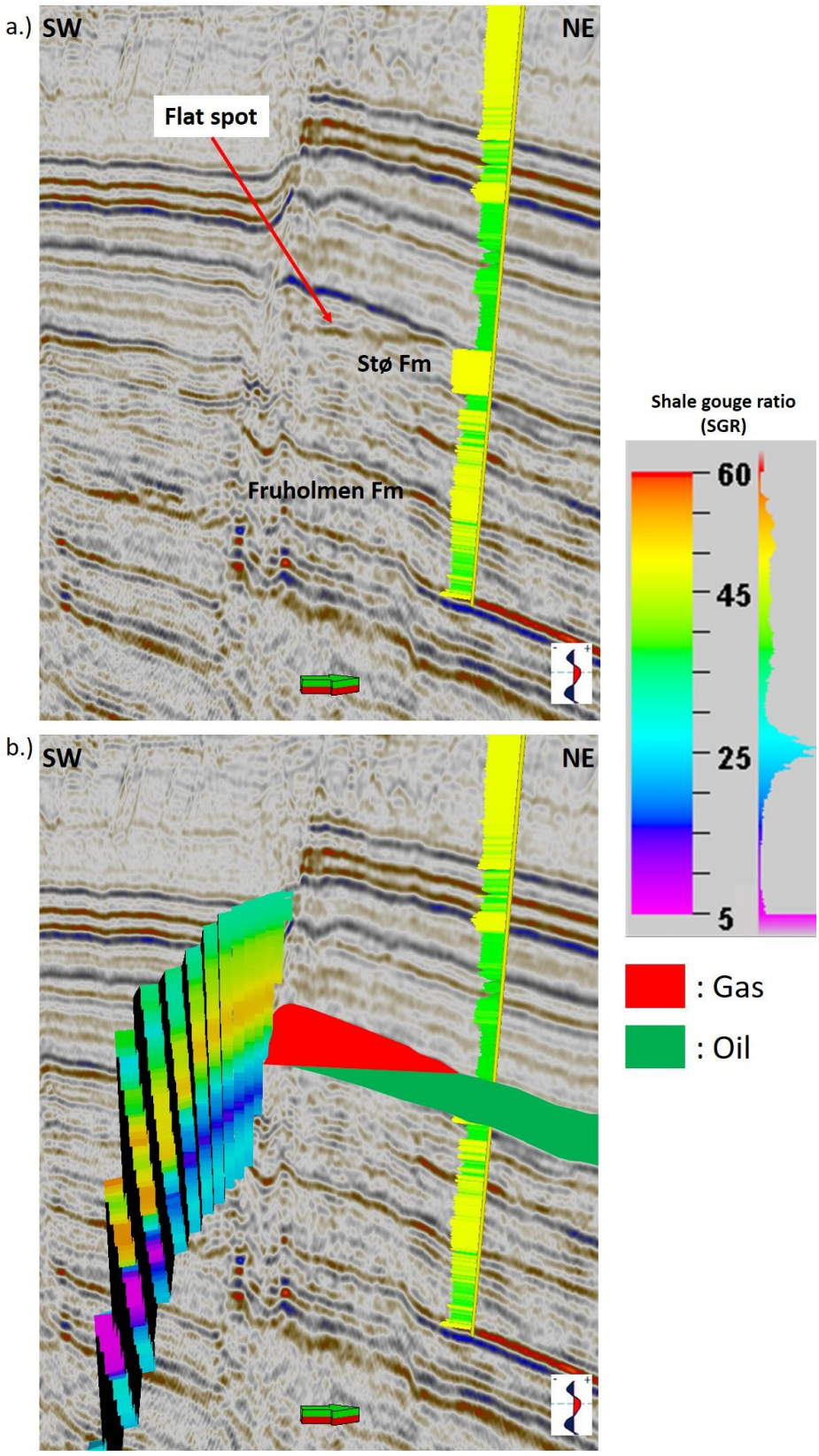

Figure 6.17: (a) High-resolution seismic line and well 7324/8-3 with gamma-ray log. (b) Same line and log with fault with SGR values and the fluid contact. The Stø Fm at the well is filled with oil. The lowest known oil is down to 722.2m in the Fruholmen Fm (NPD). The flat spot terminates at the fault and updip of the well. Hence, the flat spot should correspond to the gas-oil contact. Line B in Figure 6.14a shows the section navigation.

6.5. Gross volume

In this section, the bulk and the gross hydrocarbon volumes in the Stø Fm will be compared between the low- and high-resolution models. The gas oil-contact was set to -634m TVD (depth of the flat spot in the high-resolution seismic), and the oil-water contact was set to –692.2m TVD or -722.2m MD (Norwegian Petroleum Directorate). Due to the lack of porosity, net to gross, water, oil, and gas saturation values, the volumetric will be based on the gross volume.

Table 6.1 shows the difference in total bulk volume between the low- and high-resolution models. The low-resolution model has a bigger bulk volumes (155 x$10^6 m^3$) than the high-resolution model (136 x$10^6 m^3$). As a result, the low-resolution model contains more gross volume in both oil (**Table 6.2**) and gas (**Table 6.3**) than the high-resolution model. The low-resolution model contains a gross oil volume of (134,610x$10^3 sm^3$) and a gross gas volume of (20,216x$10^3 sm^3$), whereas the high-resolution model has a gross oil volume of (117,393 x$10^3 sm^3$) and a gross gas volume of (17,629 x$10^3 sm^3$).

Figure 6.18 illustrates the volume uncertainty using two cross sections. Cross section b along the well (**Figure 6.18b)** shows the low-resolution top Stø and top Fruholmen (white lines), the same surfaces in the high-resolution model (black lines), and the gas and oil zones. The Stø Fm from the low-resolution model is thicker in the south-western block than in the north-eastern block. In addition, the top Stø and top Fruholmen surfaces undulate, especially farther away from the well. In contrast, the Stø Fm from the high-resolution model shows a near-constant thickness, and the top and the bottom of the reservoir are more consistent. In this cross-section, the north-eastern block consists of gas and oil while the south-western block is only filled with oil, in both the low- and high-resolution models.

Cross section c at the west of the well (**Figure 6.18c)** shows a small gas zone in the south-western block for the low-resolution model. In the high-resolution model, this gas zone does not exist. As seen in **Figure 6.18b-c**, the low resolution model has a thicker reservoir zone than the high-resolution model, especially in the south-western block. The thicker reservoir zone and the gas zone in the south-western block result from the horizons uncertainty in the low-resolution model. The top Stø and top Fruholmen were adjusted to the well-tops in the geomodelling process (**Figure 6.18b**). However, the uncertainty of these horizons increases away from the well.

Table 6.1: Overview of the total bulk volumes in both resolution models.

Model Resolution	Bulk Volume ($\times 10^6 m^3$)			Total Bulk Volumes ($\times 10^6 m^3$)
	Top Stø - Inner reservoir 1	Inner reservoir 1 - Inner Reservoir 2	Inner Reservoir 2 - Top Fruholmen	
Low-resolution	155			155
High-resolution	41	26	69	136

Table 6.2: Overview of the total gross oil volumes in both resolution models.

Model Resolution	Gross Oil ($\times 10^3 sm^3$)			Total Gross Oil ($\times 10^3 sm^3$)
	Top Stø - Inner reservoir 1	Inner reservoir 1 - Inner Reservoir 2	Inner Reservoir 2 - Top Fruholmen	
Low-resolution	134610			134610
High-resolution	33222	22400	61771	117393

Table 6.3: Overview of the total gross gas volumes in both resolution models.

Model Resolution	Gross Gas ($\times 10^3 sm^3$)			Total Gross Gas ($\times 10^3 sm^3$)
	Top Stø - Inner reservoir 1	Inner reservoir 1 - Inner Reservoir 2	Inner Reservoir 2 - Top Fruholmen	
Low-resolution	20216			20216
High-resolution	7365	3125	7139	17629

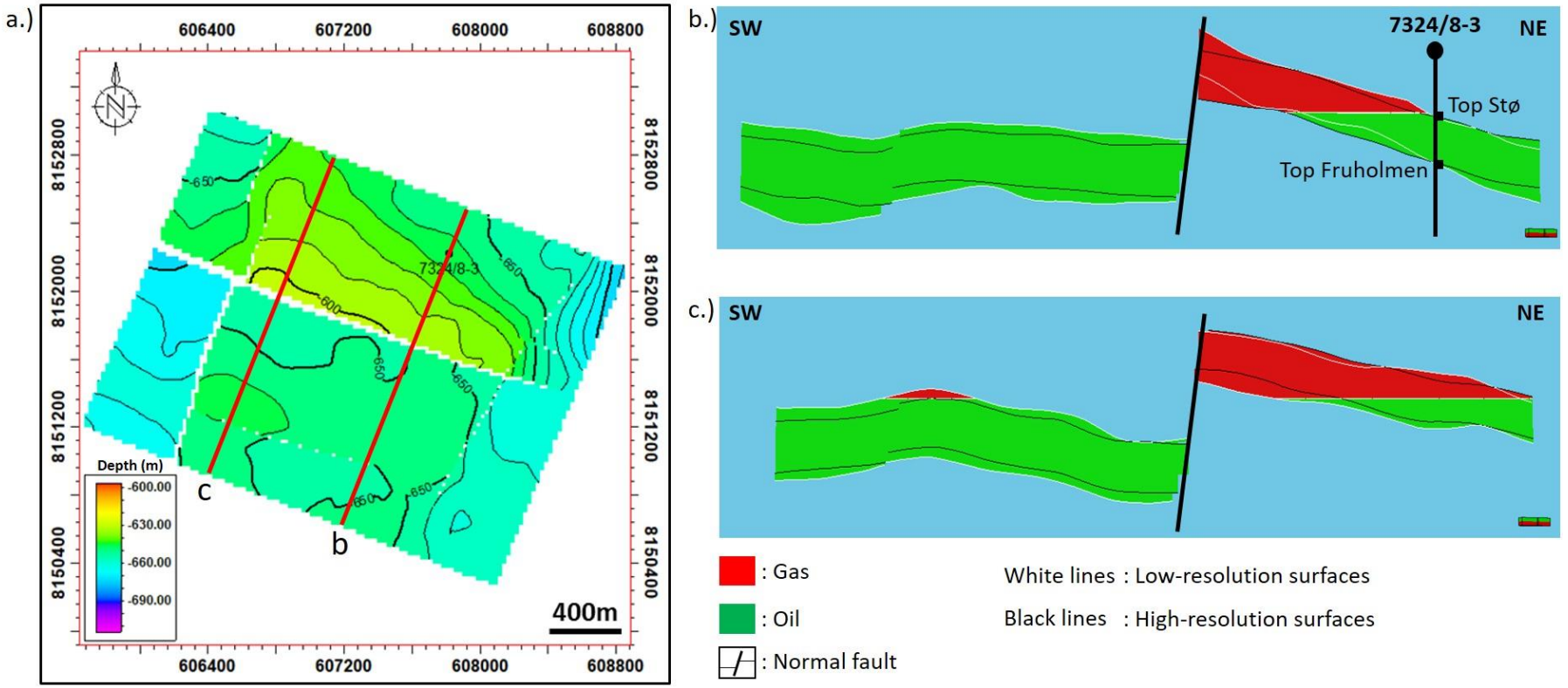

Figure 6.18: (a) Structure map of the top Stø, well 7324/8-3 and cross sections b and c. (b) Cross section b showing the hydrocarbon accumulation at the well. In both model resolutions, the gas and oil contact is observed in the north-eastern block. The depth of the gas-oil contact was set based on the flat spot depth from the high-resolution seismic. (c) Cross-section c showing the hydrocarbon accumulation west of the well. Gas is present in the south-western block of the low-resolution model, but not in the high-resolution model.

7. Discussion

Seismic attributes play an important role in guiding the structural interpretation and in defining the hydrocarbon accumulation. The variance attribute provides a sharper fault image in the high-resolution seismic than in the low-resolution seismic. The low-resolution seismic does not capture the NNE-SSW fault near the eastern boundary. This fault cannot be observed in the seismic section and is displayed as low variance values in the time slice (**Figures 6.3a-b and 6.2a**). In terms of defining the hydrocarbon accumulation, the RMS attribute at the top Stø level is similar in the low- and high-resolution seismic. The high amplitude values (blue) concentrate in the vicinity of the WNW-ESE fault. However, the extent of this area is larger in the high-resolution seismic (**Figure 6.4**).

In comparison to the low-resolution seismic, the high-resolution seismic is superior in defining the reservoir heterogeneity, flat spot, horizon uncertainties, and reservoir isochore. The Stø Fm is captured in much more detail in the high-resolution seismic as it provides more reflectors (5 reflectors) that describe the inner reservoir structure, whereas in the low-resolution seismic, the Stø Fm is only characterized by two reflectors (a trough and a peak) (**Figure 5.3**). The flat spot that corresponds to the gas-oil contact is observed in the high-resolution seismic, but not in the low-resolution seismic (**Figure 6.5**). This information is critical for determining the hydrocarbon volumetric. Seismic resolution has an impact on imaging the subsurfaces. In the low-resolution seismic, the top Stø and top Fruholmen do not honour the well-tops and have increasing uncertainties with depth (**Figure 6.6**). In contrast, the high-resolution seismic allows a more accurate mapping of these surfaces (**Figure 6.6**). As a result, the high-resolution Stø Fm isochore shows less thickness variation (**Figure 6.8a**) than the low-resolution Stø isochore (**Figure 6.8b**).

The fault network, fault cutoffs, and fault throw distribution are constructed based on the interpreted horizons and faults in the datasets. Due to the ability of the high-resolution seismic to capture the NNE-SSW fault (pink-red) (**Figure 6.9b**), and the lower uncertainty of the interpreted horizons from the high-resolution data, the fault network and fault cutoffs are more accurate and consistent in the high-resolution model, and therefore they represent more reliable the reservoir compartmentalization (**Figure 6.9b, 6.10b**). The fault throw distribution in the high-resolution model (**Figure 6.11b, d**) is also more realistic than in the low-resolution model (**Figure 6.11a, c**).

The higher quality of the high-resolution interpretations is also observed in the Allan diagram, since the juxtaposition between the Stø Fm and the other formations across the fault is controlled by the fault throw. In the low- and high-resolution models, the Stø Fm is juxtaposed against itself in the east where the throw is small (0-10m) (**Figure 6.12**). However, to the west, as the fault throw increases, the Stø Fm is juxtaposed against the Fuglen Fm until the throw reaches its maximum value (60-70m). To the west of this throw maximum, the Stø Fm is juxtaposed against the Kolje-Klippfisk-Hekkingen zones (**Figure 6.12**). In addition, in the high-resolution model, the Stø Fm-Fruholmen Fm juxtaposition shows three zones due to the better definition of the inner structure of the Stø Fm (**Figure 6.12b**). These juxtapositions are better visualized in the high-resolution model due to the inability of the low-resolution model to capture the inner structure of the Stø Fm (**Figure 6.12a**) and its unrealistic fault throw (**Figure 6.11a, c**).

The high-resolution seismic provides the unique opportunity of interpreting the shale smear along the WNW-ESE fault (**Figure 6.14)**. The lateral continuity of the shale smear can be related to the fault throw. Two separate shale smears are observed in a section across the eastern part of the fault (**Figure 6.15a**). These two shale smears are connected in a section across the central part of the fault (**Figure 6.15b**), and as the fault throw reaches its maximum, the shale smear cannot longer be observed on a section across the western part of the fault (**Figure 6.15c**). The shale smear vertical continuity also changes along the fault and is affected by the mixing behaviour of shales from the two different source formations, Hekkingen and Fuglen. The low- and high-resolution model display a similar shale gouge ratio (SGR) along the fault, with values of 25-50% at the Stø reservoir level, indicating probable fault sealing (**Figure 6.16**). However, with the flat spot (**Figure 6.17a**), and the evidence of oil accumulation at well 7324/8-3, the high-resolution seismic provides vital information for determining a gas accumulation updip of the well (**Figure 6.17b**).

The uncertainty of the interpretation, structural model, and fluid contacts impact the estimated bulk, and gross hydrocarbon volumes. The low-resolution model does not allow to identify the gas-oil contact which is evident in the high-resolution seismic. The reservoir zone in the low-resolution model is thicker, especially in the SW fault block (hanging wall) far from the well (**Figure 6.18b-c**). So even if the gas-oil contact is determined by other means, the low-resolution model would suggest a gas accumulation in the SW fault block that is not present in the high-resolution model (**Figure 6.18b-c**).The larger bulk and gross hydrocarbon volumes in

the low-resolution model (**Tables 6.1**, **6.2**, **6.3**) result from the larger uncertainty of the interpreted horizons in this model (**Figure 6.18b-c**).

8. Conclusion

Based on the results of this Master thesis, the following conclusion can be reached:

- Fault and horizons are sharper and better identifiable in the high-resolution seismic. The top and bottom of reservoir zones from the high-resolution seismic honour the well-tops and seismic reflectors, whereas this is not the case in the low-resolution seismic. In addition, the high-resolution seismic is suitable for interpreting the reservoir inner structures. As a result, the interpreted surfaces and fault network provide a more reliable assessment of reservoir compartmentalization.
- The low-resolution structural model is subject to uncertainty as the faults, reservoir interval, and flat spot features are not well defined. In contrast, the ability to capture subtle faults and flat spots, as well as addressing the reservoir inner structures in the high-resolution seismic results in a more reliable fault network and reservoir surfaces. Thus, the high-resolution structural model represents better the reservoir compartmentalization and consequently reducing uncertainty in estimating the bulk and hydrocarbon volumes.
- The high-resolution seismic is superior to the low-resolution seismic in terms of determining fault-juxtaposition relationships. The high-resolution seismic allows to reliably track more horizons which results in a more detailed Allan diagram. Moreover, the continuity of the shale smear is clearly visualized by the high-resolution seismic and can be incorporated with the high-resolution fault throw distribution. The SGR alone does not provide this information. SGR is rather a gross estimation of fault sealing, as demonstrated by the fact that the SGR of low- and high-resolution models is quite similar.

9. Recommendation for future work

Based on the results of this Master thesis, the following recommendations are made:

- In order to get a more accurate volume of shale (Vsh) for determining the shale gouge ratio, the Vsh calculation should also be cross-checked using other logs, logs combinations (e.g., neutron-density), and core data.
- A detailed facies log is needed to deliver a more reliable facies distribution that can be incorporated to the Allan diagram. In addition, the availability of the porosity log can provide a better understanding of the reservoir heterogeneity, and hence the reservoir connectivity between the different compartments.
- Seismic inversion could help a lot in capturing the reservoir heterogeneity through guiding the porosity and the facies modelling via collocated co-simulation
- A more accurate model from the high-resolution data will undoubtedly improve any geomechanical estimation of the risk of fluids leaking to the surface. We therefore recommend following an interpretation and modelling workflow similar to this thesis in order to construct accurate and consistent structural models of the field.

10. References

Allan, U. S. (1989). Model for hydrocarbon migration and entrapment within faulted structures. *American Association of Petroleum Geologists Bulletin*, *73*(7), 803–811. https://doi.org/10.1306/44b4a271-170a-11d7-8645000102c1865d

Almasgari, A. A., Elsaadany, M., Latiff, A. H. A., Hermana, M., Rahman, A. H. B. A., Babikir, I., Imran, Q. S., Appiah, N. F., & Adeleke, T. O. (2020). Application of seismic attributes to delineate the geological features of the malay basin. *Bulletin of the Geological Society of Malaysia*, *69*(May), 97–110. https://doi.org/10.7186/bgsm69202009

Avseth, P., Mukerji, T., & Mavko, G. (2005). Common techniques for quantitative seismic interpretation. In *Quantitative Seismic Interpretation: Applying Rock Physics Tools to Reduce Interpretation Risk* (pp. 168-257). Cambridge: Cambridge University Press. doi:10.1017/CBO9780511600074.005

Bacon, M., Simm, R., & Redshaw, T. (2003). *3-D Seismic Interpretation*. Cambridge: Cambridge University Press. doi:10.1017/CBO9780511802416

Brown, A.R. (1999). Interpretation of three-dimensional seismic data: Oklahoma, AAPG Memoir 42, 528p.

Boschi, M., (2017). Wisting-Developing shallow reservoirs in the Barents Sea (abs).

Clarke, S. M., Burley, S. D., & Williams, G. D. (2005). A three-dimensional approach to fault seal analysis: Fault-block juxtaposition & argillaceous smear modelling. *Basin Research*, *17*(2), 269–288. https://doi.org/10.1111/j.1365-2117.2005.00263.x

Collanega, L., M. Massironi, A. Breda, and B. E. Kjølhamar, 2017, Onset of N-Atlantic rifting in the Hoop Fault Complex (SW Barents Sea): An orthorhombic dominated faulting?: Tectonophysics, v. 706-707, p. 59-70, doi: 10.1016/j.tecto.2017.04.003.

Czajkowski, M.K., (2015). Sensitivity of seismic well ties to attenuation effects. Master thesis, Norwegian University of Science and Technology, 71p.

Dengo, C. A., & Røssland, K. G. (1992). Extensional tectonic history of the western Barents Sea. *Norwegian Petroleum Society Special Publications*, *1*(C), 91–107. https://doi.org/10.1016/B978-0-444-88607-1.50011-5

Doyen, P. (2007). Seismic Reservoir Characterization: An Earth Modelling Perspective (EET 2). In *Seismic Reservoir Characterization: An Earth Modelling Perspective (EET 2)*. https://doi.org/10.3997/9789073781771

Fagin, S. (1996). The fault shadow problem: Its nature and elimination. *Leading Edge (Tulsa, OK)*, *15*(9), 1005. https://doi.org/10.1190/1.1437403

Færseth, R. B., Johnsen, E., & Sperrevik, S. (2007). Methodology for risking fault seal capacity: Implications of fault zone architecture. *American Association of Petroleum Geologists Bulletin*, *91*(9), 1231–1246. https://doi.org/10.1306/03080706051

Faleide, J. I., Gudlaugsson, S. T., & Jacquart, G. (1984). Evolution of the western Barents Sea. *Marine and Petroleum Geology*, *1*(2), 70–78. https://doi.org/10.1016/0264-8172(84)90082-5

Faleide, J. I., K. Bjørlykke, and R. H. Gabrielsen, 2010, Geology of the Norwegian Continental Shelf, Petroleum Geoscience, p. 467-499.

Faleide, T. S., I. Midtkandal, S. Planke, R. Corseri, J. I. Faleide, C. S. Serck, and J. P. Nystuen, 2019, Characterisation and development of Early Cretaceous shelf platform deposition and faulting in the Hoop area, southwestern Barents Sea—constrained by high-resolution seismic data: Norwegian Journal of Geology, doi: 10.17850/njg99-3-7.

Fisher, Q. J., & Knipe, R. J. (1998). Fault sealing processes in siliciclastic sediments. *Geological Society, London, Special Publications*, *147*(1), 117 LP – 134. https://doi.org/10.1144/GSL.SP.1998.147.01.08

Fitriyanto, A., (2011). Structural Analysis of the Hoop Fault Complex, SW Barents Sea. Master thesis, University of Oslo, 81p.

Gabrielsen, R.H., Færseth, R.B., Jensen, L.N., Kalheim, J.E., Riis, F., 1990. Structural Elements of the Norwegian Continental Shelf. Part I: The Barents Sea Region. Norwegian Petroleum Directorate Bulletin, 6.

Gardner, G. H. F., Gardner, L. W., & Gregory, A. R. (1974). Formation Velocity and Density - the Diagnostic Basics for Stratigraphic Traps. *Geophysics*, *39*(6), 770–780. https://doi.org/10.1190/1.1440465

Glørstad-Clark, E., J. I. Faleide, B. A. Lundschien, and J. P. Nystuen, 2010, Triassic seismic sequence stratigraphy and paleogeography of the western Barents Sea area: Marine and Petroleum Geology, v. 27, no. 7, p. 1448-1475, doi: 10.1016/j.marpetgeo.2010.02.008.

Gudlaugsson, S. T., Faleide, J. I., Johansen, S. E., & Breivik, A. J. (1998). Late Palaeozoic structural developments of the south-western Barents Sea. *Marine and Petroleum Geology*, *15*(1), 73–102. https://doi.org/10.1016/S0264-8172(97)00048-2

Harding, T. P., & Tuminas, A. C. (1989). Structural interpretation of hydrocarbon traps sealed by basement normal block faults at stable flank of foredeep basins and at rift basins. *American Association of Petroleum Geologists Bulletin*, *73*(7), 812–840. https://doi.org/10.1306/44b4a276-170a-11d7-8645000102c1865d

Hardwick, A., & Rajesh, L. (2013). A 3D illumination study to investigate fault shadow effects over the Hoop Fault Complex. *Society of Exploration Geophysicists International Exposition and 83rd Annual Meeting, SEG 2013: Expanding Geophysical Frontiers*, 3315–3319. https://doi.org/10.1190/segam2013-0849.1

Henriksen, E., H. M. Bjørnseth, T. K. Hals, T. Heide, T. Kiryukhina, O. S. Kløvjan, G. B. Larssen, A. E. Ryseth, K. Rønning, K. Sollid, and A. Stoupakova, 2011a, Chapter 17 Uplift and erosion of the greater Barents Sea: impact on prospectivity and petroleum systems: Geological Society, London, Memoirs, v. 35, no. 1, p. 271-281, doi: 10.1144/m35.17.

Henriksen, E., A. E. Ryseth, G. B. Larssen, T. Heide, K. Rønning, K. Sollid, and A. V. Stoupakova, 2011b, Chapter 10 Tectonostratigraphy of the greater Barents Sea: implications for petroleum systems: Geological Society, London, Memoirs, v. 35, no. 1, p. 163-195, doi: 10.1144/m35.10.

Ismail, A., Ewida, H. F., Al-Ibiary, M. G., Gammaldi, S., & Zollo, A. (2020). Identification of gas zones and chimneys using seismic attributes analysis at the Scarab field, offshore, Nile Delta, Egypt. *Petroleum Research*, *5*(1), 59–69. https://doi.org/10.1016/j.ptlrs.2019.09.002

Jakobsson, M., Gyllencreutz, R., Mayer, L. A., Dowdeswell, J. A., Canals, M., Todd, B. J., Dowdeswell, E. K., Hogan, K. A., & Larter, R. D. (2016). Mapping submarine glacial landforms using acoustic methods. *Geological Society Memoir*, *46*(1), 17–40. https://doi.org/10.1144/M46.182

Kennedy, M. (2015). Introduction to Log Analysis: Shale Volume and Parameter Picking. *Developments in Petroleum Science*, *62*, 151–180. https://doi.org/10.1016/B978-0-444-63270-8.00006-2

Kettermann, M., Smeraglia, L., Morley, C. K., Von Hagke, C., & Tanner, D. C. (2019). Fault sealing. In *Understanding Faults: Detecting, Dating, and Modeling*. Elsevier Inc. https://doi.org/10.1016/B978-0-12-815985-9.00008-4

Klausen, T. G., R. Müller, M. Poyatos-Moré, S. Olaussen, and E. Stueland, 2019, Tectonic, provenance and sedimentological controls on reservoir characteristics in the Upper Triassic–Middle Jurassic Realgrunnen Subgroup, SW Barents Sea: Geological Society, London, Special Publications, doi: 10.1144/sp495-2018-165.

Knipe, R. J. (1992). Faulting processes and fault seal. In *Norwegian Petroleum Society Special Publications* (Vol. 1, Issue C). Elsevier B.V. https://doi.org/10.1016/B978-0-444-88607-1.50027-9

Knott, S. D. (1993). Fault seal analysis in the North Sea. In *American Association of Petroleum Geologists Bulletin* (Vol. 77, Issue 5, pp. 778–792). https://doi.org/10.1306/bdff8d58-1718-11d7-8645000102c1865d

Lasabuda, A. P. E., N. S. Johansen, J. S. Laberg, J. I. Faleide, K. Senger, T. A. Rydningen, H. Patton, S.-M. Knutsen, and A. Hanssen, 2021, Cenozoic uplift and erosion of the Norwegian Barents Shelf – A review: Earth-Science Reviews, v. 217, doi: 10.1016/j.earscirev.2021.103609.

Li, M., & Zhao, Y. (2014). Seismic Attribute Analysis. *Geophysical Exploration Technology*, 103–131. https://doi.org/10.1016/b978-0-12-410436-5.00005-8

Lindsay, N. G., Murphy, F. C., Walsh, J. J., & Watterson, J. (1993). Outcrop studies of shale smears on fault surfaces. *International Association of Sedimentologist Special Publication 15*, p.113-123

Meunier, K.H., (2019). Reservoir Characterization of the Realgrunnen Subgroup in Wisting Central III (7425/8-3), SW Barents Sea: Controls on Reservoir Quality in the Triassic-Jurassic Transition. Master thesis. University of Oslo, 203p.

Mondol, N. H., 2010, Seismic Exploration, Petroleum Geoscience, p. 375-402.

Norwegian Petroleum Directorate, 2021. Wellbore: 7324/8-3 - Factpages - NPD (accesed 4.1.21).

Paulsen, R., Grundvåg, S., Senger, K., & Stueland, E. (2019). Seal integrity in the uplifted basins in the greater hoop area on the northern barents shelf. *5th International Conference on Fault and Top Seals 2019, September 2019*. https://doi.org/10.3997/2214-4609.201902355

Pindel, A., (2020). Comparison of facies models based on stochastic versus deterministic AVO inversion. Master thesis. The University of Stavanger, 87p.

Planke, S., Eriksen, F.N., Berndt, C., Mienert, J. and Masson, D.G., 2009. P-Cable high-resolution seismic. Oceanography, 22, 85-85

Ringrose, P. and Bentley, M., 2015, Reservoir Model Design, How to build good reservoir models, Springer

Rotar, V., (2019). Reservoir Modeling and Uncertainty Estimation: A Comparison Between Stochastic and Deterministic Inversion. Master thesis. The University of Stavanger, 104p.

Schlumberger, 2017. Training manual property modelling.

Schlumberger, 2019. Petrel user assistance.

Simm, R., & Bacon, M. (2014). Seismic wavelets and resolution. In *Seismic Amplitude: An Interpreter's Handbook* (pp. 23-37). Cambridge: Cambridge University Press. doi:10.1017/CBO9780511984501.004

Smelror, M., Mørk, A., Monteil, E., Rutledge, D., & Leereveld, H. (1998). The Klippfisk formation - a new lithostratigraphic unit of Lower Cretaceous platform carbonates on the Western Barents Shelf. *Polar Research*, *17*(2), 181–202. https://doi.org/10.1111/j.1751-8369.1998.tb00271.x

Smith, P., & Mattox, B. (2020). A time-lapse seismic repeatability test using the P-Cable high-resolution 3D marine acquisition system. *Leading Edge*, *39*(7), 480–487. https://doi.org/10.1190/tle39070480.1

Stueland, E., (2016). Wisting-shallow reservoir possibilities and challenges. FORCE Underexplored Plays II.

Tomasgaard, M., (2018). Time dependent signal of a chalk field: The South Arne Field, Danish North Sea. Master thesis. The University of Stavanger, 105p.

Watts, N. L. (1987). Theoretical aspects of cap-rock and fault seals for single- and two-phase hydrocarbon columns. *Marine and Petroleum Geology*, *4*(4), 274–307. https://doi.org/https://doi.org/10.1016/0264-8172(87)90008-0

Weber, K. J., Mandl, G., Pilaar, W. F., Lehner, F., & Precious, R. G. (1978). The role of faults in hydrocarbon migration and trapping in Nigerian growth fault structures. *Proceedings of the Annual Offshore Technology Conference*, *1978-May*, 2643–2647. https://doi.org/10.4043/3356-ms

White, R., & Simm, R. (2003). Tutorial: Good practice in well ties. *First Break*, *21*(10), 75–83. https://doi.org/10.3997/1365-2397.21.10.25640

Yadav, L., Ghosh, D., Maurya, S., & Bhattacharya, A. (2004). Calibration of Sonic Logs for Seismic Applications in Upper Assam. *Spgindia.Org*, *April*, 154–161. http://www.spgindia.org/conference/5thconf_hyd04/123484.PDF

Yielding, G., Freeman, B., & Needham, D. T. (1997). Quantitative fault seal prediction. *AAPG Bulletin*, *81*(6), 897–917. https://doi.org/10.1306/522b498d-1727-11d7-8645000102c1865d

Yielding, G. (2002). Shale Gouge Ratio - calibration by geohistory. *Norwegian Petroleum Society Special Publications*, *11*(C), 1–15. https://doi.org/10.1016/S0928-8937(02)80003-0